Theory of Terahertz Pumping of Chemical Environments in the Condensed Phase

Ultrafast Energy Transfer by Highly Intense and Ultrashort THz Pulse

Dissertation
zur Erlangung des Doktorgrades an der Fakultät für
Mathematik, Informatik und Naturwissenschaften
Fachbereich Physik
der Universität Hamburg

vorgelegt von
Pankaj Kumar Mishra
aus
India

Hamburg
2015

Gutachter der Dissertation: Dr. Oriol Vendrell
Prof. Dr. Michael Thorwart

Gutachter der Disputation: Prof. Dr. Nils Huse
Prof. Dr. Gabriel Bester
Prof. Dr. Michael A. Rübhausen

Datum der Disputation: 01.12.2015

Vorsitzender des Fach-Promotionsausscuhsses: Prof. Dr. Michael A. Rübhausen

Leiter des Fachbereiches Physik: Prof. Dr. Peter Hauschildt

Dekan der Fakultät für Mathematik,
Informatik und Naturwissenschaften: Prof. Dr. Heinrich Graener

dedicated to

My Parents

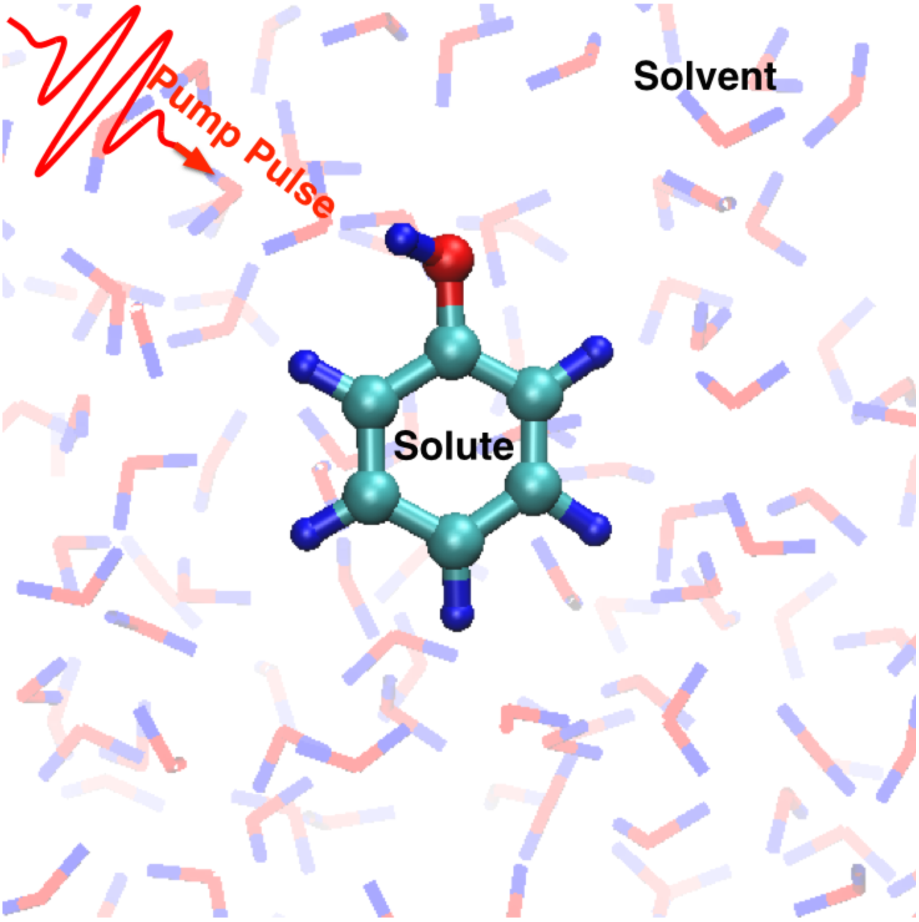

Figure: Schematic figure of laser pulse pumping on phenol, as an example solute in liquid water solvent.

Zusammenfassung

Neue Laser ermöglichen es synchronisierte, ultra-kurze und ultra intensive Lichtblitze zu erzeugen. Diese erlauben es Prozesse mittels eines Pump Laserpulses zu starten und die Dynamik mittels eines Probe Pulses in Femtosekunden Auflösung zu verfolgen. Diese Pump-Probe Experimente sind von signifikanter Bedeutung für die Untersuchung chemischer und biologische Prozesse in Femtosekunden Zeitskala. Die Methodik wird auch zur Untersuchung von Femtosekunden-Temperatursprung-Erzeugung (T-jump), um sehr schnelle Kinetik fundamentaler chemischer Prozesse zu untersuchen. Aufgrund seiner biologischen und chemischen Relevanz, haben T-jump Experimente mit flüssigem Wasser viel Beachtung erhalten. In chemischen und biologischen Prozessen, ist die Wasserdynamik fundamental wichtig während der Solvatisierung und der Stabilisierung von Reaktions-Zwischenprodukten. Oftmals wird die O-H Streckschwingung mit einem Infrarot (IR) Laser angeregt, um eine T-jump in Nano- bis Femtosekunden Zeitskala zu erzeugen. Mit diesem Mechanismus wurden bislang Temperatursprünge von wenigen Zehn-Kelvin erzeugt. In dieser Arbeit wird ein neuer Mechanismus untersucht, um T-jumps von wenigen hundert Kelvin in sub-Pikosekunden Zeitskala zu erzeugen.

Der Hauptteil dieser Arbeit konzentriert sich mit der Antwort flüssigen Wassers auf Unterzyklus THz Pump-Pulse mit einer Wellenzahl von 100 cm^{-1}(3THz). Der THz Pump Puls mit einer Intensität von 5×10^{12} $\mathrm{W/cm}^2$ transportiert einen grosse Menge an Energie in die inner- und intramolekularen Schwingungen des Wasser in einer Sub-Pikosekunden Zeitskala. Nach dem Pump Puls, nähert sich das Wasser einem Quasi-Gleichgewichtszustand an, einem Gas-ähnlichem, sehr heissen Flüssigkeits-Zustand. Der sehr große Energie-Anstieg im Wasser erzeugt erheblich Strukturänderungen und Verschiebungen im vibrations spectrum, die mit zeit-aufgelöster, kohärenter Röntgenstreuung und zeitaufgelöster Infrarot Spektroskopie untersucht werden können. In diesem Kapitel wird die Wechselwirkung mit dem THz Puls für verschiedene Wasser-Cluster bis hin zum Kontinuum untersucht mit dem Ergebnis, dass diese hauptsächlich über die wechselwirkung des el. Feldes mit dem Dipolmoment der Wassermoleküle verstanden werden kann. Außerdem zeigen wir, dass die Absorption eines THz Pulses, maßgeblich durch die Temperatur und die Dichte des Wassers beeinflusst ist.

Das zweite Kapitel dieser Arbeit beschäftigt sich mit den Auswirkungen der durch den THz Pulse erzeugten heißen, gas-ähnlich, flüssigen Umgebung auf die in dem Wasser gelöste Moleküle. Wir zeigen, dass ein gelöstes Phenol-Molekül, als Beispiel, kaum Schwingungsenergie durch den THz Puls direkt aufnimmt. Allerdings erhält es erhebliche Schwingungsenergie durch die zahlreichen Stöße mit den sich sehr schnell bewegenden Wassermolekülen. Der THz Pulse beeinflusst die Dynamik beider Teile, des gelösten Moleküls und des Lösungsmittels, in wenigen ps erheblich. Mit THz Pulsen lassen sich daher möglicherweise chemische Prozesse initiieren noch bevor die bereitgestellte Energie in die Ausdehnung oder Verdampfung der medium geht.

Der letzte Teil dieser Arbeit gibt einen Überblick über die aktuell verfügbaren THz

Quellen, die für die hier betrachteten Pump-Probe Experimente verwendet werden könnten. Die Auswirkungen des Pulses auf das Wasser wird hier für verschiedene Frequenzen, Flüsse und Puls Dauern untersucht. Es zeigt sich, dass die Spitzen-Amplitude des Pulses besonders relevant ist bezüglich der Verringerung von Wasserstoff-Brückenbindungen. Nachdem Wasserstoff-Brückenbindungen aufgehoben sind, ist der Energietransfer eine Funktion des Flusses. Pulse mit einen Frequenz von 20 THz werden diskutiert als ein geeigneter Weg Temperatur-sprunge von bis Zu 1000 K oder darüber hinaus Zu erreichen.

Abstract

Newly emerged light-sources allow to generate fully synchronized, ultrashort and highly intense light pulses. With these light pulses, it is possible to initiate a process by a pump pulse and follow the dynamics via probe pulse in the femtosecond timescale. These pump-probe experiments play an important role for studying the chemical and biological processes in real time. Such techniques are also used to generate temperature-jump (T-jump) in ultrashort timescale to study the very fast kinetics of fundamental steps in chemical processes. Because of its biological and chemical relevance, T-jump experiments on liquid water have gained a lot of attention. Rather than acting as a passive environment, the dynamics of water during chemical and biological processes play a fundamental role in the solvation and stabilization of reaction intermediates. To target the O-H stretching mode of water with an infrared (IR) laser is a widely used mechanism to generate the T-jump in nanosecond to femtosecond timescales. With these techniques, T-jump has been limited only to few 10s of K so far. In this thesis, a new mechanism is investigated to generate T-jump up to few 100s of K in sub-ps timescale.

The main portion of this thesis concentrates on the response of liquid water to sub-cycle THz pump pulses spectrally centered at 100 cm^{-1} ($\sim$3 THz). The THz pump pulse with intensity of 5×10^{12} $\mathrm{W/cm}^2$ transfers a large amount of energy to inter- and intramolecular vibrations of water in sub-ps timescale. After the pump pulse, water reaches to a quasi-equilibrium state, which is a gas-like hot liquid. The large energy gain in water causes significant structural modifications and vibrational shifting, which can be probed by time-resolved coherent x-ray scattering and time-resolved IR spectroscopy, respectively. Here, the interaction of THz pulse with water molecules is investigated from clusters to bulk water. We find it to be mainly described via the interaction of electric field with the permanent dipole of water molecules. Further, we show that temperature and density of the water affect the energy transfer by THz pulse significantly.

Another section of this thesis is focused on investigating the response of solutes to such hot and gas-like liquid water environment, created by the THz pump pulse. We show that an isolated phenol molecule, as example solute gains negligibly small energy directly from such pump pulse. However, the phenol in liquid water environment gains significantly large amount of energy due to the strong collisions of the highly mobile water molecules. The THz pump also modifies the solute-solvent dynamics substantially in sub-ps timescale. Thus, THz can potentially activate chemical processes long before the large amount of energy supplied to the system, leads to volume increase and vaporization of the medium.

The last part of this thesis presents the state of art of existing THz sources for the possible pump-probe experiments. The response of water is analyzed for pulses of different central frequencies, pulse fluence and pule duration. The peak field amplitude of pulse plays crucial role in H-bond depletion. Once H-bond are broken, the energy transfer to water depends on the fluence of the pulse. A pump pulse of 20 THz frequency is also discussed as an adequate pumping mechanism for T-jump up to 1000 K or beyond.

Contents

LIST OF PUBLICATIONS xv

1 Introduction 1

1.1 Introduction : Chemical Reactions . . . 1

1.2 Femtochemistry . . . 2

1.3 Uni-molecular Reaction Rate Theory: Transition State Theory . . . 4

1.4 Temperature-Jump Experiment . . . 8

1.4.1 Historical Background . . . 8

1.4.2 Ultrafast Temperature-Jump Experiments . . . 8

1.4.3 Pump-probe Studies of Ultrafast T-jump in Liquid Water . . . 9

1.5 X-ray Free Electron Lasers on Liquid Water . . . 10

1.6 Computational Studies on Liquid Water in Presence of Electric Field . . . 10

1.7 Challenges of High T-jump Experiments on Water . . . 12

1.8 Development of THz Sources . . . 13

1.9 Outline of the Thesis . . . 14

2 Methods 17

2.1 Introduction . . . 17

2.2 Basic Theory: Born-Oppenheimer Molecular Dynamics . . . 18

2.2.1 Born-Oppenheimer Approximation . . . 18

2.3 Born-Oppenheimer Molecular Dynamics . . . 19

2.4 Density Functional Theory . . . 20

2.4.1 A Hybrid Gaussian and Plane Wave DFT Method 21
2.4.2 GPW Forces 24
2.5 Treatment of Electric Field within DFT: Berry Phase Formalism 27
2.6 Coherent X-ray Scattering 28
2.7 Force-Field Molecular Dynamics 29
2.7.1 Short Range Interaction 30
2.7.2 Long Range Interactions 31
2.8 Molecular Dynamics 32
2.8.1 Molecular Dynamics Simulations in Different Ensembles 32
2.8.2 Nosë-Hoover Thermostat 33
2.9 Summary 34

3 Ultrafast Energy Transfer to Liquid Water by Sub-picosecond THz Pulse 37
3.1 Introduction 37
3.2 Method 39
3.3 Results 40
3.3.1 Energy Transfer by THz Pump to Liquid Water 40
3.3.2 Structural Changes in Liquid Water by THz Pulse 43
3.3.3 Vibrational Transformations in Liquid Water by THz Pump: Time-delay Power Spectrum 46
3.4 Conclusion 50

4 Energy Transfer from Solvent to Solute Induced by Highly Intense and Ultrashort THz 51
4.1 Introduction 51
4.2 Methods 52
4.3 Results and discussion 53
4.3.1 Energy Transfer from Solvent to Solute Initiated by a THz Pump Pulse 53

4.3.2 Solvation Dynamics Modification Around the Solute Induced by THz Pump Pulse 57
4.4 Conclusion 60

5 Comparison of *Ab-initio* and Force-field Molecular Dynamics to Describe THz Pulse Interaction **63**
5.1 Introduction 63
5.2 Methods 64
5.3 Results 66
5.3.1 Difference in Potential Energy Surface by *Ab-initio* and Force-field . 67
5.3.2 THz pumping on liquid water: *Ab-initio* and Force-field MD 69
5.3.3 Infrared Pumping on Liquid Water: Ab-initio and Force-Field MD . 75
5.3.4 THz pumping on solute in liquid water solvent: Ab-initio and Force-field MD 76
5.4 Conclusion 77

6 Sub-ps Energy Transfer From A Highly Intense THz Pulse to Water Cluster and Bulk **79**
6.1 Introduction 79
6.2 Computational details 81
6.3 Result and Discussion 82
6.3.1 Interaction of THz Pulse with Water-Cluster 83
6.3.2 THz pulse Interaction with Bulk Water at Different Temperatures and Densities 93
6.4 Conclusion 100

7 Effect of Pulse Parameters on the Energy Transfer Dynamics to Water **101**
7.1 Introduction 101
7.2 Method 103
7.3 Results 104
7.3.1 THz Pump Pulses of Same Pulse Duration but Different Fluences . 104

7.3.2 THz Pump Pulses of Different Frequencies but Same Fluence 106
7.3.3 Effect of Pulse Frequency 108
7.3.4 Far-Infrared Pumping on Liquid Water 110
7.4 Conclusion 115

8 Summary and Outlook 117

Acknowledgment 123

Bibliography 127

LIST OF PUBLICATIONS

2013 *Ultrafast Energy Transfer to Liquid Water by Sub-picosecond High-Intensity Terahertz Pulses: An Ab-Initio Molecular Dynamics Study*
Pankaj Kr. Mishra, Oriol Vendrell, and Robin Santra Angew. Chem. Int. Ed. 52: 13685–13687

2015 *Ultrafast Energy Transfer from Solvent to Solute induced by Sub-picosecond Highly Intense THz Pulses*
Pankaj Kr. Mishra, Oriol Vendrell, and Robin Santra J. Phys. Chem. B 119: 8080

2015 *Sub-picosecond energy transfer from a highly intense THz pulse to water: a computational study based on the TIP4P/2005 model*
Pankaj Kr. Mishra, Oriol Vendrell, and Robin Santra (submitted)

LIST OF BOOK CHAPTER

2014 *Ab initio Molecular Dynamics Simulation of the Interaction of Liquid Water with Sub-Picosecond High-Intensity THz Pulses*
Pankaj Kr Mishra, Oriol Vendrell, and Robin Santra NIC Symposium 2014-Proceedings: 12–13 February 2014, Jülich, Germany

Chapter 1

Introduction

1.1 Introduction : Chemical Reactions

The major portion of research in chemistry focuses on the understanding and controlling of the kinetics, as well as the dynamics of a chemical and biological reactions. In layman's terms, a chemical reaction basically, comprises of 3 different states:
1) reactant state,
2) product state,
3) a path followed from reactant to product state.

By modifying any of these 3 factors, one can not only modify the kinetics but also the dynamics of a reaction. In the last century, there has been significant progress in the development of methods to estimate or predict the kinetics of a reaction. In 1889, Arrhenius elucidated the rate equation of a reaction as $k = A\exp(-\frac{E_a}{RT})$, which provides the reaction rate constant (k) at a given temperature(T) and activation energy(E_a) [1]. But the kinetics of a reaction provides only a macroscopic statistical picture. To observe the time dependent evolution of a reaction, it becomes important to understand the microscopic details of the the dynamics from reactant to product. The advent of Quantum Mechanics made significant contributions in understanding the mechanical events during the reaction by analyzing the inter-atomic potential as a function of inter-atomic distances/angles and then, predicting the classical path based on such potential energy surfaces [2, 3]. Such theoretical studies heralded a new era in the field of chemical kinetics, in which the chemists could now start predicting the dynamical course of a chemical reaction.

Fundamentally, there are three kinds of molecular events which can take place during a chemical or biological process:
1) breaking of a bond,
2) formation of a bond,
3) and, rearrangement or restructuring of a bond.

All these molecular events occur very rapidly, quite often in fs (10^{-15} s) to ps (10^{-12} s) timescales [4]. One of the fundamental problems is to understand how these molecular events are taking place during the course of transition from reactants to products. Many different methods have been developed to explore the detailed dynamics of reactions at the molecular level in last few decades. Examples include the use of molecular beams [5], chemiluminescence [6] and more recently, different laser techniques [7]. Among these techniques, molecular beam techniques gained large attention in 1970s-80s, due to its simplistic approach where a beam of reagent molecules is directed towards co-reagent molecules, and the reactive scattering leads to formation of product. Here, the main idea is to modify the relative kinetic energy of reagents by varying the velocity of one reagent with respect to another, which are involved in "single collisions" [8, 9].

Interestingly, the development of made a twist for such experiments. Rather than using a beam of reagent, a laser was used to excite one of the reagent molecules in laser-molecular beam experiments which influenced the reaction probability significantly. Lasers were also used to initiate a uni-molecular reaction by depositing sufficient energy into a molecule, also known as "half-collision" molecular process [10]. Such experiments played an important role in exploring many interesting features like deducing the nature of potential energy surface of chemical reactions as well as angular, population and energy distribution of products [5]. Such methods were very successful in changing the state of reactant on the potential energy surface which affected the transition path as well as the yield of the product, dramatically. But still these methods were lacking to observe the time-resolved motion between reagents and products. The main reason was the ultrashort life time of these events in comparison to the time-scale of the experiment. In the words of A.H. Zewail, this problem can be phrased as [11]: "The study of chemical reaction can be linked to the task of making a motion picture of a reaction. The trouble thus far with achieving this goal seems to be the problem of too many would be actors who strut upon the stage without proper cue and mumble their lines too rapidly to be understood- for chemical reactions occur with the ease of sticking a match and at a speed so fast (on a subpicosecond time scale for the making of new bonds and breaking of old ones) as to be a severe challenge to the movie-maker who would like to record individual frames." In 1980s, many methods were developed such as absorption [12], emission [13, 14], scattering, and ion spectroscopy [15] to probe the state between reactant and product where unresolved spectra in ps timescale showed the existence of the new states; known as transition state [16]; between reactants and products. But such methods were still lacking the time-resolved information about the transition state due to the time-independent nature of the experiments.

1.2 Femtochemistry

In 1988, A.H. Zewail and collaborators performed a unique pump-probe experiment on alkali halides by using a femtosecond laser [11, 17]. Sodium Iodide (NaI) was transferred from its ground state to the excited state of the potential energy surface with an infrared pump pulse [11]. Then, the internuclear separation of Na and I, along the ionic as well as covalent potential energy surface were followed by probing with an optical pulse of different frequency. In this experiment, the wave function was found propagating back and forth along the ionic as well as covalent potential energy surfaces and the yield of dissociation of NaI was existing along both surfaces. This experiment showed that it is possible to probe inter-atomic vibrations using a femtosecond laser. This idea gave birth to a new field of chemistry which deals mainly with the femtosecond timescale, named as "Femtochemistry".

In femtochemistry, one monitors the reaction using two laser pulses of possibly different colors. The first pulse initiates the reaction and sets the zero of time (clocking). The second pulse probes the product as they separate from each other or as they form new bonds [18]. With the advent of ultrafast laser techniques, transferring the energy in femtosecond timescale permits one to initiate and record the snapshots of a chemical reaction during the process in femtosecond time resolution. This makes it feasible to follow the dynamics of a chemical reaction from reactant state to product state through the transition state. In simple words, such pump-probe technique opens a window of possibility to shoot the molecular movie in fs timescale with sub-angstrom resolution. It is important for clocking a chemical reaction that the length of the trigger pulse to initiate a reaction should be smaller than the dynamics of the reactive event, which allows one to have a well defined clocking time $t = 0$. Such an experimental technique is being used to study many kinds of chemical and biological processes in last couple of decades. For example, the ultrafast photo-dissociation of I_3^- in ethanol solution was shown by using femtosecond time-resolved transient transmission experiments with an UV laser, which resulted in the formation of coherently vibrating di-iodide ions within 300 fs [19]. In another experiment by Schoenlein *et al.*, the femtosecond torsional isomerization of Rhodopsin from 11-cis to 11-trans was excited by a 35 fs pump pulse at 500 nm and probed with a 10 fs pulse that successfully demonstrated the ground state to excited state transition [20]. The photo-ionization of cis-stilbene from cis to trans state, as an example of photo-chemical isomerization in the condensed phase, was studied with a 312 nm pump pulse within a ps timescale [21]. In a different kind of ring opening reaction, gas-phase 1,3-cyclohexadiene was accelerated in the spectroscopic state 1B along Frank-Condon active coordinates by using a low-intensity UV pump of 267 nm and then altered direction before changing over the dark state. This motion was probed by high-intensity photo-ionization at 800 nm along with mass-selective detection of the ion yield [22].

Till now, the use of such pump-probe techniques has been limited mostly to photo-activated processes only e.g. photo-ionization, photo-dissociation etc. The photo-activated reactions constitute only a small fraction of all chemical processes. These processes can be initiated by exciting and pumping energy directly to photo-sensitive mode with a trigger pulse such that on the time-scale, trigger pulse is shorter than the dynamics of the process. But, the application of pump-probe technique to initiate thermally activated chemical processes has not been feasible and so, it is an interesting subject of investigation. The reason for limitations of pump-probe technique on thermal chemical processes will be discussed in detail in coming sections.

1.3 Uni-molecular Reaction Rate Theory: Transition State Theory

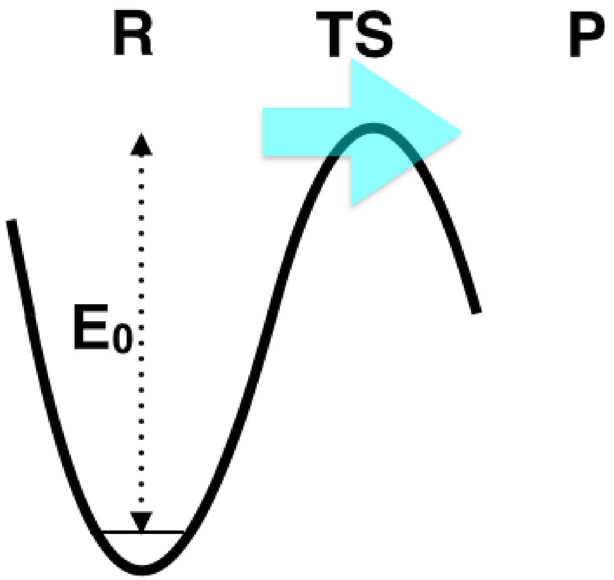

Figure 1.1: Graphical representation of a 1-d energy curve of a reaction along the reaction barrier. R is the reactant state, P is the product state and TS is the reaction barrier.

The simplest theory to determine the rate of a chemical reaction is the uni-molecular transition state theory (TST) [16, 23]. TST assumes that reactants and products lie in two different potential energy states separated by a large energy well(Fig: 1.1). This large energy barrier is known as the transition state (TS). Molecules at the TS correspond to configurations of no return. Starting from the reactants, when and if the reactants reach this critical spatial configuration, it will necessarily proceed to form products. Basically, this theory doesn't pay attention about how the system approaches to the TS or what dynamics it undergoes beyond the TS. On the energy curve of a reaction along the reaction path, TS; "the point of no return" is the point of effective potential maximum. In simple words, any trajectory, which originates at the reactant's side of the barrier has only two choices:
1) Either fails to reach at the TS,
2) or reactants have sufficient energy to reach the TS barrier and form the products.
All the quantum state at the TS are equally probable.

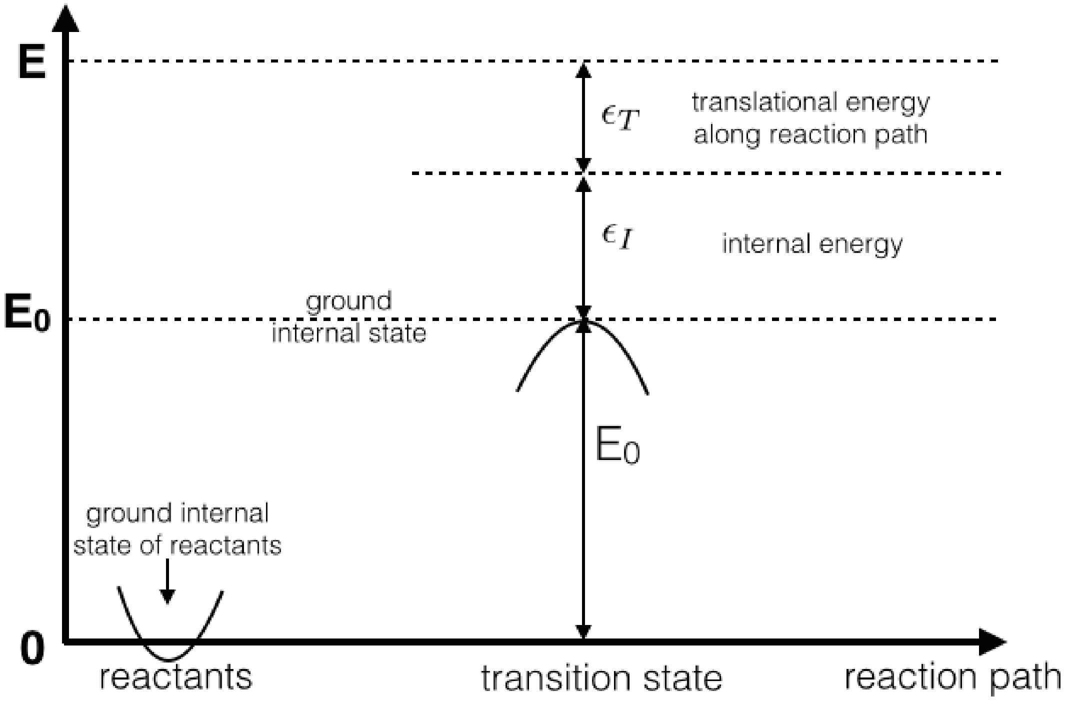

Figure 1.2: Graphical representation of 1-d energy curve of a reaction along the reaction barrier. R is the reactant state, P is the product state and TS is the reaction barrier. Figure is taken from ref: [23].

Let's suppose, E_0 is the minimal energy required to reach the transition state configuration from the ground state reactant(Fig: 1.2). At a given total energy E of reactant, the translational energy for the motion along the reaction coordinate, ε_T, can at most be (E-E$_0$). In general, the available energy, (E-E$_0$), will be distributed between ε_T and energy in other degrees of freedom of the transition state. So, the microcanonical rate constant can be obtained by

$$k(E) = \frac{N^{\ddagger}(E)}{h\rho(E)} \tag{1.1}$$

where $\rho(E)$ is the density of states of the reactants, or in other words, the number of quantum states per unit energy. For reactants having a total energy in the range E to $E + dE$, the rate of passage is determined by the number $N^{\ddagger}(E - E_0)$ of the internal states of the super-molecule at the transition state whose energy ε_I is in the allowed range $(0 \leq \varepsilon_I \leq E - E_0)$. $N^{\ddagger}(E - E_0)$ corresponds only to the bound internal states at the point of no return which excludes the unbound motion along the reaction coordinate. A key assumption made in this derivation is that all quantum states (or phase-space points) with total energy E are equally probable.

When the reactants are in thermal equilibrium at temperature T, the expression for the thermal reaction rate is

$$k(T) = \frac{1}{Q}\int_0^\infty k(E)\rho(E)\exp^{-E/K_BT} dE \tag{1.2}$$

where Q is the partition function of reactants. Q represents the density of states such that the thermal average over a normalized distribution.

$$Q \equiv \int_0^\infty \exp(-E/K_BT)\rho(E)dE. \tag{1.3}$$

By using canonical transition state theory, the thermal rate constant can be written as [16]

$$k(T) = \frac{k_BT}{h}\frac{Q^\ddagger}{Q}\exp^{-E_0/k_BT}, \tag{1.4}$$

where $Q^\ddagger$ is the partition function for the internal states (degrees of freedom excluding the reaction coordinate) at the transition state configuration.

$$Q^\ddagger \equiv \int_0^\infty \exp(-E^{'}/K_BT)\rho^\ddagger(E^{'})dE^{'} \tag{1.5}$$

with $\rho^\ddagger(E^{'})$ being the density of the internal states at transition state

$$\rho^\ddagger(E^{'}) = \frac{d}{dE^{'}}[N^\ddagger(E^{'})] \tag{1.6}$$

Thermally activated processes correspond to the largest fraction of all chemical processes. Most of these thermal chemical processes occur in solution in the ground electronic state. In thermally activated reactions, reactants and products are metastable states separated by large potential energy barriers, compared to thermal energies. So, thermally activated reactions are rare events.

Classically, it is clear from the above analysis that those reactant molecules which do not have the energy $E > E_0$, can not cross the transition state and proceed to products. There are two cases:
1) for $E < E_0$; K(E) = 0 and
2) for $E > E_0$; K(E) = finite value.

For thermal chemical reactions, only a small fraction of molecules contain sufficient energy ($E > E_0$) at a given point of time during the reaction. Molecular distributions at a low temperature have very small fraction of molecules with energy higher than E_0(Fig: 1.3) compared to high temperature distribution. It is not possible to define a clocking time for the reaction with such molecular distributions (P(E)) where there are only small fractions of molecules having energy $E > E_0$. For defining a clocking time, it is required to have molecular distribution of reactant where a significant fraction of reactants has the energy $E(> E_0)$, similar to molecular distribution at high temperatures. So in order to have significantly large fraction of reactant molecules with energy $E > E_0$ to start the reaction,

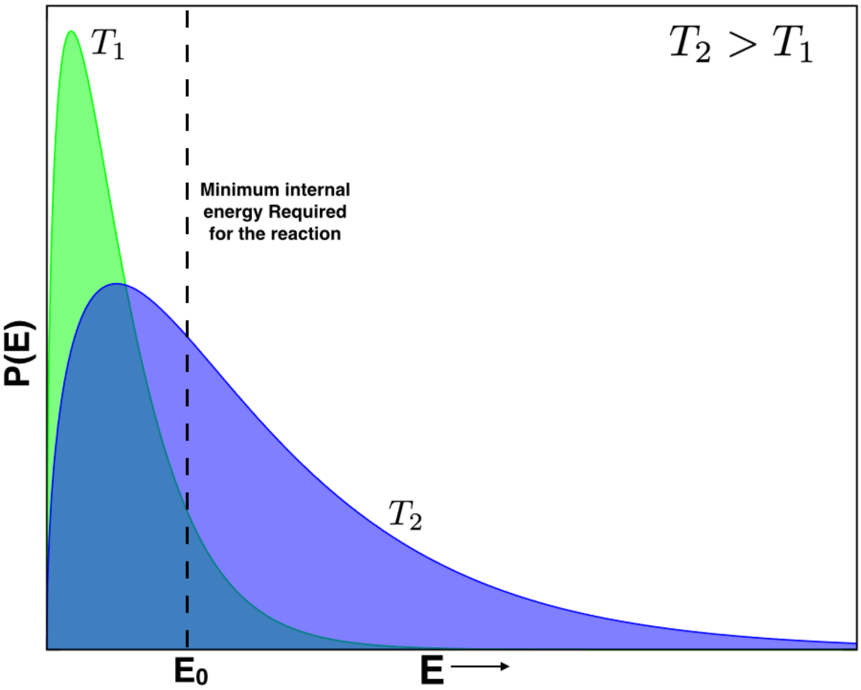

Figure 1.3: Maxwell-Boltzmann Probability distribution of molecules with energy at 2 different temperatures T_1 and T_2 where $T_2 > T_1$.

the molecular distribution needs to shift towards higher energy distribution. Higher energy distribution directly relates to higher temperature according to Maxwell-Boltzmann distribution(eq: 1.7).

$$P(E) = 2\sqrt{\frac{E}{\pi}}(\frac{1}{KT})^{3/2} \exp \frac{-E}{KT} \tag{1.7}$$

To define the clocking time, it becomes important to shift the molecular distribution from low temperature to high temperature within time-scale of the rate constant of reaction using a trigger pump. Thermal chemical processes happen in a solvent environment, mostly in liquid water. The time-dependent rate constant $k(T,t)$ (eq: 1.8) of a reaction, can be changed significantly by changing the temperature and so, corresponding molecular distribution (P(E,t)) within ps time-scale by using a trigger. Then, it will be feasible to clock the thermal chemical reaction.

$$k(T,t) = \int_0^\infty k(E)P(E,t)dE \tag{1.8}$$

For pumping the thermal chemical reactions and defining a clocking time, it is important to create a molecular distribution corresponding to high temperature within a fs to ps time-scale. In the coming sections, many experimental methods to generate temperature-jump will be discussed within ps timescale.

1.4 Temperature-Jump Experiment

1.4.1 Historical Background

Temperature-jump (T-jump) experiments have a long history of being used to study the kinetics of chemical reactions. One of the oldest methods is to generate the T-jump by discharging a high-voltage, low inductance charged capacitor by using a high-voltage dc power supply. For example, G. Tollin *et al.* studied equilibrium binding constants, kinetic and thermodynamic parameters to determine the binding of several flavine, analogs to the apoprotein of azotobacter flavodoxin (snethna flavoprotein), and they observed the evidence for a phosphate-induced protein conformational change [24]. A similar technique was used by M. T. Wilson *et al.* to study the electron-transfer reaction between azurin and cyto-chrome c-551 [25]. An electric heating technique was also used to increase the temperature from 8 to 22°C to determine the dissociation rate of dodecylpyridinium iodide micelles [26]. Such methods were able to generate T-jumps in sub-second timescales.

The use of a laser in T-jump experiments has reduced the time-scale of the processes in study. Lasers started to be used for T-jump experiments in the 1960s. In 1965, H. Staerk and G. Czerlinski used a ruby crystal in a TRG laser to demonstrate heating of some pH-indicator system to within a few nanosecond precision and achieved maximum 23 degrees temperature increment [27] which depend on other factors as well. In another experiment, a laser of 1.06 μm delivering maximum energy 20 J in 25 ns by stimulated Raman effect in liquid nitrogen was used to study the kinetics (forward and backward rate constants) of the Tri-iodide equilibrium [28].

1.4.2 Ultrafast Temperature-Jump Experiments

The advent of tunable femtosecond lasers allows to couple directly to inter and intra-molecular vibrational modes in ultrafast timescales. In an early experiment with the use of laser in 1975, Nd^{+3}-glass laser with a pockels cell Q-switch system was used to generate T-jump in 18 ns by stimulated Raman effect in hydrogen gas with aim to study of nanosecond fast chemical relaxation times [29]. In one of the interesting experiment by Chen *et al.* [30], IR-165 dye in poly-methyl-methacrylate film was pumped with a 1.064 μm near-IR pulse with intensity 9.4 mJ and 25 ps time-length which generated a temperature jump of 105 K in liquid with the bulk heating rate of $\frac{dT}{dt} \approx 10^{12}\ K/s$, whereas the polymer in this solvent was heated even more than 500 K. This experiment took the advantage of the fact that dyes can be doped easily into a wide variety of molecular materials and so, near-IR dyes are attractive to pump with near-IR pulses [30]. Wan *et al.* studied the dynamics of dissociation, recombination and abstraction of ICN in liquids ($CHCl_3$, CH_2Cl_2, and $CDCl_3$) by using a pump pulse in the range of 258-277 nm and probe pulse 387-415 nm. Here, the pump and probe pulses were the second and third harmonics generated by a 70 fs long 774-830 nm IR pulse of energy above 600 μJ at a repetition rate of 1KHz by using a Ti:sapphire amplifier laser system [31]. The advent of laser has provided a platform to transfer large amount of energy to the molecule in ultrafast timescale and find different ways to generate the T-jump. There have been large number of experiments to generate the T-jump in ps to μ by using lasers to study different chemical and biological processes till now.

1.4.3 Pump-probe Studies of Ultrafast T-jump in Liquid Water

Ultrafast T-jump experiments on liquid water have gained lot of attention due to the great importance of water as a solvent. Most of the chemical and biological processes happen in aqueous solvent environment. The main reason is the formation of the strong H-bond networks among water molecules. During the chemical and biological processes, liquid water does not behave as a passive solvent, but rather it provides an active and dynamic environment due to the fluctuation and arrangement of the H-bond network. Ultrafast temperature increments in water can possibly heat up the solute as well and change its molecular distribution ($\rho(E)$) in ultrashort timescales, as discussed above. Water has basically 3 internal vibrational modes: symmetric and anti-symmetric O-H vibrations and the HOH bending mode. Spectroscopically, all these intramolecular vibrations correspond to infrared frequency regime. The O-H vibrational modes of water molecule absorbs light at about 3400 cm^{-1}. Therefore, one can resonantly excite the O-H stretching mode of water with an IR pulse and transfer a large amount of energy into water. Infrared pump has been an effective technique to induce T-jump in liquid water. This provides the T-jump in water in the nanosecond (ns) to microsecond (μs) time scale. Some of the experiments are as follows. Fukumura et al. demonstrated a T-jump of 100 K with pumping of wavelength 1.9 μm laser pulse with energy 300 mJ and pulse duration of 10 ns. Explosive boiling was observed withing 100 ns by time-resolved shadowgraphy and Raman spectroscopy [32]. In another T-jump experiment by Ma *et al.*, the pump pulse of 1.45 μm wavelength with typical 15 μJ energy within 5-20 ps time scale was used to provided a T-jump up to 20 K. This experiment focused on the modification of the H-bond network in water and its effect on conformation and reaction dynamics at the thermal limit for DNA and hydrated cobalt complexes [33]. In a different kind of pump-probe experiment using the synchroton radiation facility at BESSY, Wernet *et al.* presented a T-jump of up to 33K by the use of a 60 fs long pulse of 1mJ energy and observed significant structural changes by probing with an X-ray pulse of width 70 ps [34].

Such T-jump experiments in mixture of other molecules in liquid water have also been used to study the dynamics of chemical and biological processes. For example in experiment by Hobley *et al.*, T-jump of 7K on average with a gradient of 5K in 300 μm was generated in triethylamine-water mixture [35]. This study focused to explore the dynamics of liquid structure relaxation from criticality with the pump and a time-resolved Raman probe and figured out the induction of spinodal demixing of the triethylamine-water binary mixture

[35]. Even laser-induced T-jump has emerged as a promising approach to impulsively trigger protein reactions in water [36, 37]. As an example, very fast kinetics of helix melting in a small 21-residue alanine-based peptide was observed by initiating a folding reaction using an injection seeded Nd:YAD laser-induced T-jump and probed using time-resolved infrared spectroscopy [38].

1.5 X-ray Free Electron Lasers on Liquid Water

In the recent years, the development of X-ray free electron laser (XFEL) sources open the door to generate highly intensed femtosecond X-ray pulses fully synchronized with lasers which allows to watch ultrafast structure dynamics on the femtosecond time-scale with sub-angstrom resolution. There are many XFEL facilities available in the world which include European XFEL in Hamburg, LCLS in Stanford, FLASH in Hamburg and PSI in Villigen etc. One of the main benefit with XFELs is to generate the unique pulse structure with unprecedented brightness, which allows to study fast dynamics in the time domain, thus providing direct access to the dynamic response function S(Q,t) rather than S(Q,ω) [39]. This is of central importance for variety of phenomena such as fast non-equilibrium dynamics initiated by an ultra-short pulse. N. Huse *et al.* performed a solution-phase infrared pump/soft X-ray probe experiment on liquid water at the advanced light source to perform time-resolved soft X-ray spectroscopy at the oxygen K-edge. This experiment successfully probed the hydrogen-bond network of liquid water and a T-jump of 10 K at constant volume was also generated to follow the transient laser excitation and rapid thermalization of vibrational energy [40]. In experiment at European XFEL, G. Grübel *et al.* estimated the expected time scales and count rates of surface X-ray photon correlation spectroscopic (XPCS) experiments for capillary wave dynamics on liquid water [39]. In another pump-probe X-ray diffusion scattering experiment at the XPP beamline at LCLS, a liquid water sample was pumped through a nozzle at different time-delays to study the temporal response of water-heating on ultra-fast time-scales by collecting the diffuse scattering on an area detector [41]. Many other experiments have been performed at XFELs to understand time-resolved structural changes in water structure due to pump pulse and providing a complete new dimension of water. Even XFELs experiments have also been used to study many chemical and biological processes in liquid water environment.

1.6 Computational Studies on Liquid Water in Presence of Electric Field

Liquid Water has been a hot topic to study for computational physicists and chemists from many decades. Even from the early 1960s, the researchers were trying to understand the structure of liquid water using molecular simulations. In 1971, A. Rahman *et al.*

successfully simulated the molecular dynamics of liquid water with density 1 g/cm^3 by solving the classical hamiltonian for a collection of rigid rotors by defining the effective potential energy function [42]. Structural and dynamical predictions of water like radial distribution function, dipole-dipole correlation, self-diffusion etc. with this method were very close to experimental results.

In the past few decades, the application of electric field in molecular simulations has helped to explore the modifications in many properties of water e.g. structure, thermodynamics, dielectric, dynamics, directed diffusion, heating, spectroscopic properties, crystallization and response to biological and chemical processes and application of lasers. Lasers produce the effect of electromagnetic radiation on liquid water. The magnitude of the Lorentz force (qvB) due to magnetic field is several order of magnitude lower than the electric field (qE). Except some cases, it is reasonable assumption to treat the laser pulse as time-varying electric field in the molecular simulations. However, the implementation of electric field during the simulation has faced many challenges in describing the H-bond, proton transfer, high intensity and high frequency laser pulse, polarization effect and the use of periodic boundary conditions. Over the period of time, these limitations have been tried to overcome with development of new simulation methods and better description of potential.

With the development of different force-fields of water, force-field molecular dynamics (FFMD) on water has been very successful in describing many properties and applications. In presence of the strong static electric field, Vigiri presented a FFMD study to demonstrate the orientation of water dipoles along the field direction, breaking of H-bonds, structural and dynamical modifications in cold water system [43]. This study also tried to figure out minimum electric field strength required to break H-bond and make significant structural modification in liquid water (0.1 V/ Å) [43] and water cluster (1.5 V/Å) [43, 44]. The modification of density and polarization density of water was presented in presence of strong electric field (0.0 - 0.1 V/ Å) between two graphite-like plates by using FFMD [45]. In an interesting study, J. Kou *et al.* performed FFMD simulations to study water permeation through single wall nanotubes with electrical interference of frequency range 1-100 THz [46]. He reported the strong modification in the net flow through nanotubes, in H-bonds among waters inside nanotubes and interaction energies. In a recent study, it was shown that water density increases and forms ordered ice-like structures inside carbon nanotube in presence of the strong electric field (0.1 - 0.2 V/Å) by using FFMD [47]. Significantly large changes were also explored in hydrogen bond dynamics, diffusion coefficient and structures of water molecules in system in this study.

But FFMD has many limitations and it lacks the accurate description of energy redistribution among different modes in presence of the electric field in ultra-short timescale, applications of high frequency laser fields and polarization due to strong electric field etc. Such limitations of FFMD have been tried to sort out with different force-field and methodological improvements. Different polarizable water force-field like Martini force-field [48] and Amoeba force-field [49] etc were developed to include the electronic polarizability during FFMD. There are many ab-inito based quantum mechanical polarizable force-fields as well e.g. MCDHO [50], QMPFF2 [51] and TTM2.1 etc. Energy relaxation among different modes of water in presence of the field has not been well captured by fixed charge models or those with 'frozen' bond-angle bending restraints or other holonomic constraints which lead to development of non-equilibrium MD (NEMD) methods. In late 1970s, Ciccotti *et al.* made the foundation of NEMD simulations on liquid water in presence of time-varying electric field [52, 53]. Significant progress in NEMD was made by Evans in 1980s [54, 55] and Zhu *et al.* [56, 57] in modeling constant amplitude laser fields on bulk water. Other methods include enhanced-sampling dynamics [58], path-integral MD [50] and transition path-sampling [59] which are also describing some aspects of time-varying electric-field interaction with liquid water.

With an aim to treat electric field "on the fly" during molecular dynamics to deal with limitations of other methods, Umari and Pasquarello have given the basic theory for ground state DFT in presence of external electric fields under periodic boundary condition (PBC) using the modern theory of polarization (which is known as "Berry-phase" approach) [60]. In an another interesting method to use electric field in DFT, Kunc and Resta treat the Hamiltonian perturbation of the external field in the framework of the local density functional in either linear (weak-field) or nonlinear (stronger field) regimes which has the distinct advantage of circumventing field application in PBC versus aperiodic settings (i.e., useful for both) [61]. *Ab-initio* molecular dynamics (AIMD) can describe well chemical and biological processes with formation and breaking of bonds up to certain limits. Recently, Saitta *et al.* studied bulk water under PBC in presence of strong electric field via Car-parrinallo MD coupled with transition-path sampling [62]. He explored the break-up of water in presence of intense static electric field using the Berry-phase field approach where a change in H-bond length and molecular orientation occurs before 0.35 V/Åand break-up of water started after beyond this threshold intensity. In an another, he also performed the Miller experiments in atomistic simulations to study chemical reactions in presence of strong electric field by AIMD [63]. Till now, these is no study available in presence of time-varying electric field with (ground state) DFT with or without PBC. AIMD simulations in presence of time-dependent electric field will be interesting to study many processes like dissociation, chemical reactivity or electronic-cloud rearrangement.

1.7 Challenges of High T-jump Experiments on Water

As discussed above, the pump-probe experiments for T-jump in water have gained large attention with the advances in lasers and free electron laser (FEL) facilities. However, T-jumps in water in ultrashort timescale have been limited to few 10s of K mostly. The fundamental reason behind the temperature limitation of T-jump experiment is the targeting of a particular intramolecular vibrational mode of water and resonanting it for example, resonating O-H stretching with an IR pulse. An ultrashort sub-ps IR pump pulse transfers the large amount of energy to O-H vibrations and excite it. But at the same time, all other intra- and inter-molecular vibrations remain colder than O-H stretching during the pump. After the pump, O-H vibrational energy starts redistributing to other vibrational modes. T-jump in pumped O-H stretching vibrations become significantly large but the T-jump in whole system remains low once the energy redistribute to other modes. Another important point is the relaxation time-constant of energy among different modes. Time-constant of energy relaxation of among O-H intramolecular mode is 0.75 ps [64, 65] and time constant of the energy transfer from rotational to translational mode is 0.42 ps [66, 67]. So, the energy relaxation among different modes happens in ps time-scale and consequently, the depletion of H-bond also happens in the similar time-scale. To activate thermal chemical reactions, few 1000s of K of T-jump is required in the water solvent. As an example, a reaction barrier ΔE =10 kcal/mol, which should be considered a small barrier in terms of reaction kinetics, corresponds to a temperature of $T = \Delta E/k_B \approx$5000 K. In terms of wavenumber, 5000 K of energy corresponds to 3475 cm^{-1} which is very close to O-H excitation per water molecule. If suppose, all water molecules in the system get on average one photon at 3450 cm^{-1}, the T-jump of the system will be quite large. But still, the question remains that how fast other vibrational modes can gain energy. Along with this, it is also unanswered that how fast the energy of solvent is going to redistribute to the solute and whether the solute absorbs the energy directly at this frequency or not. Transferring large amount of energy in ps time-scale via targeting O-H vibrations to create a T-jump of 1000s of K can also break the molecular bonds. The pump-probe experiment on a condensed phase thermal reaction will be possible only if the solvent can be heated up to few 1000s K in fs - ps timescale. This force us to think a new possible pumping technique, which is not mode-selective in transferring the energy to water and also very similar to heating process.

Some studies suggest that the THz interacts with the collective modes of water [68]. None of the intramolecular vibrations can be targeted and excited directly by THz pump. Ashihara *et al.* reported the absorption cross-section at THz frequencies from 0.1 THz to 10 THz (3 mm to 30 μm). Simulation study by M. Heyden [68] also presents that the solvation shell structure and H-bond network due to the presence of a solute are modified by a low intensity THz pulse. Such studies suggest that the THz pulse interacts with collective modes of water at low intensity. These studies open a domain of pump-probe experiment where pump can be mode-unselective in transferring the energy and affect the solvation shell structure of the system even in the absence of well-defined resonances.

1.8 Development of THz Sources

In last few years, there have been significant advancements in the technology to generate the ultrashort and high power THz sources. Still it is not yet fully feasible to generate low cost and portable room temperature THz sources operating in wide range of frequency and peak power. However, with the development of lasers, high-speed electronics and new materials, new potential THz sources are emerging to achieve the THz pulses for a range of desired specifications. There are basically two kinds of THz sources. One kind of sources are broadband pulsed THz sources, which are generated by the excitation of different materials with ultrashort laser pulses [69]. Many different mechanisms have been used to generate THz radiation which include photo-carrier acceleration in photoconducting antennas, second-order non-linear effects in electro-optic crystals, plasma oscillations [70] and electronic non-linear transmission lines [71]. Others are narrow band THz sources which produce low-power continuous-wave THz radiation and are based on the generation through up-conversion of lower-frequency microwave oscillators [69]. Extremely high-power THz emission has also been demonstrated using free-electron lasers with energy-recovering linear accelerators [72]. Due to low conversion efficiencies, pulsed THz beam power is limited from nano to microwatt range. For example, photoconductive emitters can produce THz pulse of 40 μW [73] (THz peak amplitude of 95 V/cm) with a bandwidth as high as 4 THz [74].

In an interesting experiment by C. P. Hauri *et al.* [75], phase-locked single-cycle THz pulses were generated in the frequency range of 0.1 to 5 THz which can have peak field amplitude up to 42MV/cm and 14 Tesla. The scheme here was based on a Cr:Mg_2SiO_4 laser using an uncooled organic crystal. This pulse carried 0.9 mJ of energy within a 400 mm^2 focal spot which provided the intensity of 10^{12} W/cm^2. In an another experiment to generate a high power THz sources, R. Huber *et al.* [76] generated THz waveforms with peak fields of 72 MV/cm by driving coherent interband polarization combined with dynamical Bloch oscillations in semiconducting gallium selenoid. Using this technique, it was possible to generate THz pulse in the frequency region of 10-30 THz with power per unit area of 10^{13} W/cm^2. Hegmann and co-workers demonstrated the generation of 1.5 μJ energy per pulse, single-cycle 3 terahertz pulses by optical rectification from a large-aperture of 75 mm diameter, 0.5 mm thick, (110) ZnTe single crystal wafer using a 100 Hz Ti:sapphire laser source [77]. In a recent experiment, Shalaby *et al.* generated low frequency THz ($<$ 5THz) radiation confined to a diffraction-limited spot size by using a wavefront manipulation concept with focusing optimization [78]. He presented an extremely bright PW/m^2 level THz radiation with peak fields upto 8.3 GV/m and 27.7 T which is higher than any other system. So, frequency and intensity of the THz pulse are the important parameters, which is not easy to tune to achieve pulses of desired specifications. It was observed that high intensity can be achieved for high frequency pulses whereas peak power per unit area decreases for low frequency pulses.

1.9 Outline of the Thesis

In our work, we investigated the response of liquid water to highly intense and ultrashort THz pump and possible T-jump experiments. We also put an effort to understand the pump-probe experiment on thermal chemical process by exploring the dynamical response of solvent-solute to such THz pulse. After this introduction, this dissertation consists of 7 more chapters, which are outlined in the following.

In the chapter; 2; all the theoretical formalism and methods used for the calculation will be summarized to provide a complete and comprehensive overview. I will recapitulate the fundamentals of Born-Oppenheimer based Ab-initio Molecular Dynamics (AIMD) as implemented in the CP2K molecular dynamics package. A brief discussion will also be made on the use of hybrid basis sets and psudopotential which play a crucial role in AIMD. All the bulk simulations were performed with the use of periodic boundary condition where the Berry-Phase approach was used for AIMD in the presence of an electric field. An important aspect of the whole study is the partition of total kinetic energy into different components. The concept of coherent x-ray scattering for the structural analysis of liquids will be introduced briefly to signify its importance for the structural information. Along with this, the role of radial distribution function is worth mentioning for the solvation shell study. The method behind the calculation of time-resolved power spectrum will be briefly introduced as well. The last part of this chapter will also touch the concept of force-field molecular dynamics. A short description of force fields will be provided along with a particular water model which was used in the reported simulations.

After discussing the fundamental of methods and preparing the ground, I will focus on the response of water solvent to a highly intense and ultrashort THz pulse. Chapter 3 will focus on the study of THz pulse pumping on liquid water. The effect of THz pulse on liquid water was studied by analyzing the kinetic energy gain in different modes of water. The large energy gain causes significant structural changes in liquid water which can be studied by coherent x-ray scattering as well as the radial distribution function. The energy gain by different modes in water bring out the changes in the internal vibrations. The changes in internal vibrations due to THz pump are analyzed by the time-resolved power spectrum. The whole analysis of liquid water proves that a highly intense and ultrashort THz pump is able to create a hot and non-equilibrium gas like liquid water. In this chapter, I will provide a discussion for the possibility THz pump - X-ray probe and THz pump - IR probe experiments on liquid water.

A hot and gas-like liquid water environment created by such ultrashort and highly intense THz pump pulse provides the motivation to explore the response of a solute in such environment. Chapter 4 will focus on the response of phenol, as an example solute in aqueous solvent interacting with the THz pump. This chapter will present a comparative picture of energy transfer to solute by THz pulse in the gas phase and in aqueous environment. I will also analyze the modification in the dynamics between solvent-solute due to the pump-pulse. We will show that such heating mechanism is not selective to any particular solute, rather it presents a general mechanism to transfer large energy to the solute in an aqueous environment.

The previous will present the effect of THz pulse pumping by Ab-initio Molecular

Dynamics. In the chapter: 5, I will present the THz pumping on liquid water via force-field molecular dynamics. A comparison between force-field and *Ab-initio* molecular dynamics (AIMD) for THz pumping will be discussed. I will discuss about the limitations of using parameterized force fields in comparison to AIMD calculations. This chapter will also focus on discussing different physical properties of water important in presence of the electric field which FFMD lacks to describe accurately.

In the Chapter 6, a microscopic study to transfer the energy to water clusters by THz pulse will be discussed. The THz interaction of water molecules, from gas phase to liquid phase will be analyzed. We will explore the effect of THz pumping on H-bonding from cluster to bulk. We will discuss the fundamental of energy transfer by THz pump. This chapter will also focus on the effect of initial temperature and density of water system on the energy gain from the THz pump. The aim will be to understand the effect of THz pumping on different phases of water.

After providing the picture of energy transfer due to a THz pump previous chapters, Chapter: 7 will explore different pulse conditions ranging from few to several THz and various fluences and pulse durations. THz sources are still limited by the techniques to produce the desired high intense and ultrashort THz pulses. We will discuss the effect of frequency, intensity and energy of THz pulse on T-jump experiment. Possibility of generating T-jump by resonating the librational modes will also be investigated in this chapter. This chapter will be helpful to experimentalists during the design of a possible experiments based on the existing sources.

Finally, Chapter:8 will present a summary and outlook of the work.

Chapter 2

Methods

2.1 Introduction

Within the last several decades, the development of quantum mechanics, electronic structure methods and computational statistical mechanics along with high power computing facilities made feasible to investigate "on the fly" statistical and dynamical properties of atoms and molecules in very short timescale. However, due to the complexity and rigorousness of calculation required for a system bigger than hydrogen atom, the full quantum mechanical treatment of nuclei and electrons is not yet possible due to the limitations of existing computational techniques and resources. These limitations necessitated the development of approaches like density functional theory and Hartree-Fock, which treats only electrons quantum mechanically. These methods are extendable to systems with few 100s of atoms. In attempts to simulate bigger system with few thousands of atom, force-fields methods were developed in which atoms are treated like point particles with partial charges moving on a parameterized potential energy surface.

In this chapter, I will present a brief and comprehensive summary of different computational tools used in our study. Born-Oppenheimer based Ab-anitio Molecular Dynamics will be recapitulated as implemented in QUICKSTEP [79] module of CP2K molecular dynamics package. A short description will also be provided for the methods used for calculation of different properties like coherent x-ray scattering and power spectrum during the study. In the later part, there will also be a short discussion focused on force-field molecular dynamics via LAMMPS.

2.2 Basic Theory: Born-Oppenheimer Molecular Dynamics

The non-relativistic time-dependent Schrödinger equation for a system can be written as

$$H\Psi(\{\mathbf{r}_i\},\{\mathbf{R}_I\};t) = i\hbar\frac{\partial}{\partial t}\Psi(\{\mathbf{r}_i\},\{\mathbf{R}_I\};t) \tag{2.1}$$

in its position representation for the wave function $\Psi(\{\mathbf{r}_i,\mathbf{R}_I\})$ in conjunction with Hamiltonian

$$\begin{aligned}
H &= \hat{T}_N + \hat{T}_e + \hat{V}_{ee} + \hat{V}_{eN} + \hat{V}_{NN} && (2.2)\\
&= -\sum_I \frac{\hbar^2}{2M_I}\nabla_I^2 - \sum_i \frac{\hbar^2}{2m_e}\nabla_i^2 + \sum_{i<j}\frac{e^2}{|\mathbf{r}_i-\mathbf{r}_j|} - \sum_{I,i}\frac{e^2 Z_I}{|\mathbf{R}_I-\mathbf{r}_i|} + \sum_{I<J}\frac{e^2 Z_I Z_J}{|\mathbf{R}_I-\mathbf{R}_J|} && (2.3)\\
&= -\sum_I \frac{\hbar^2}{2M_I}\nabla_I^2 - \sum_I \frac{\hbar^2}{2m_e}\nabla_i^2 + V_{n-e}(\{\mathbf{r}_i\},\{\mathbf{R}_I\}) && (2.4)\\
&= -\sum_I \frac{\hbar^2}{2M_I}\nabla_I^2 + \hat{H}_e(\{\mathbf{r}_i\},\{\mathbf{R}_I\}) && (2.5)
\end{aligned}$$

acting on the electronic $\{\mathbf{r}_i\}$ and nuclear $\{\mathbf{R}_I\}$ degree of freedom. The terms $\hat{T}_N$ and $\hat{T}_e$ are the kinetic energy operator of nuclei and electrons, respectively. The operators $\hat{V}_{ee}$, $\hat{V}_{eN}$ and $\hat{V}_{NN}$ are representing the electron-electron, electron-nuclear, and nuclear-nuclear coulombic interactions, respectively. The Hamiltonian $\hat{H}_e(\{\mathbf{r}_i\},\{\mathbf{R}_I\})$ comprises of all electronic energy contributions along with its nucleus interaction.

2.2.1 Born-Oppenheimer Approximation

The Born-Oppenheimer approximation (also known as "adiabatic approximation") is based on the fact that the electrons are much lighter objects than the nuclei. The electron-nucleus mass ratio M_I/m_e is ≈ 1836 for a proton and to O(4) for typical elements like carbon or oxygen. Due to the smaller mass, electrons are bounded within the potential of the nuclei. Electrons move more rapidly than the heavy nuclei themselves, but on average follow their motion.

This approximation is numerically by making an ansatz for the time-independent wave function $\Psi(\{\mathbf{r}_i\},\{\mathbf{R}_I\})$, in terms of a separate wave function of the nuclei $\chi(\{\mathbf{R}_i\})$ and of the electron $\Phi(\{\mathbf{r}_i\};\{\mathbf{R}_i\})$

$$\Psi(\{\mathbf{r}_i\},\{\mathbf{R}_I\}) = \chi(\{\mathbf{R}_I\})\Phi(\{\mathbf{r}_i\};\{\mathbf{R}_I\}) \tag{2.6}$$

The assumption of heavier nuclei allows us to neglect the nuclei coordinates $\{\mathbf{R}_I\}$-dependence of $\Phi(\{\mathbf{r}_i\};\{\mathbf{R}_I\})$ for electrons and have only parametric dependence. $\Phi(\{\mathbf{r}_i\};\{R_I\})$ has only parametric dependence on $\{R_I\}$ to follows nuclear motion. This leads to separating of the entire electronic problem to a momentary set of nuclear coordinates. Thus, the Schrödinger equation for the nuclei, which move on an effective potential surface, that is responsible for their interaction with the electrons can be written by separating eq: 2.6 into two equations (eq: 2.7 and 2.8).

$$(\hat{T}_e + \hat{V}_{ee} + \hat{V}_{eN}(\{R_j\}))\Phi(\{\mathbf{r}_j\};\{R_J\}) = E_n(\{R_I\})\Phi(\{\mathbf{r}_i\};\{R_I\}) \tag{2.7}$$

$$(\hat{T}_N + \hat{V}_{NN} + E_n(\{\mathbf{R}_I\}))\chi_{n\nu}(\{\mathbf{R}_j\}) = E_{n\nu}\chi_{n\nu}(\{\mathbf{R}_j\}) \tag{2.8}$$

As non-adiabatic interaction, the parametric dependence of $\hat{V}_{eN}$ on $\{R_j\}$ (eq: 2.7) requires that the electronic eigenvalues $(E_n(\{R_I\}))$ are also functions of $\{\mathbf{R}_j\}$. n and ν are the quantum numbers of electrons and nuclei. The $E_n(\{R_j\})$ as function of the coordinates, acts as an effective potential of the adiabatic electron-nuclei interaction. This effective potential depends on the quantum state occupied by the electronic subsystem. Together with the repulsive Coulombic interaction between the nuclei, V_n provides the effective potential on which the electrons move.

$$V_n(\{R_j\}) = V_{NN}(\{R_j\}) + E_n(\{R_j\}) \tag{2.9}$$

The effective potential $V_0(\{R_j\})$ corresponds to the electronic ground state.

2.3 Born-Oppenheimer Molecular Dynamics

In the Born-Oppenheimer Molecular Dynamics (BOMD), the nuclei evolve in time only on the ground electronic surface (known as Born-Oppenheimer surface) with $V_0(\{R_j\})$ [80]. So, only those processes can be studied with BOMD for which the dynamics is happening in the ground state. BOMD simulation is divided in two main steps:
1) determining the ground states by solving the electronic structure problem for a given nuclear positions at a given instant of time; and
2) solving Newton's equations for the nuclei.
Thus, step 1 is to solve a time-independent Schrödinger equation. Concurrently, the nuclei are propagated using Newton's equations of motion. So in BOMD, the time-dependence of the electronic structure is only the consequence of nuclear motion, rather than being an intrinsic feature of the electronic system. The resulting method is defined by

$$M_I\ddot{\mathbf{R}}_I(t) = -\bigtriangledown_I min_{\Psi_0}\{\langle\Psi_0|H_e|\psi_0\rangle\} \tag{2.10}$$

$$E_0\psi_0 = H_e\psi_0 \tag{2.11}$$

for the ground electronic state. The minimum of $\langle H_e \rangle$ has to be achieved in each BOMD step. There are different methods available to determine the electron structure and find the $min\langle H_e \rangle$, e.g., Hartree-Fock and density functional theory (DFT). In our case, CP2K uses the DFT method to solve the electronic structure, which is implemented in the QUICKSTEP module to solve the electronic structure.

2.4 Density Functional Theory

Density Functional Theory (DFT) is a theory of electronic structure based on the electronic density rather than wave function. It can be turned into an efficient computational tool by using the Hohenberg-Kohn theorems [81] and Kohn-Sham [82] formulation to solve the electronic structure for many body systems. It reduces computational cost significantly compared to any other electronic structure method and provide a relatively good accuracy that's why DFT is the main method of choice for "on the fly" AIMD in modern application. The properties in DFT are obtained by the use of *functionals* of electronic density. This section of the chapter follow the ref: [79, 83] closely.

The total energy (E^{tot}) of a molecular system is given by the sum of the internuclear interaction ($E^{nuc-nuc}$) and the electronic energy (E^{el}) for a fixed set of nuclear coordinates ($\{\mathbf{R}\}$) [83].

$$E^{tot} = E^{nuc-nuc}(\{\mathbf{R}\}) + E^{el}[\{R\}, \rho], \tag{2.12}$$

In the Kohn-Sham (KS) [82] formalism of density functional theory, the electronic energy can be written as

$$E^{el}[\rho] = E^{T}[\rho] + E^{V}[\rho] + E^{H}[\rho] + E^{XC}[\rho], \tag{2.13}$$

where $E^T[\rho]$ is the kinetic energy, $E^V[\rho]$ is energy due to the electronic interaction with the nuclei (electrostatic interaction), and, $E^H[\rho]$ and $E^{XC}[\rho]$ are the electronic Hartree and exchange-correlation (XC) energies, respectively. The electronic density (ρ) can be defined in terms of the spin-restricted orbitals $\{\Psi_i\}$, with their respective occupation number f_i,

$$\rho = \sum_i f_i |\Psi_i|^2. \tag{2.14}$$

In this formalism, the orbitals are expanded in a *basis set* of localized functions φ_μ, which are represented e.g. in terms of cartesian Gaussians. For condensed phase system, φ_μ should be periodic in space to satisfy the periodic boundary condition [84]. The periodic function ($\varphi_\mu^{\mathbf{P}}$) can be achieved by extending φ_μ over all its periodic images 2.15.

$$\varphi_\mu^{\mathbf{P}}(\mathbf{r}) = \sum_{\mathbf{i}} \varphi_\mu(\mathbf{r} - I_i), \tag{2.15}$$

where the sum is over all triplets of positive and negative integers, $\mathbf{i} = i, j, k$. $\mathbf{I}_i = i\mathbf{I}_1 + j\mathbf{I}_2 + k\mathbf{I}_3$, and $\mathbf{I}_1, \mathbf{I}_2, \mathbf{l}_3$ are the three vectors that extend over the periodical images of the unit cell. In terms of the basis function, the KS orbitals are written as

$$\Psi_i(\mathbf{r}) = \sum_{\mu} C_{\mu i} \varphi_{\mu}^{P}(\mathbf{r}), \tag{2.16}$$

which ensures the periodicity of the $\Psi_i(\mathbf{r})$'s. Using the concept of orbitals, the kinetic energy of the auxiliary non-interacting system can be written as,

$$E^T = \sum_i f_i \langle \Psi_i | - \frac{\Delta}{2} | \Psi_i \rangle. \tag{2.17}$$

The Hartree energy can also be written as

$$E^H[\rho] = \frac{1}{2} \int d\mathbf{r} \int d\mathbf{r}' \frac{\rho(\mathbf{r})\rho(\mathbf{r}')}{|\mathbf{r} - \mathbf{r}'|}, \tag{2.18}$$

and the exchange-correlation energy by

$$E^{XC}[\rho] = \int d\mathbf{r} \rho(\mathbf{r}) \varepsilon_{XC}[\rho](\mathbf{r}), \tag{2.19}$$

where $\varepsilon_{XC}[\rho]$ is the exchange and correlation energy density functional.

An expansion of an atomic all-electron density or wave function using the plane waves is computationally inefficient due to the use of same number of grid points required to describe empty space as well as atomic region. However, for most of the chemical events, such as bond breaking or formation, an accurate description is required only for the valence electrons. One can eliminate the core electrons by introducing atomic pseudopotentials [85], which describe the interaction of the valence electrons with the nuclei and the core electrons by effective potentials. $E^V[\rho]$ is described by norm-conserving pseudopotentials ($\mathrm{V}^{PP}(\mathbf{r})$) with a potential split in a local part $V_{loc}^{PP}(r)$ and fully non-local $V_{nl}^{PP}(\mathbf{r}, \mathbf{r}')$. In our study, we used the pseudopotentials developed by Geodecker, Teter, and Hutter (GTH) [86] optimized for the gradient-corrected exchange-correlation functionals of Perdew, Burke, and Ernzerhof (PBE).

2.4.1 A Hybrid Gaussian and Plane Wave DFT Method

The basis set plays an important role in the calculation of energy using the Kohn-Sham orbitals. In conventional DFT, the plane waves (PWs) have been used extensively as a basis set for the expansion of Kohn-Sham (KS) orbitals. PWs approaches have been successful due to many advantages like, the independence of PWs from atomic position, no superposition error due to unbiasness towards atomic and empty region, straight-forward process to check convergence and simplified algebraic manipulations with fast Fourier transform techniques. However PWs also have many disadvantages, which include the requirement of large number of PWs basis sets to describe the rapid variation of the wavefunctions near the nuclei and the high computation cost due to the use of same density of function to describe the empty regions and atomic region. Whereas, atomic region can be described well with the Gaussian basis set with significantly small number of basis set.

To overcome the complexities involved with the use of PWs basis sets, a hybrid Gaussian and Plane Wave (GPW) DFT method was developed to use the advantages and remove the disadvantages of PWs by using Gaussian basis sets. GPW method combines two different basis sets, Gaussian functions and plane waves. It uses the Gaussians functions to represent the KS orbitals with which one can evaluate analytically all the density independent terms of the KS Hamiltonian, in a fairly straightforward and efficient way. Over the years since DFT was first introduced, there have been significant developments in producing the basis sets including many orbitals and even polarization e.g. DZVP, TZVP, TZV2P, QZV2P and QZV3P etc. For the use in large scale molecular simulations, one requires to have a Gaussian basis set that works well with gas phase systems, interfaces, and liquids, with good performance for total energies, geometries, and hydrogen bonding energies.

One therefore uses PWs as an auxiliary basis set that represents the full charge density. This simplifies the calculation of the Hartree and exchange and correlation potentials, which so far has been the achilles heel of Gaussian based calculations. Furthermore, the use of pseudopotentials eliminates cusps at the nuclei and thus, reducing the number of Gaussians needed to represent the wavefunctions. This also has a beneficial effect on the basis set superposition error. Pseudopotentials become essential for efficient electronic structure calculations because of the following. Firstly, the elimination of core electrons reduces the number of orbitals, to be calculated. Secondly, the pseudo-wave functions are much smoother in the core region than the all-electron wave functions, and the number of basis functions are thus, reduced. Another advantage of using pseudopotentials is that one only needs to describe valence electrons, with that number of electrons, basis functions, and primitive Gaussians per atom are smaller than in the corresponding all-electron case.

Energy Functional

The heart of the GPW method [83] is to use two different representations of the electron density. The first representation of the electron density $\rho(\mathbf{r})$ is based on an expansion in atom centered, contracted Gaussian functions

$$\rho(\mathbf{r}) = \sum_{\mu\nu} P^{\mu\nu} \varphi_\mu(\mathbf{r}) \varphi_\nu(\mathbf{r}), \tag{2.20}$$

where $P^{\mu\nu}$ is a density matrix element, and $\varphi_\mu(\mathbf{r}) = \sum_i d_{i\mu} g_i(\mathbf{r})$ with primitive Gaussian functions $g_i(\mathbf{r})$ and corresponding contraction coefficients $d_{i\mu}$. The second representation employs an auxiliary basis of plane waves, which is given by

$$\tilde{\rho}(\mathbf{r}) = \frac{1}{\Omega}\sum_{\mathbf{G}} \tilde{\rho}(\mathbf{G}) exp(i\mathbf{G}\cdot\mathbf{r}), \tag{2.21}$$

where Ω is the volume of the unit cell, and $\mathbf{G}$s are the reciprocal lattice vectors. The expansion coefficients $\tilde{\rho}(\mathbf{G})$ are such that $\tilde{\rho}(\mathbf{r})$ is equal to $\rho(\mathbf{r})$ on a regular grid in the unit cell. This choice allows for a rapid conversion between $\rho(\mathbf{r})$, $\tilde{\rho}(\mathbf{r})$ and $\tilde{\rho}(\mathbf{G})$ using an efficient mapping procedure and fast Fourier transform.

Using this dual representation, the Kohn-Sham DFT energy expression [81, 82] (eq: 2.13) in GPW framework can be written as

$$\begin{aligned} E[\rho] =& E^T[\rho] + E^V[\rho] + E^H[\rho] + E^{XC}[\rho] + E^{II} \\ =& \sum_{\mu\nu} P^{\mu\nu}\langle\varphi_\mu(\mathbf{r})| -\frac{1}{2}\nabla^2|\varphi_\mu(\mathbf{r})\rangle \\ &+ \sum_{\mu\nu} P^{\mu\nu}\langle\varphi_\mu(\mathbf{r})|V_{loc}^{PP}(r)|\varphi_\mu(\mathbf{r})\rangle \\ &+ \sum_{\mu\nu} P^{\mu\nu}\langle\varphi_\mu(\mathbf{r})|V_{nl}^{PP}((r)\mathbf{r}')|\varphi_\mu(\mathbf{r}')\rangle \\ &+ 2\pi\Omega\sum_{\mathbf{G}}\frac{\tilde{\rho}^*(\mathbf{G})\tilde{\rho}(\mathbf{G})}{\mathbf{G}^2} + \int \epsilon_{XC}(\mathbf{r})d\mathbf{r} \\ &+ \frac{1}{2}\sum_{I\neq J}\frac{Z_I Z_J}{|\mathbf{R}_I - \mathbf{R}_J|} \end{aligned} \tag{2.22}$$

The interaction energies of the nuclei charges Z_A and positions $\mathbf{R}_A$ is denoted by E^{II}.

Electrostatic Energy

The electrostatic energy has contributions from nuclei and electrons. In a periodic system, this is calculated by a conditionally converging sum in which the separate contributions of ions and electrons are infinite.

$$E^{ES} = E^{ES}_{shortrange} + E^{ES}_{longrange} \tag{2.23}$$

$$= \int V_{loc}^{PP}\rho(\mathbf{r})d\mathbf{r} + \frac{1}{2}\sum_{i\neq j}\frac{Z_i Z_j}{|\mathbf{R}_I - \mathbf{R}_J|} + 2\pi\Omega\sum_{G}\frac{\tilde{\rho}^*(\mathbf{G})\tilde{\rho}(\mathbf{G})}{\mathbf{G}^2} \tag{2.24}$$

using the Ewald sum method [87]. Here, $V_{loc}^{PP}(r)$ is norm-conserving, separable, dual-space GTH pseudopotentials which consist of a local part including a long-ranged (LR) and a short-ranged (SR) term.

$$V_{loc}^{PP}(r) = V_{loc}^{LR}(r) + V_{loc}^{SR}(r) \tag{2.25}$$

The long range part of all electrostatic interactions is treated in Fourier space, whereas the short range part is treated in real space. In QUICKSTEP, the electrostatic energy is given by

$$\begin{aligned}
E^{ES} &= \int V_{loc}^{SR}(r)\rho(\mathbf{r})d\mathbf{r} \\
&+ \frac{\Omega}{2}\sum_{G}\tilde{\rho}_{tot}^{*}(\mathbf{G})v^{H}(\mathbf{G}) \\
&+ \frac{1}{2}\sum_{i\neq j}\frac{Z_I Z_J}{|\mathbf{R}_I-\mathbf{R}_J|}erfc[\frac{|\mathbf{R}_I-\mathbf{R}_J|}{\sqrt{R_I^{c2}+R_I^{c2}}}] \\
&- \sum_{i}\frac{1}{\sqrt{2\pi}}\frac{Z_I^2}{R_I^c} \\
&= \int V_{loc}^{SR}(r)\rho(\mathbf{r})d\mathbf{r} + E^{H}[\rho_{tot}] + E^{ovrl} + E^{self}
\end{aligned} \tag{2.26}$$

where *erfc* is the complementary error function, $v^H(\mathbf{G})$ is the Hartree potential ($= 4\pi\tilde{\rho}_{tot}(\mathbf{G})/\mathbf{G}^2$), and $\tilde{\rho}_{tot}(\mathbf{G})$ is total charge distribution ($=\tilde{\rho}(\mathbf{G})+\tilde{\rho}_C(\mathbf{G})$). $E^H[\rho_{tot}]$ is total Hartree energy, E^{ovrl} is the overlap energy and E^{self} is self-energy, respectively.

Exchange-Correlation Potential Energy

An critical element of DFT is the approximate exchange and correlation function (E^{XC}), which is calculated normally as

$$E^{XC}[\rho] = \int \epsilon_{XC}(\rho_{\uparrow}(r), \rho_{\downarrow}(r), \triangle\rho_{\uparrow}(r), \triangle\rho_{\downarrow}(r), \tau_{\uparrow}, \tau_{\downarrow})d\mathbf{r} \tag{2.27}$$

where τ is kinetic energy density. We used PBE exchange-correlation functional which exists in QUICKSTEP.

2.4.2 GPW Forces

Deriving the Kohn-Sham Matrix from the GPW Energy

In this section, we present the computation of the the exact derivative $H_{\mu\nu} = \partial E/\partial P^{\mu\nu}$ of the total energy by taking into the account all approximations that arise from the Gaussian based density $\rho(\{P^{\mu\nu}\})$ to the density represented on the grid $\tilde{\rho}(\{P^{\mu\nu}\})$. This includes mapping from the Gaussian basis to the grid using finite radii, use of multi-grids and of grid based methods to compute $\bigtriangledown\tilde{\rho}(r)$. Here, the notation $\tilde{\rho}_i$ will denote a value of $\tilde{\rho}(r)$ on a particular grid point with coordinates r_i, using a single index i for notational convenience. Truncation to a finite radius of products $\phi_\mu(r)\phi_\nu(r)$ is equivalent to summing over a subset $\{\mu', \nu'\}$ of $\{\mu, \nu\}$ in the definition

$$\tilde{\rho}_i = \Sigma_{\{\mu',\nu'\}} P^{\mu',\nu'} \phi_{\mu'}(r_i)\phi_{\nu'}(r_i). \tag{2.28}$$

The derivative of $E(\{P^{\mu\nu}\}, \tilde{\rho}(\{P^{\mu\nu}\}))$ will be obtained explicitly using the chain rule as

$$H_{\mu\nu} = \frac{\partial E}{\partial P^{\mu\nu}} + \frac{\partial E}{\partial \tilde{\rho}_i}\frac{\partial \tilde{\rho}_i}{\partial P^{\mu\nu}}, \tag{2.29}$$

where summation over repeated indices, such as i, is implicit. $\frac{\partial E}{\partial \tilde{\rho}_i}$ is the potential on the grid.

Forces on the Ions

Forces on the ions can be determined explicitly by calculating the gradient of the GPW energy according to equations: 2.22 and 2.26 with respect to the atomic positions. This derivative takes into account the atom centered nature of the Gaussian basis set and the orthogonality constraint on the wave functions.

The derivative of the density independent terms overlap energy (E_{ovrl}) and self energy E_{self} described in eq: 2.26, are given by

$$\begin{aligned} \bigtriangledown_I E^{ovrl} = & \sum_{J \neq I} \frac{\mathbf{R}_j - \mathbf{R}_I}{|\mathbf{R}_j - \mathbf{R}_I|^2} \\ & \times \{ \frac{Z_I Z_J}{|\mathbf{R}_j - \mathbf{R}_I|} erfc[\frac{|\mathbf{R}_j - \mathbf{R}_I|}{\sqrt{R_I^{c2} + R_J^{c2}}}] \\ & + \frac{2}{\sqrt{\pi}} \frac{Z_I Z_J}{\sqrt{R_I^{c2} + R_J^{c2}}} exp[-\frac{|\mathbf{R}_j - \mathbf{R}_I|^2}{\sqrt{R_I^{c2} + R_J^{c2}}}]\} \end{aligned} \tag{2.30}$$

$$\bigtriangledown_I E^{self} = 0. \tag{2.31}$$

All the other terms depend directly on the density matrix $P^{\mu\nu}$. One can define E^{core} and $H^{core}_{\mu\nu}$ as the energy and matrix elements from the electronic kinetic energy, the short range part of the local pseudopotential ($\mathrm{V}^{SR}_{loc}(\mathrm{r})$), and the non-local pseudopotential ($\mathrm{V}^{PP}_{nl}(\mathbf{r},\mathbf{r}')$)

to obtain the derivative of E^{core} (eq: 2.32).

$$\begin{aligned}
\nabla_I E^{core} &= \sum_{\mu\nu}(\nabla_I P^{\mu\nu})H^{core}_{\mu\nu} + \sum_{\mu\nu} P^{\mu\nu}(\nabla_I H^{core}_{\mu\nu}) \\
&= \sum_{\mu\nu}(\nabla_I P^{\mu\nu})H^{core}_{\mu\nu} \\
&+ \sum_{\mu\nu} P^{\mu\nu}[2\langle\nabla_I\varphi_\mu(\mathbf{r})|-\frac{1}{2}\nabla^2|\varphi_\nu(\mathbf{r})\rangle \\
&+ 2\langle\nabla_I\varphi_\mu(\mathbf{r})|V^{SR}_{loc}(r)|\varphi_\nu(\mathbf{r})\rangle \\
&+ 2\langle\nabla_I\varphi_\mu(\mathbf{r})|V^{PP}_{nl}(\mathbf{r},\mathbf{r}')|\varphi_\nu(\mathbf{r}')\rangle \\
&+ \langle\varphi_\mu(\mathbf{r})|\nabla_I V^{SR}_{loc}(r)|\varphi_\nu(\mathbf{r})\rangle \\
&+ \langle\varphi_\mu(\mathbf{r})|\nabla_I V^{PP}_{nl}(\mathbf{r},\mathbf{r}')|\varphi_\nu(\mathbf{r}')\rangle],
\end{aligned} \tag{2.32}$$

where the number of terms is already reduced by regrouping, exploiting symmetry of $P^{\mu\nu}$ and $H^{core}_{\mu\nu}$.

The density dependent energy terms are computed using the chain rule with the density as intermediate variable to yield the derivatives of $E^H[\rho_{tot}]$ and $E^{XC}[\rho]$.

$$\begin{aligned}
\nabla_I E^H[\rho_{tot}] + \nabla_I E^{XC}[\rho] &= \sum_{\mu\nu}(\nabla_I P^{\mu\nu})V^{tot}_{\mu\nu} \\
&+ 2\sum_{\mu\nu} P^{\mu\nu}\int(\nabla_I\varphi_\mu(\mathbf{r}))v^{tot}(\mathbf{r})\varphi_\nu(\mathbf{r}d\mathbf{r}) \\
&\int(\nabla_I\rho^I_c(\mathbf{r})v^H(\mathbf{r})d\mathbf{r}
\end{aligned} \tag{2.33}$$

where $v^{tot}(\mathbf{r}) = v^H(\mathbf{r}) + v^{XC}(\mathbf{r})$. In the eq: 2.33, the term involving $\nabla_I P^{\mu\nu}$ can be written by using the Kohn-Sham matrix $K_{\mu\nu}$ as

$$\sum_{\mu\nu}(\nabla_I P^{\mu\nu})(H^{core}_{\mu\nu} + V^{tot}_{\mu\nu}) = \sum_{\mu\nu}(\nabla_I P^{\mu\nu})K_{\mu\nu} \tag{2.34}$$

This can be simplified further as

$$\sum_{\mu\nu}(\nabla_I P^{\mu\nu})K_{\mu\nu} = -2\sum_{\mu\nu} W^{\mu\nu}\langle\nabla_I\varphi_\mu(\mathbf{r})|\varphi_\nu(\mathbf{r})\rangle \tag{2.35}$$

by using the energy weighted density matrix $\mathrm{W}^{\mu\nu}$.

As discussed earlier, electronic wavefunction must be optimized to its ground state at each molecular dynamic step for the Born-Oppenheimer trajectories after calculating the force. The calculation of the electronic ground state amounts to the minimization of the electronic energy with respect to the orthonormal one-particle orbitals or the one-particle density matrix. Two methods are currently available in QUICKSTEP module of CP2K to minimize the total ground state energy of a system by using an iterative self-consistent field (SCF) procedure: a traditional diagonalisation (TD) scheme and an efficient orbital transformation (OT) method. QUICKSTEP can deal with both (closed and open) types of systems using both the TD and OT method. OT method is very efficient and fast method to optimize the wave function in the presence of periodic electric field.

2.5 Treatment of Electric Field within DFT: Berry Phase Formalism

A pump pulse can be simulated by using a time-varying electric field, which is spatially homogeneous in the molecular dynamics. In the Born-Oppenheimer based AIMD, the spatially homogeneous time-varying electric field is treated explicitly within density functional theory (DFT) while solving the electronic structure for electrons periodic boundary conditions (PBC). For this, a non-local energy functional, which depends on the applied electric field is used within DFT, while calculating electrostatic contribution E^{ES}. This non-local energy functional gets multiplied with position operator to calculate the expectation value for contribution in electrostatic energy E^{ES}.

The non-periodic nature of position operator is the fundamental problem of treating periodic electric field within DFT. Even within the Schrödinger representation, if the position operator gets multiplied with the wave function while calculating the expectation value, it will not be periodic. When the periodic boundary condition is used, the multiplicative position operator is not a valid operator. This means that $x\psi(x)$ is not a periodic function, even if $\psi(x)$ is such periodic. The treatment of electric field within Schrödinger picture requires a special treatment with Berry Phase approach, while using PBC. The energy functional in DFT approach are also treated in a similar manner.

To understand this better, let's assume the case of single electron in one dimensional box of length L. If the PBC is not chosen, the wave function of electron $\psi(x)$ goes to zero exponentially outside a bounded region of space [88]. It is possible to use the operator $\hat{x} = x$, and define the position expectation value in the ground state $\psi_0(x)$ as usual:

$$\langle \hat{x} \rangle = \langle \psi_0 | \hat{x} | \psi_0 \rangle = \int x |\psi_0|^2 dx = \int x \rho(x) dx, \tag{2.36}$$

where $\rho(x)$ is the one-particle probability density which goes to zero outside the box. If we assume that the box is periodic in the X-direction with periodicity of length L, so the wave function is also periodic in nature $\psi_0(x + L) = \psi_0(x)$. Using the same definition of expectation value, the expectation value of position operator $\langle \hat{x} \rangle$can be written as

$$\langle \hat{x} \rangle = \int x |\psi(x + L)|^2 dx = \int x \rho(x + L) dx \tag{2.37}$$

In this case, the electron distribution may look like as in fig: 2.1. Expectation value of electron at boundary will go zero and will be maximum at centers which is only modulo of the replica periodicity. This expectation value is not correct as electrons can not have zero expectation value at boundary. The expectation value of this operator $\hat{x}$ cannot be calculated in this manner, if the wave function follows PBC. In fact, $\hat{x}$ does not commute with a translation by L, and therefore, it is not a legitimate operator in the Hilbert space.

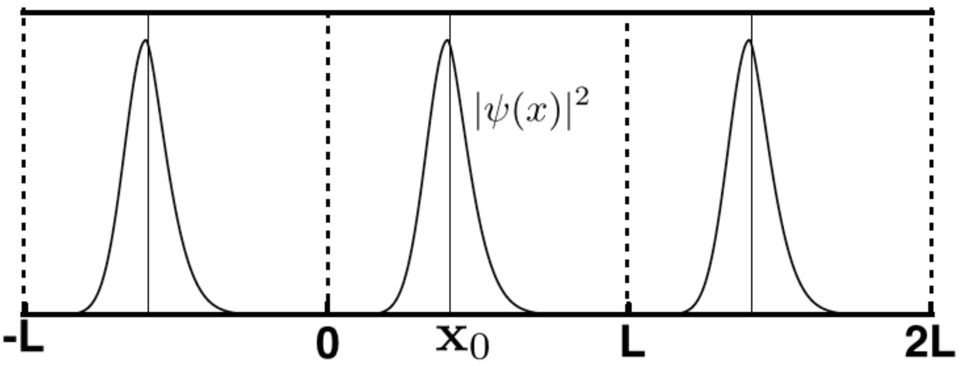

Figure 2.1: The distribution of $|\psi_x|^2$ of a single particle with PBC.

According to the Berry-phase formalism, a key quantity to deal with the position operator with PBC is the dimensionless quantity z defined as

$$z = \langle\psi_0|e^{i\frac{2\pi}{L}x}|\psi_0\rangle = \int_0^L e^{i\frac{2\pi}{L}x}|\psi(x)|^2 dx \tag{2.38}$$

A natural definition of a localized periodic distribution $|\psi_0|^2$ is therefore given by the phase of z as

$$\langle\hat{x}\rangle = \frac{L}{2\pi} Im \ln z = \frac{L}{2\pi} Im \ln\langle\psi_0|e^{i\frac{2\pi}{L}x}|\psi_0\rangle \tag{2.39}$$

While treating the electric field **E** (= E·x) on a system of electrons with PBC in DFT, same formalism was used on the energy functional applied on density (ρ), which was implemented explicitly for the calculation of electrostatic energy (E^{ES}). It is well known that polarization is also a manifestation of the Berry Phase. The polarization is an observable, which cannot be treated as the expectation value of any operator, being instead a gauge-invariant phase of any wavefunction. Such novel description of polarization has revitalized the study of electric fields in periodic electric structure calculation.

In CP2K, only time-independent electric field is implemented with periodic boundary condition. For the application of THz pulse, we incorporated the time-dependence of electric field by using a wrapper code along with CP2K. The wrapper code changes the value of periodic electric field at each time-step and then CP2K solves the SCF steps to find the ground state energy of the system in presence of this electric field.

2.6 Coherent X-ray Scattering

Exploring the structure of liquid water has been a matter of interest for many decades. Theoretically calculated radial distribution function g_{O-O} is connected to the tetrahedral structure of water. There have been many attempts to connect the g$_{O-O}$ to some experimental results. One of the experimental techniques which can measure g$_{O-O}$ is coherent x-ray scattering. Interestingly, Krack *et al.* developed a method including all-electron implementation of the Gaussian augmented plane wave method to calculate the coherent x-ray scattering signal [89] which can be obtained in experiments directly.

Within the first Born approximation, the elastic or coherent x-ray scattering intensities $I(q)$ for systems where no angular resolution exists are given by [89]

$$I(q) = \langle |F(\mathbf{q})|^2 \rangle, \tag{2.40}$$

where

$$F((q)) = \int \rho(\mathbf{r}) e^{i\mathbf{qr}} d\mathbf{r}, \tag{2.41}$$

is the Fourier transform of the one-electron density $\rho(\mathbf{r})$, $\mathbf{q}$ is the momentum transfer, and the average is over all $\mathbf{q}$ vectors with the same modulus q in the statistical ensemble. In order to extract $g_{OO}(r)$ experimentally, one usually assumes that the total charge density is a superposition of spherically averaged atomic charge densities (Debye approximation) whose Fourier transforms give the atomic form factors $f_i(q)$. The x-ray scattering intensities can then be written as

$$\begin{aligned} I(q) = & \sum_{ij} x_i x_j f_i(q) f_j(q) \frac{\sin q r_{ij}}{q r_{ij}} \\ & + \sum_{i \leq j} x_i x_j f_i(q) f_j(q) h_{ij}(q), \end{aligned} \tag{2.42}$$

where x_i is the ith species concentration and

$$h_{ij}(q) = 4\pi\rho \int_0^\infty (g_{ij}(r) - 1) \frac{\sin qr}{qr} r^2 dr, \tag{2.43}$$

The first term in eq: 2.42 represents the intramolecular scattering.

2.7 Force-Field Molecular Dynamics

The Hamiltonian of a system in presence of external potential (due to electric field) can be written as $H = H_0 + H_1$ [90, 91]. Here, H_0 is the internal part of the Hamiltonian, whereas H_1 is an external part which include the interaction with external potential. The internal Hamiltonian H$_0$ can be written as

$$H_0(\mathbf{R}^N, \mathbf{P}^N) = \sum_{I=1}^{N} \frac{1}{2} M_I \ddot{\mathbf{R}}_I^2 + U(\mathbf{R}^N) \tag{2.44}$$

where $U(\mathbf{R}^N)$ is the potential energy due to particle-particle interaction. The atoms are here described as point-like centers which interact through pair or multibody interaction potentials. In contrast to AIMD (as discussed above in detail), the highly complex description of electronic structure is abandoned. But, an effective and simplified picture is adopted, where the potential energy surface of the system is modelled by a set of parameters and analytical functions. The combination of these parameters and functions is known as the *"Force field"*. The force acting on each particle can be derived for use in *Newton's equation of motion (EOM)*(eq: 2.45).

$$\mathbf{F}_I = M_I \ddot{R}_I = -\nabla U(\mathbf{R}^N) \tag{2.45}$$

There have been many types of force-field developed in past which include MM3, MM4, Dreiding, SHARP, VALBON, UFF, CFF95, AMBER, CHARMM, OPLS and MMFF. The major difference among all force-fields is the distinction between pair- and multi-body potentials, and also to the spatial extent of a potential, classified as short and long range interactions.

2.7.1 Short Range Interaction

As short range interaction, one understands interactions that can be described with an effective potential that decays r^{-d} where r is the distance between two particles and d is the dimension of the problem. In such interactions, one considers only particles up to a certain distance for the calculation of interaction. There are two kind of short range forces. 1) intramolecular forces and 2) intermolecular forces.

Intramolecular interactions are the forces defined among the atoms within a molecule which are bonds, angles, dihedrals and impropers. In the OPLS force field, an intramolecular bond is modelled via harmonic bond stretching potential.

$$U_{bond}(r) = \sum_{bond} \frac{1}{2} K_{bond}(r - r_{eq}) \tag{2.46}$$

where K is the harmonic bond constant and r_{eq} is the equilibrium bond distance. In some cases, the Morse bond stretching potential is also used(eq: 2.47).

$$U_{bond}(r) = \sum_{bond} D[1 - \exp(-\alpha(r - r_{eq}))]^2 \tag{2.47}$$

where r_0 is the equilibrium bond distance, α is a stiffness parameter, and D determines the depth of the potential well. The bond bending is defined by the harmonic potential.

$$U_{angle}(\theta) = \sum_{angle} \frac{1}{2} K_{angle}(\theta - \theta_{eq})^2 \tag{2.48}$$

where θ_{eq} is the equilibrium value of the angle, and K is the harmonic angle constant. For the OPLS force-field, dihedrals interaction is computed by

$$U_{dihedrals}(\phi) = \sum_{dihedrals} (\frac{1}{2}K_1[1+\cos(\phi-\phi_{eq})] + \frac{1}{2}K_2[1-\cos 2(\phi-\phi_{eq}))]+ \tag{2.49}$$

$$\frac{1}{2}K_3[1+\cos 3(\phi-\phi_{eq})] + \frac{1}{2}K_4[1-\cos 4(\phi-\phi_{eq})] \tag{2.50}$$

where $\phi's$ are dihedral angle and $K's$ are dihedral constants.

Besides all these intramolecular potentials, the short-range intermolecular interaction is described by the Lennard-Jones potential. This non-bonded short range interaction includes Vander-Walls interaction. The lennard-jones potential is given by

$$U_{LJ}^{\alpha\beta}(r_{ij}) = \sum_{i=1}^{N}\sum_{i>j}^{N} 4\epsilon[(\frac{\sigma_{\alpha\beta}}{r_{ij}})^{12} - (\frac{\sigma_{\alpha\beta}}{r_{ij}})^{6}] \tag{2.51}$$

where ϵ is the minimum potential energy located at $r = 2^{1/6}\sigma$ and σ is the diameter of the particle, since for $r < \sigma$, the potential becomes repulsive. The indices α, β indicate the particle type. Arithmetic mixing of Lennard-jones potential for two different atoms follows the Lorents-Berelot combining rules for its parameters.

$$\sigma_{\alpha\beta} = \frac{\sigma_{\alpha\alpha} + \sigma_{\beta\beta}}{2}, \epsilon_{\alpha\beta} = \sqrt{\epsilon_{\alpha\alpha}\epsilon_{\beta\beta}} \tag{2.52}$$

2.7.2 Long Range Interactions

For the long range interaction, interaction between all N interacting particles in the system must be taken into account which is a $O(N^2)$ problem. In general, long range forces are Coulombic interaction for the collection of atoms with partial effective charge q_i.

$$U_{coul}(r_{i,j}) = \sum_{i=1}^{N}\sum_{j>i}^{N} \frac{q_i q_j}{r} \tag{2.53}$$

where q_i and q_j are the charges of the 2 atoms in atomic unit. For the sake of computational efficiency, $U_{coul}(r_{i,j})$ is evaluated as a truncated sum over neighbors within a defined cut-off r_c, rather than as a full $O(N^2)$ double sum problem.

When periodic boundary conditions are applied, one has to take into account not only the interaction among the particles in the central cell, but also with all periodic images. There are many computational methods to calculate the coulombic interaction for systems under periodic boundary condition, e.g., Ewald sum method, fast multipole (FMM) method and particle-particle-particle-mesh methods (PPPM). PPPM method is the fastest implementation among others for parallel simulations which was also used in our simulations. In PPPM [92], one replaces the point-charge Coulombic term with an equivalent expression for extended charge centered on the atomic positions, namely

$$U_{coul}(r_{i,j}) = \sum_{i=1}^{N}\sum_{j>i}^{N}\frac{q_i q_j}{r_{ij}} erfc(Gr_{ij}/\sqrt{2}) + \frac{1}{2}\int\int\frac{\hat{\rho}(r)\hat{\rho}(r')}{|r-r'|}drdr' - \frac{G}{\sqrt{2\pi}}\sum_{i=1}^{N} q_i^2 \tag{2.54}$$

where $\hat{\rho}_i(r) = q_i(Gr_{ij}/\pi)^{3/2}exp[-G^2(r-r_i)^2]$ is the Gaussian density that represents an extended charge and $\hat{\rho}(r) = \sum_i \hat{\rho}_i(r)$. In eq: 2.54, the first term is the usual Coulombic interaction multiplied by an error function, that forces it to go (≈) to zero at specified cutoff distance r_c. This term is the near-field portion of the Coulombic energy, which is calculated along with other forces as a sum over nearby pairwise interactions using a neighbor list. The second term is the Coulombic energy due to interaction of extended charges.

2.8 Molecular Dynamics

The force and energy of a system at a particular time can be obtained by using either the DFT method or force field parameters as discussed above. For a given potential model that characterizes the system, the system propagates with time by solving the Newton's equation of motion. We used velocity-verlet integrator to obtain positions and velocity in next step under the given ensemble.

2.8.1 Molecular Dynamics Simulations in Different Ensembles

In molecular dynamics, it is feasible to realize different types of thermodynamic ensembles which are characterized by the control of certain thermodynamic quantities like temperature, pressure or energy.

The Microcanonical Ensemble

The microcanonical ensemble (NVE) can be considered as the natural ensemble for molecular dynamics simulations. In the microcanonical ensemble, the number of particles (N), the volume (V) and total energy of the system (E) remains constant. If there are no time dependent external forces on the system, the Hamiltonian remains constant which implies that the system's dynamics evolves on a constant energy surface. The corresponding probability density in phase space is therefore given by

$$\rho(\mathbf{q},\mathbf{p}) = \delta(H(\mathbf{q},\mathbf{p}) - E) \tag{2.55}$$

where in principle, all the accessible states are equally probable. In the microcanonical ensemble (NVE), the number of microstates is given by

$$\Omega(N,V,E) \propto \int d\mathbf{r}_1 ... \int d\mathbf{r}_N \int d\mathbf{p}_1 ... \int \mathbf{p}_N \delta(H(\mathbf{r}^N,\mathbf{p}^N) - E) \tag{2.56}$$

The Canonical Ensemble

In the canonical ensemble (NVT), the number of particles (N), the volume (V) and the temperature are fixed at a defined value. The temperature (T) is an intensive quantity that can be measured by an extensive quantity, known as energy. In the canonical ensemble, the system is in equilibrium with a thermal bath of fixed temperature (T). The probability of the macrostate at a given T is given by the Laplace transform of the density of states at energy (E)

$$Q(N,V,T) = \int \exp(-\beta E)\Omega(N,V,E)dE \tag{2.57}$$

$$Q(N,V,T) = \frac{1}{N!h^{3N}} \int \exp[-\beta \mathbf{H}(\mathbf{r}^N,\mathbf{p}^N)]d\mathbf{r}^N d\mathbf{p}^N \tag{2.58}$$

where $\beta = \frac{1}{k_B T}$.

To fix the temperature during the NVT MD simulation, one uses an efficient thermostat which provides a bath like environment to maintain the temperature. Here, we have used Nosë-Hoover thermostat which is an integral thermostat which is explained in detail in the following section..

2.8.2 Nosë-Hoover Thermostat

The Nosë-Hoover thermostat introduces an extra degree of freedom in system's Hamiltonian to represent the heat bath, from which the equations of motion can be derived. Hence, it is also known as extended system method or integral thermostat [93, 94]. The main concept of this thermostat is to reduce the effect of an external system acting as heat reservoir to keep the temperature of the system constant. So, the thermal interactions between a heat reservoir and the system changes the kinetic energy of the systems, i.e. the velocity of the particles in the system.

Assume the simulated system consists of N particles, with coordinates $\mathbf{q'}_i$, masses m_i, potential energy $\phi(\mathbf{q'})$, and momenta $\mathbf{p'}_i$. An extra degree of freedom s is also introduced acting as an external degree of freedom on the the simulated system. New virtual variables (coordinates $\mathbf{q}_i$, momenta $\mathbf{p}_i$, and time t) are also introduced which are related to real variables $(\mathbf{q}', \mathbf{p}', t')$ as

$$\mathbf{q}'_i = \mathbf{q}_i, \mathbf{p}'_i = \mathbf{p}_i/s, t' = \int_0^t \frac{dt}{s} \tag{2.59}$$

$$\frac{d\mathbf{q}'_i}{dt'} = s\frac{d\mathbf{q}_i}{dt} \tag{2.60}$$

Using these variables, the Hamiltonian of the extended system can be written as

$$H_{Nose} = \sum_{i=1}^{N} \frac{\mathbf{p}_i^2}{2m_i s^2} + \phi(\mathbf{q}) + \frac{p_s^2}{2Q} + 2gk_B T \ln s \tag{2.61}$$

where Q is an effective mass associated to s and the parameter g is equal to the number of degrees of freedom of the system. Using the extended Hamiltonian, the equation of motion can written as

$$\frac{d\mathbf{q}_i}{dt} = \frac{\partial H_{Nose}}{\partial \mathbf{p}_i} = \frac{\mathbf{p}_i}{m_i s^2} \tag{2.62}$$

$$\frac{d\mathbf{p}_i}{dt} = -\frac{\partial H_{Nose}}{\partial \mathbf{q}_i} = \frac{\partial \phi}{\partial \mathbf{q}_i} \tag{2.63}$$

$$\frac{ds}{dt} = \frac{\partial H_{Nose}}{\partial p_s} = \frac{p_s}{Q} \tag{2.64}$$

$$\frac{dp_s}{dt} = -\frac{\partial H_{Nose}}{\partial s} = \frac{\sum \frac{\mathbf{p}_i^2}{m_i s^2} - gkT}{s} \tag{2.65}$$

This method produces microcanonical ensemble for extended system due to the conservation of extended Hamiltonian H_{Nose} with the evolution of equations of motion and has been used in the equilibriation dynamics of both AIMD and FFMD simulations presented in the following chapters.

2.9 Summary

In this chapter, I shortly summarized the methods to calculate the force and energy of the system at a particular timestep in AIMD and FFMD. For the time-evolution of the system, both methods solve Newton's equation of motion and use velocity-verlet integrator for the expansion of position and velocity. During the thermalization of the system at a temperature, the Noӛe-Hoover thermostat was used under canonical ensemble in both cases. The MD trajectories were propagated under microcanonical ensemble in presence of the electric field. AIMD calculates the force and energy at each time-step by treating nuclei classically and electrons quantum mechanically by DFT. Whereas FFMD uses a parameterized force-field for the calculation of energy and force at each step. During AIMD, time-dependence of electric field was applied with an external code, which changed the value of periodic electric field at each step to solve the SCF steps for evaluating the ground state energy via CP2K.

Chapter 3

Ultrafast Energy Transfer to Liquid Water by Sub-picosecond THz Pulse

3.1 Introduction

Liquid water is known as the "matrix of life" [95]. It features numerous anomalous behaviour [96] in different conditions like temperature, pressure, electric field and confinements etc, which lead the researchers to explore it computationally and experimentally during the last decades. Liquid water does not provide an inert and passive environment to the solute [95] in chemical or biological processes. Rather, the dramatic changes in its physical and chemical properties with temperature and pressure, influences the dynamics of water around solute molecules which make water an active solvent [97]. These properties of water play a key role in solvation and stabilization of reaction intermediates. The strong hydrogen bond among molecules is one of the fundamental reasons for all these ubiquitous properties of water. This is reason why water is the single most important medium in which chemical and biological processes take place.

In recent years, the pump-probe spectroscopic studies on liquid water in a broad range of frequencies are exemplifying the growing interest to understand the interaction of water with lasers and its basic features. Examples include Raman and infra-red spectroscopy [98], femtosecond nonlinear spectroscopy [99], inelastic neutron scattering [99], fluorescence spectroscopy [100], pump-probe experiments [101] and other techniques [68, 102]. Intermolecular vibrational modes lie in the frequency domain of 1 to 10 THz ($\approx$ 30-300 cm^{-1}) [103, 104]. Intermolecular modes correspond to the vibrations of the hydrogen bonded network, which includes two or more water molecules. THz radiation affects the collective motions of water, which are low frequency intermolecular vibrations [102]. This feature makes of THz radiation a convenient frequency range to investigate the hydration dynamics around solutes [105]. There have been many experimental and theoretical studies of laser spectroscopy in THz frequency domain on water dynamics with low intensity for small solutes like carbohydrates and proteins [102, 106]. The THz absorption spectroscopy has shown the effect from small to large hydration shell (≈7-20 Å), which results many processes in water like hydrogen bond rearrangement and excitation of librational modes in ps timescale. This makes of THz radiation, a key technique for studying bulk systems such as enzymatic reactions and protein folding.

The advent of highly intense and ultrashort light sources has turned the dream of pump-probe experiments with femtosecond resolution and high brilliance [107] into reality. Intense EM radiations can be generated in synchronization with free electron lasers (FELs) and has opened the door to investigate the time resolved ultrafast processes of the inter and intra-molecular modes of liquids and solids. FELs operating in the THz domain have been available for sometime now. Recently, the generation of THz radiation from X-ray FELs (XFELs) in full synchronization with the X-ray pulse has been demonstrated [72, 108]. As one of the finest examples of the use of XFEL, time-resolved X-ray spectroscopy was used to film the spin-flip dynamics of iron metal complexes by electronic excitation with a fs pulse at LCLS [109].

Such sources provide an interesting platform for pump-probe experiments, where THz can excite the inter-molecular modes and interrogate the system at well defined time-delays by an ultrashort X-ray pulse. The combination of X-ray probe with THz pump scheme has already been used in pump-probe experiments in material science specifically in light induced superconductivity applications [110]. Liquid water has also been studied in ultrafast infrared spectroscopy and nonlinear vibrational spectroscopy [40, 111], where infrared pulse excites the OH stretching and bending and follow the dynamics with a fs X-ray probe pulse. In the IR domain, the intense pulse excites the intra-molecular vibrations and follows the energy dissipation processes. It has also been shown that THz light couples to low energy collective modes of the liquid at low intensity [68, 102]. But all these studies have been performed with low intensity laser sources, where mostly one photon absorption processes dominates. However, there is not much known about the sub-picosecond response of liquid water to intense and ultrashort (one cycle) THz pulse, which is mostly due to lack of high intensity THz sources with pulse duration in the fs regime.

In this chapter, I will describe an *ab-initio* molecular dynamics (AIMD) study of the response of liquid water to a highly intense and sub-picosecond THz pulse. The large amount of energy per water monomer transferred to the liquid, changes its structure by disrupting the H-bond network and tetrahedral coordination of water molecules in a very short time. This structural modification were analyzed by computing time-resolved coherent X-ray scattering and radial distribution function. The large energy gain in water changes the inter- and intra-molecular vibrations, which correspond to higher temperature. The changes in internal vibrations were analyzed by calculating the power-spectra at different time-delays.

3.2 Method

Molecular Dynamics (MD) simulations have been vastly performed to investigate the energy relaxation and redistribution. Here, Ab Initio Molecular Dynamics (AIMD) simulations were performed by using "CP2K molecular dynamics package" [112]. The AIMD Born-Oppenheimer trajectories have been propagated via Quickstep electronic structure module, which was described in chapter:2 in detail. Gaussian and plane waves (GPW) [83] method of Quickstep module [79] was used to to study the electronic structure during geometry optimization (GO) and MD. The Perdew-Burke-Ernzerhof (PBE) functional was used together with Geodecker-Teter-Hutter (GTH) pseudopotential [86] to define the electronic density. We used plane waves upto 400 Ry and the TZV2P [79] basis set to expand the density and orbitals respectively. All the simulations were carried out under periodic boundary conditions in all three spatial directions and one fs timestep was used in all simulations.

A cubic box containing 256 water molecules at a density of 1 g/cm^3 was equilibriated thermally at room temperature (300 K) using canonical (NVT) MD with Nöse-Hoover thermostat. Thermally equilibriated configuration was propagated for 5ps long time to collect 15 initial configurations (positions and velocities) at a certain time internal. Each initial configuration was propagated microcanonically (NVE) for 1.5 ps long time in the presence of the THz pulse. During NVE-MD, the AIMD Born-Oppenheimer trajectories were propagated with explicit inclusion of electric field in Quickstep. Such THz pulse is given by

$$\mathbf{E}(t) = \epsilon(t)\mathbf{u}_z \cos(\omega_c t + \phi), \tag{3.1}$$

where $\epsilon(t) = A \exp\{-(t - t_0)^2/2\sigma^2\}$ is a Gaussian envelope with $\sigma = 84.93$ fs. This corresponds to a full width at half maximum (fwhm) of $\epsilon^2(t)$ of 141 fs. The maximum electric field amplitude A=0.61 V/Å corresponds to a peak power per unit area of 5×10^{12} W/cm^2. We consider a mean frequency $\omega_c = 2\pi \times 3$ THz (100 cm^{-1}), which is a full and half cycle long pulse. $\mathbf{u_z}$ is the polarization direction of the electric field and ϕ is the carrier-envelope phase (CEP), which we set equal to $\pi/2$. In all reported results, the THz pulse envelope is centered at $t_0 = 0$ fs and trajectories are started at $t = -250$ fs, when the Gaussian envelope of the pulse is still negligible. THz pulses of these characteristics were generated recently by optical rectification of mid-infrared laser pulses in an organic nonlinear crystal [113]. We also tried other CEPs and obtained very similar results. During NVE MD, thermostat was switched off.

Time resolved coherent x-ray scattering (TR-XRD) patterns [89] of the system were obtained by Fourier transform of the electron density of snapshots during the dynamics. We averaged over the 15 available trajectories at every time delay between THz and x-ray probe pulse and convolved the set of patterns with a 20 fs Gaussian window to represent the finite length of the probing X-ray pulse. The Gaussian and augmented plane waves (GAPW) method [114] of Quickstep was used instead of GPW for the calculation of the TR-XRD patterns [89]. GAPW is an all electron method [114], which is crucial to describe the electron density near the nuclei. The time resolved spectral densities at different pump-probe time delays were calculated to analyze the changes in frequency of internal vibrational modes due to THz pump. It was calculated by the Fourier transform of velocity-velocity auto-correlation function.

Energy Partitions

The analysis on the energy gain by the bulk water is performed on the basis of decomposing the total kinetic energy (KE) of each rigid water monomer m in its rotational energy (RE), translational energy (RE) and vibrational energy (VE) components. This is simply achieved in Cartesian coordinates by,

$$TE = \frac{|\sum_{a_m} M_{a_m} \vec{V}_{a_m}|^2}{2\sum_{a_m} M_{a_m}} \tag{3.2}$$

and

$$\begin{aligned} RE &= \sum_{a_m} \frac{\vec{j}^2_{a_m}}{2M_{a_m}|\vec{x}_{a_m}|^2} \\ \vec{j}_{a_m} &= M_{a_m}\,(\vec{x}_{a_m} \times \vec{v}_{a_m}), \end{aligned} \tag{3.3}$$

where $\vec{x}_{a_m} \equiv \vec{X}_{a_m} - \vec{X}_m$ and $\vec{v}_{a_m} \equiv \vec{V}_{a_m} - \vec{V}_m$ define the position and velocity of atom a in monomer m relative to the center of mass position $\vec{X}_m$ and velocity $\vec{V}_m$ of the monomer, respectively. In general, at this point the kinetic energy per monomer related to vibrational motion of the remaining $3N-6$ intramolecular coordinates $VE = KE - TE - RE$ can be obtained. The temperature (T) of water system presented here is the kinetic temperature (T_K), which is computed by using equipartition theorem.

$$E = \frac{n}{2} k_B T_K \tag{3.4}$$

where n is the number of degrees of freedom involved in the calculation of energy (E). E can be KE, TE, RE or VE. k_B is the Boltzmann constant.

3.3 Results

3.3.1 Energy Transfer by THz Pump to Liquid Water

In order to understand the energy transfer dynamics from the THz pulse to liquid water, we partitioned the total kinetic energy (KE) of the water monomer into 3 different distributions:

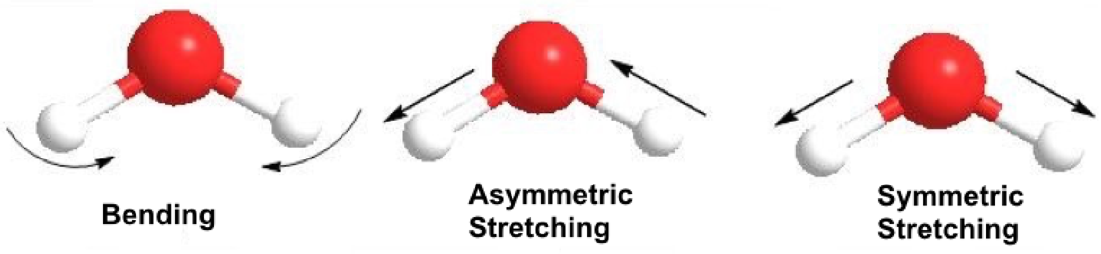

Figure 3.1: Intramolecular vibrations of an isolated water molecule

1) Translational (TE) : Translation motion of the center of mass of each molecule

2) Rotational (RE) : Rotation of the molecule around its instantaneous principal axes of rotations

3) Vibrational (VE) : Internal vibrations of a molecule

VE includes intra-molecular bending and stretching motions (fig: 3.1) which were not been separated here. In the bulk, TE and RE contributions arise from hindered rotations and librational motions of the water monomer. Figure: 3.2 shows the mean value of the total KE per water monomer as a function of time, as well as the TE, RE and VE contributions. At time t=-250 fs, KE is equipartitioned among all the degrees of freedom. All three energy distributions follow a Maxwell-Boltzmann distribution at T=300 K. The probability distribution of TE, RE and VE has been presented together with Maxwell-Boltzmann distribution at 300 K and 330 K in fig: 3.3(a). During the pulse, the KE per water monomer increases most rapidly as the pulse reaches the peak electric field amplitude of 0.5 to 0.6 V/Å which is present only during few tens of fs. The significant increment in KE starts only after the pulse reaches about half of its maximum amplitude (≈ 0.25-0.3 V/Å) and keeps on increasing until it reduces to less than half of its peak value. As expected, the KE remains constant after the pulse, only slightly fluctuating due to the exchange of total KE and potential energy. The total energy of each trajectory after the THz pulse is conserved to numerical accuracy as expected from a microcanonical simulation. The KE increase per monomer of about ≈ 2300 cm^{-1} (0.3 eV or 6.6 kcal/mol) corresponds to a final kinetic temperature of ∼1050K. This energy gain corresponds to an absorption of about 25 THz photons per water monomer. The increase in VE is slower than TE and RE. The reason is that the THz pulse interacts mainly with the permanent dipole moments of the water monomers, forcing them to rotate out of their preferred arrangement. In the bulk, molecular rotations are hindered and quickly lead to collisions. This sets in motion hindered molecular translations. The resulting collisions quickly bring energy to internal modes on a short time scale. We assume that the heating process is isochoric on a picosecond time scale for a bulk system, meaning on such short time scales no increase in volume is expected to take place. This assumption will be discussed in detail in chapter 6. All KE contributions, namely TE, RE and VE, reach a quasi-equilibrium distribution

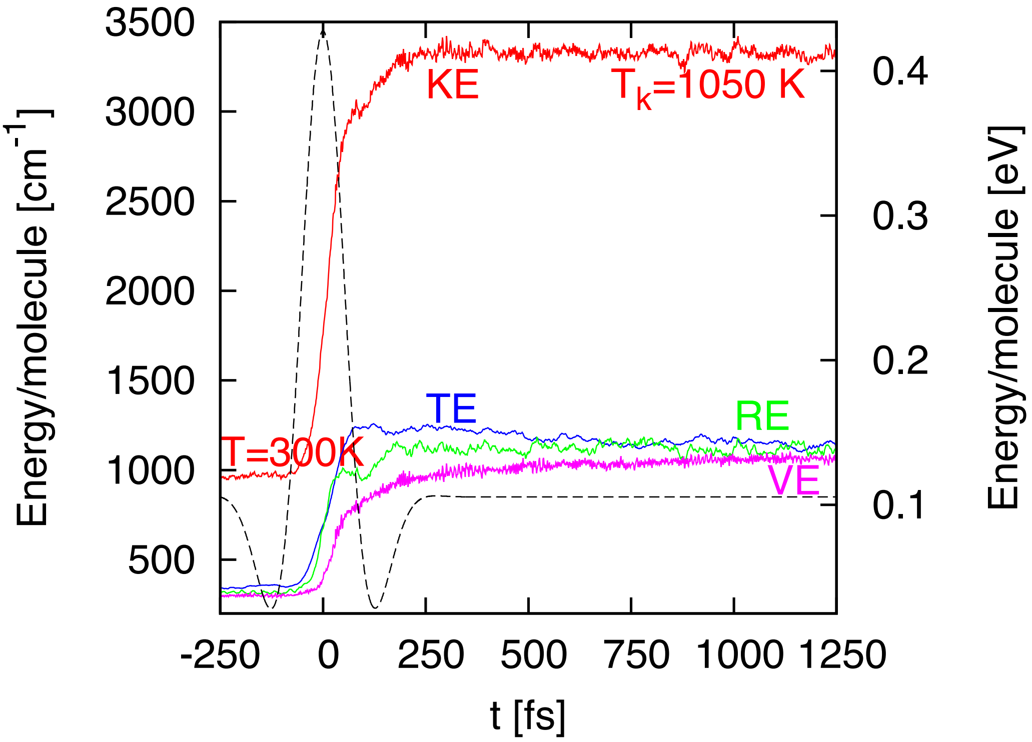

Figure 3.2: Kinetic energy partitioning per water monomer as a function of time. $t = 0$ corresponds to the center of the THz pulse envelope. Red: total kinetic energy (KE), blue: translational energy (TE), green: rotational energy (RE), pink: vibrational energy (VE), dashed: electric field amplitude. The maximum of the electric field amplitude is 0.61 V/Å. For water $\langle KE \rangle = \frac{9}{2} k_B \mathrm{T}_k$, where T_k is just a kinetic temperature and no assumption of thermal equilibriation is made whatsoever. $\langle KE \rangle$ is the ensemble-averaged kinetic energy per water molecule from all trajectories and all water molecules.

within 1 ps after the pulse.

Figures: 3.3(b), 3.3(c) and 3.3(d) show the probability density (or molecular distribution) with energy for TE (dP_{tra}), RE (dP_{rot}) and VE (dP_{vib}) at different times. At t=-250fs, all the probability density take the form of the equilibrium Boltzmann distribution at T=300 K. The molecular distributions for TE, RE and VE have not changed substantially till t = -50 fs. As the pulse profile crosses its peak field amplitude at t = 0 fs, the molecular distribution changes suddenly shifting to higher energy. The probability densities at times after the pulse are similar to the Maxwell-Boltzmann distribution at higher temperature. Probability density for VE after the pump is similar to Maxwell-Boltzmann distribution at high in temperature.

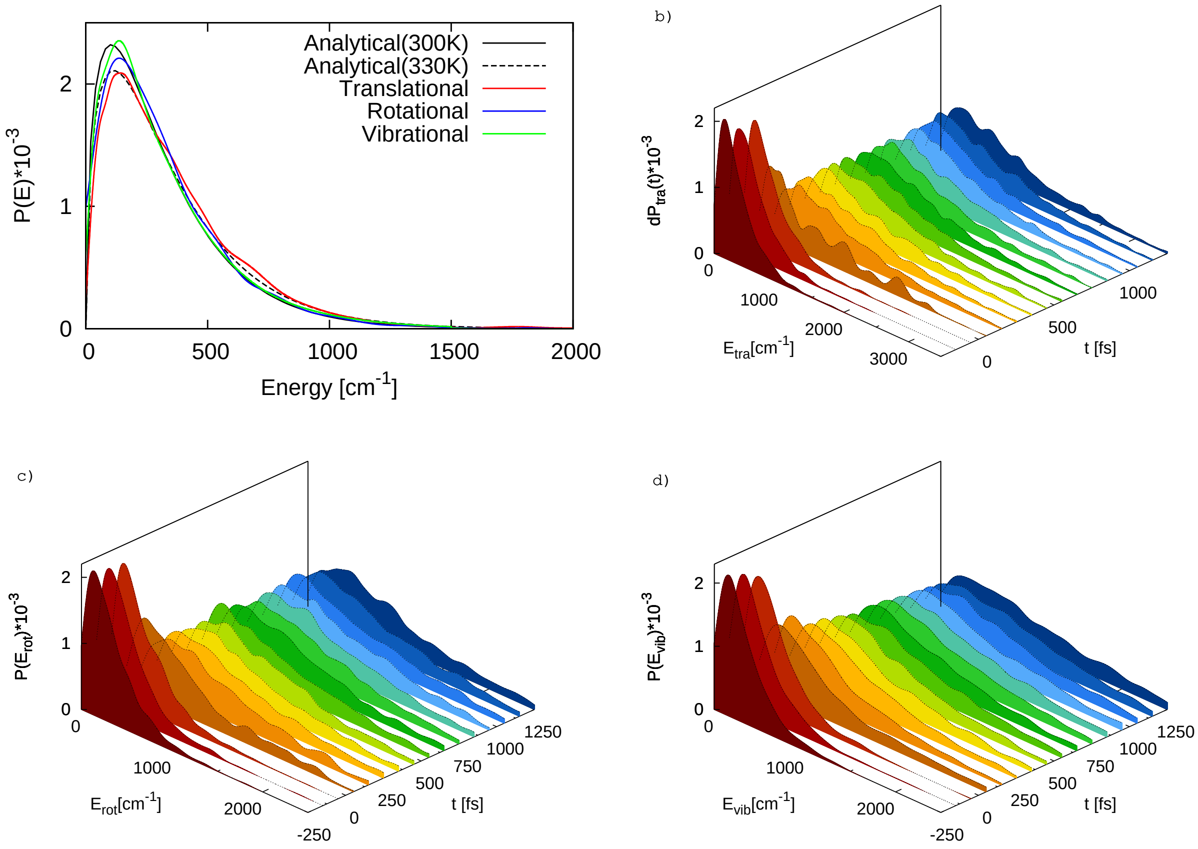

Figure 3.3: (a) Kinetic energy distribution per water molecule in its translational (red), rotational (blue) and vibrational (green) degrees of freedom compared analytical Maxwell-Boltzmann distributions at T=300 K and T=330 K. Probability density (Molecular distribution) with energy and time (b) Translational Energy (c) Rotational Energy and (d) Vibrational Energy. Here, all the distributions are normalized such that $\int_0^\infty P(E)dE = 1$.

3.3.2 Structural Changes in Liquid Water by THz Pulse

Time-resolved Coherent X-Ray Scattering

The THz pulse transfers large amount of energy to liquid water, which also causes big structural changes. A convenient probe of the structural transformations of a material is the coherent X-ray scattering (XRD) signal, which is computed with the Fourier transform of the electron density. XRD pattern has been studied theoretically and experimentally by many researchers for bulk water for a broad range of temperatures and pressures [115, 116]. XRD pattern of liquid water is characterized by a double peak at T=300K [89]. The peak at ~ 2 Å^{-1} is related to typical oxygen-oxygen distances in tetrahedrically coordinated

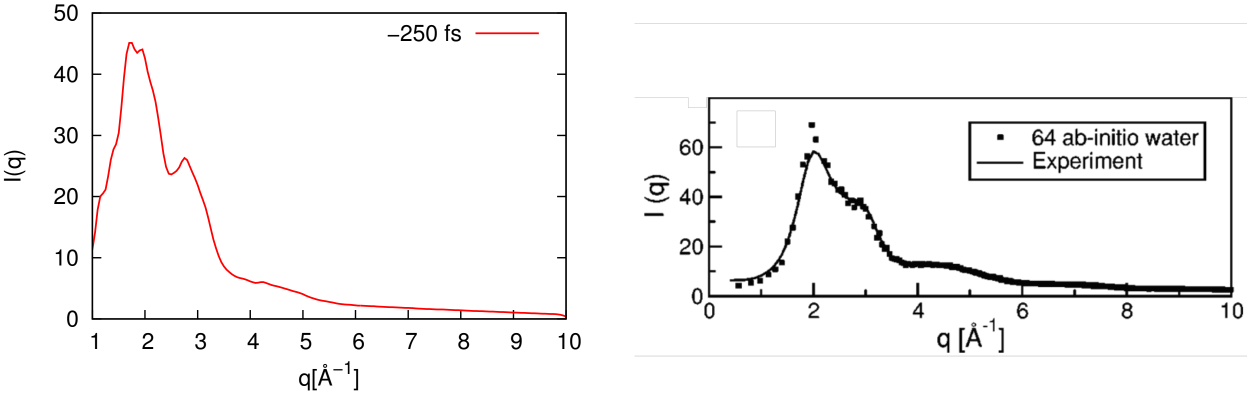

(a) (b)

Figure 3.4: (a) Coherent x-ray scattering signal of water computed at time t = -250 fs when there is no pulse. This is compared with (b) coherent x-ray scattering signal presented in ref: [89] for water at 300 K and 1 g/cm^3.

water, whereas the lower peak at ∼ 3 Å^{-1} is related to features of the density connected to the hydrogen-bond structure. XRD pattern at t=-250 fs in fig: 3.4 is clearly showing the double peak behaviour at T=300K. The TR-XRD(fig: 3.5) shifts into a pattern with a single peak at about 2.2 Å^{-1} after the pump pulse at 0 fs. This is a strong indication of

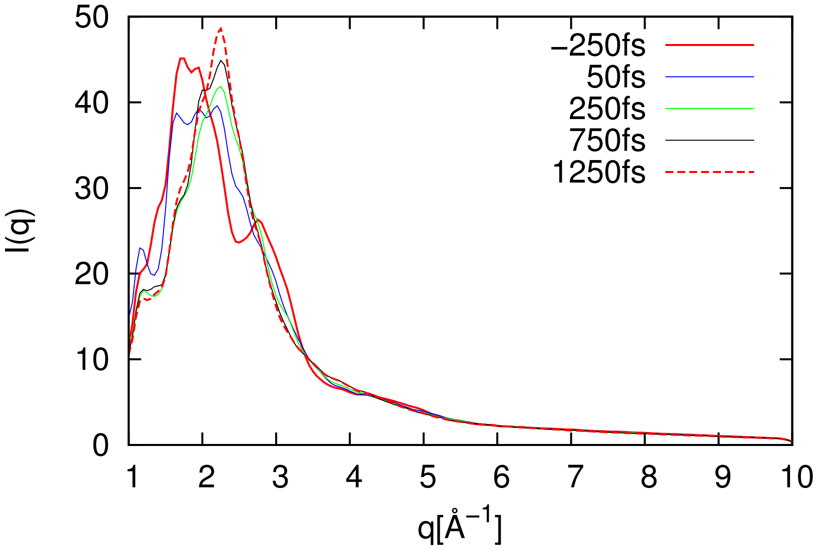

Figure 3.5: Coherent x-ray scattering signals of water at different times during and after the pump pulse.

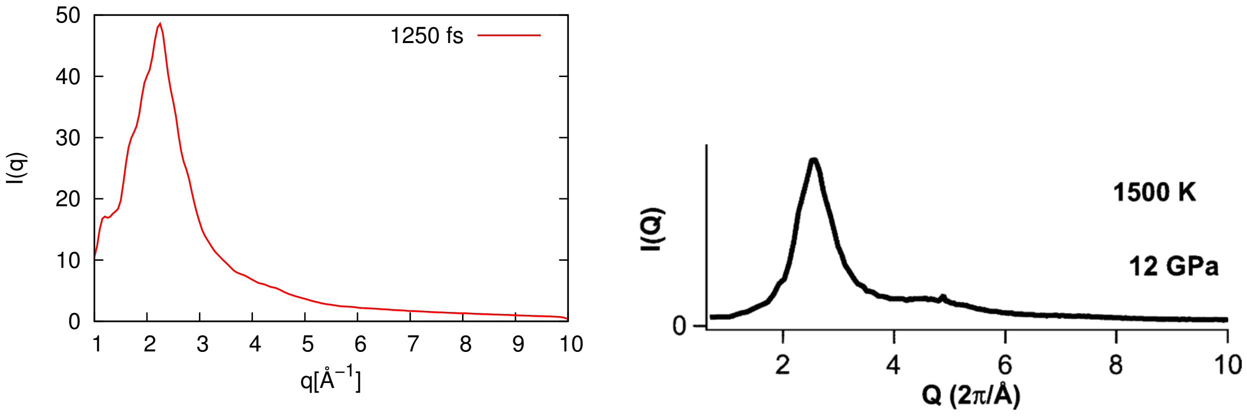

(a) (b)

Figure 3.6: (a) Coherent X-ray scattering of water computed at time t = 1250 fs after the pump pulse and the result is compared with (b) x-ray scattering of water at 1500 K and 12 GPa as shown in ref: [115].

dramatic changes of the tetrahedral structure of water molecules in the liquid. This is also a signature which signifies the disruption of the hydrogen bond network of water. The TR-XRD pattern obtained after the pulse is similar to the XRD pattern of water at extreme conditions. XRD pattern at t = 1250 fs (fig: 3.6)shows the one peak behaviour found for temperatures of 1500 K and pressures of 12 GPa [115], where a complete disruption of the shell structure of liquid water has been reported. This indicates that extreme conditions similar to a very high temperature and pressure have been achieved within a sub-ps time scale.

Radial Distribution Functions

Fig. 3.7(a) showed the radial distribution function (RDF) i.e. g_{O-O}(r) which were calculated as a function of time. g_{O-O}(r) makes transition from two peaks structure to flat type RDF due to the pump. Two peak structure of g_{O-O}(r) for water corresponds indicative of the first two solvation shells around each, whereas flat RDF (g_{O-O}(r)) is typical of a gas. This change occurs suddenly after the peak of THz pulse at t=0 fs. Similar structural transformations was observed by TR-XRD. Similarly, the g_{O-H}(r) RDF and Fig. 3.7(b) shows a very fast disruption of the hydrogen bond network, clearly seen by the disappearance of the peak at ∼2 Å which is related to the oxygen-hydrogen distance in a hydrogen bond. g_{O-H}(r) corresponding to intramolecular O-H distance was not shown here. We remind that the structural changes occur isocorically since there is no time for the bulk to change its volume in the ps time scale of the excitation.

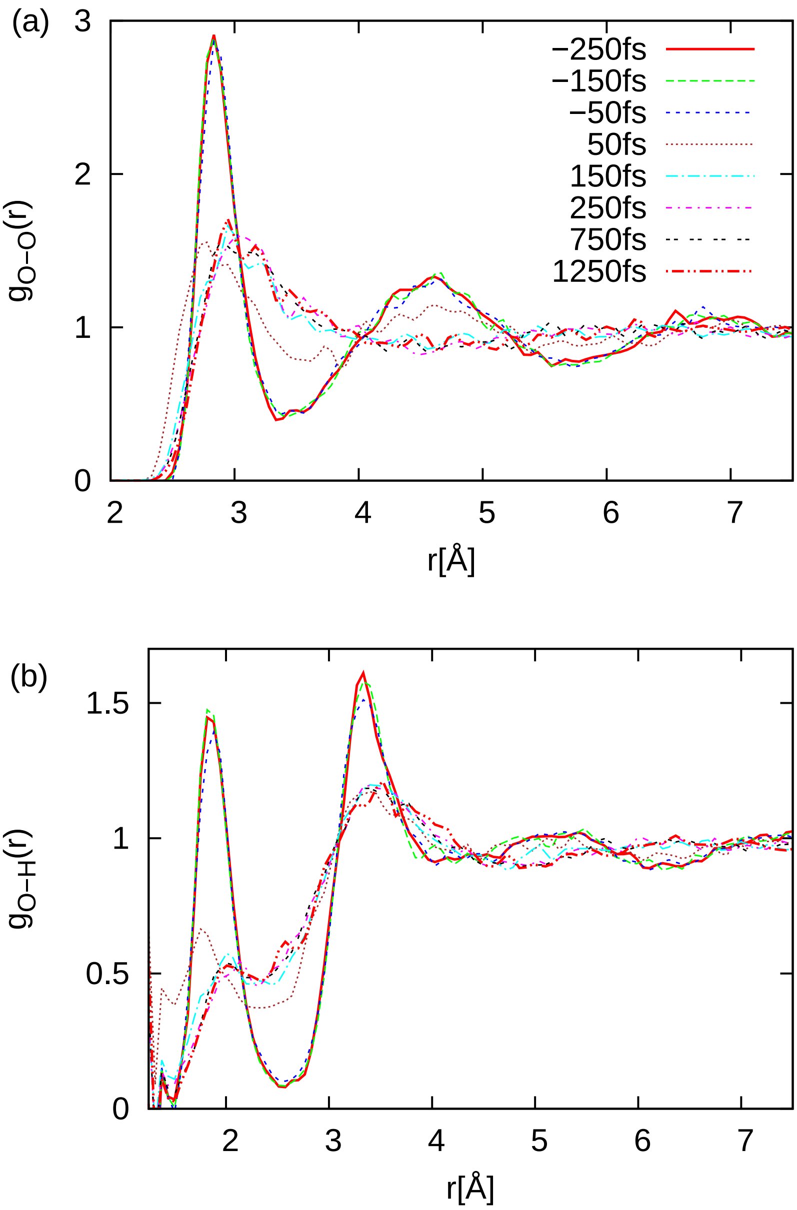

Figure 3.7: (a) Radial distribution functions (a) $g_{O-O}(r)$ and (b) $g_{O-H}(r)$ at different time delays under the effect of THz pulse.

3.3.3 Vibrational Transformations in Liquid Water by THz Pump: Time-delay Power Spectrum

Raman [117], infrared [101, 118, 119] and neutron scattering [117] spectra of liquid water show existing intra-molecular stretching and bending vibrations between 400-4000 cm^{-1}. Librational motion of water shows a band between 400-1200 cm^{-1} with maximum at ~670 cm^{-1}, the intramolecular OH bending band between 1200-2200 cm^{-1} with peak at ∼1650 cm^{-1} and OH stretching band between 2900 - 3700 cm^{-1} with peak at ∼3450 cm^{-1}.

The power-spectrum or spectral density describes the number of modes at a certain frequency and is obtained by Fourier transform of the velocity auto-correlation function(VACF). Here the spectral density was calculated at different pump-probe time delays (TDs) by Fourier transform of VACF with a defined initial time t=0.

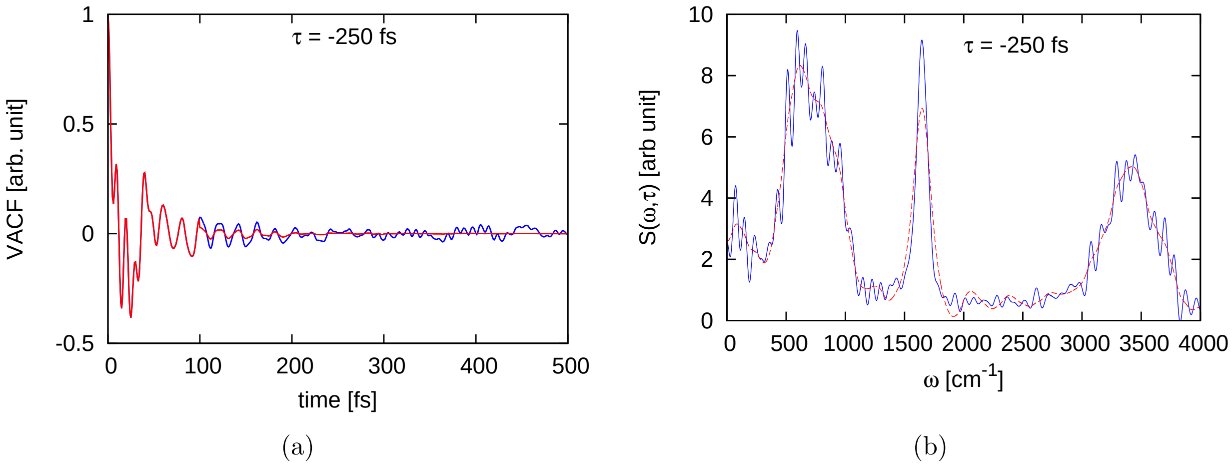

(a)

(b)

Figure 3.8: (a) Velocity auto-correlation function (VACF) and (b) Spectral density (S(ω,t)) of water at pump-probe time-delay τ = -250 fs to show the effect of apodyzation function on the vibrational modes. Blue color presents VACF and S(ω,t) without apodyzation function and red color presents VACF and S(ω,t) with apodyzation function.

$$\mathbf{S}(\omega,\tau) = \int_0^\infty \frac{1}{N}\sum_j \langle \mathbf{v}_j(t+\tau)\cdot\mathbf{v}_j(\tau)\rangle \exp(-t/\alpha)\cos(\omega t)dt \tag{3.5}$$

$$= \int_0^\infty a_\tau(t)\exp(-t/\alpha)\cos(\omega t)dt \tag{3.6}$$

where $S(\omega,\tau)$ is the spectral density of vibrational frequency ω at pump-probe TD τ and v_j is the velocity of the j^{th} atom. Brackets mean the ensemble averaging over different initial conditions. An apodyzation function of exp(-t/α) has been applied to bring the tail of the signal smoothly to 0 and avoid residual fluctuations due to the finite number of trajectories used for ensemble averaging. Therefore, the $\exp(-t/\alpha)$ function brings the tail of $a_\tau(t)$ smoothly to 0 within about 500 fs [120], which in the frequency domain corresponds to a convolution with a Lorentzian profile. In fig: 3.8(a), the VACF was shown at pump-probe time-delay τ = -250 fs to show the effect of apodyzation function. It can be seen that VACF keeps on fluctuating around zero for the longer time without the apodyzation function, whereas it dies out within 200 fs while using apodyzation function.

The VACF fluctuations at shorter times are almost unaffected due to this function. Effect of fluctuations of VACF at longer time on power spectrum can be observed in fig: 3.8(b). All physical vibrational modes are clear and existing while using the apodyzation function.

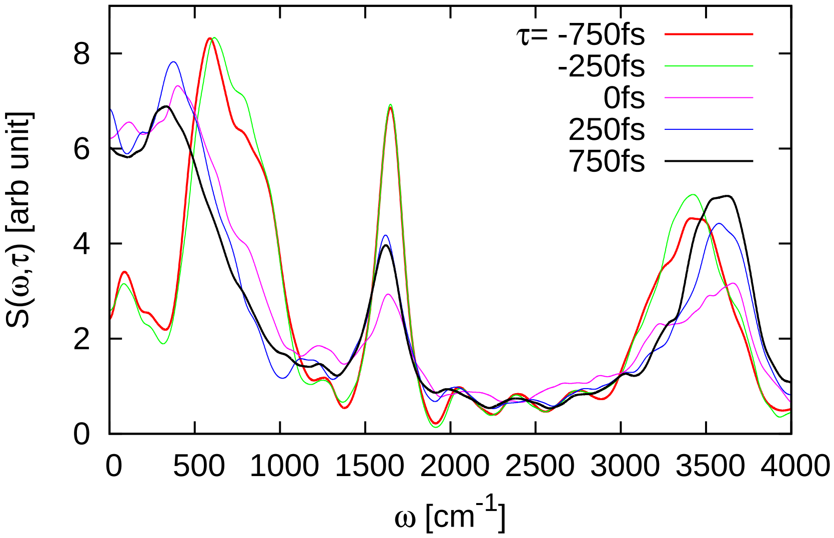

(a)

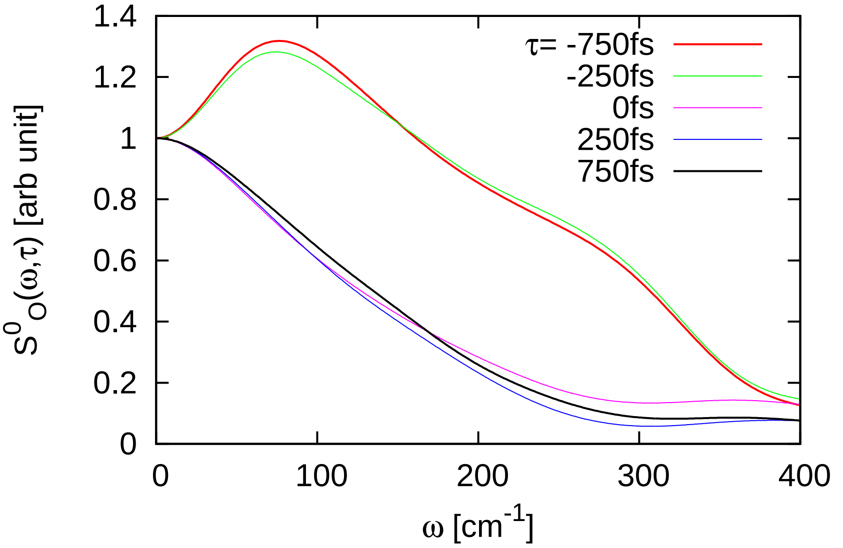

(b)

Figure 3.9: (a) Spectral density of water and (b) Spectral density of only oxygen in water at different pump-probe time-delays

The spectral density of liquid water as a function of the time delay with respect to the center of the THz pulse is shown in Fig. 3.9(a). In this figure, one can clearly follow the strong perturbation of the vibrational structure of liquid in time water caused by the interaction with the THz pulse. The spectra at $\tau = -750$ fs and $\tau = -250$ fs are indistinguishable from the power spectrum of liquid water at room temperature. Right after the pulse, the OH stretching band at 3430 cm^{-1} blue shifts to 3620 cm^{-1} due to disruption of H-bonds whereas the HOH bending mode (1648 cm^{-1}) does not change significantly. The librational motion band at about 585 cm^{-1} red-shifts to about 333 cm^{-1} after the pulse. Librational modes are known to be very sensitive to changes in the H-bonding network [121] and such red-shifts have been observed for water above T=500 K [122]. Our results indicate the T-jump produced by the THz pulse can be followed in time by measuring a transient IR absorption spectrum as a function of the time-delay, for example following the blue-shift of the OH band as the temperature increases within the first picosecond after the THz pump pulse, or alternatively by following the evolution of other spectral features described above.

In the low frequency region between 10 and 400 cm^{-1}, Raman [123, 124], far infrared [125–127] and neutron scattering [128, 129] spectra of liquid water show two weak bands with peaks at $\sim$ 60 and 200 cm^{-1}, which correspond to hindered translational modes involving several water molecules [121]. There has been some debate over the interpretation of the band at about 60 cm^{-1} [121, 123, 130]. The widely accepted interpretation is that the existence of the peak at this frequency corresponds to vibrations of the cage structure formed by various water molecules. The band near $\sim$250 cm^{-1} corresponds to the O-O intermolecular stretching vibrations, i.e., hindered translations of H-bonded molecules [121]. The power spectrum $S^0{}_O(\omega,\tau)$ calculated at different time delays and shown in Fig. 3.9(b) reveals how the long-range structure of water is changed by the THz pulse in this low-frequency spectral region. $S^0{}_O(\omega,\tau)$ is obtained from the VACF of the oxygen atoms only and is normalized to 1 at t=0. This results in cleaner structural information on the concerted network vibrations of water than by inspecting the $S(\omega,\tau)$ spectral density [121]. $S^0{}_O(\omega,\tau)$ at -750 and -250 fs time delays shows the two peaks and is consistent with liquid water results at room temperature [123, 128]. Due to the THz pulse, the mobility of the molecules increases and dramatically changes the network structure. At delay times 0, 250 and 750 fs, the intensity of the band at centered at 250 cm^{-1} decreases due to the depletion of the H-bond network. The disappearance of the peak at 60 cm^{-1} suggests the disruption of any type of cage structure at the level of several water monomers. The power spectrum obtained after the pulse is indicative of a very quick loss of correlation between the relative motions of oxygen atoms in the superheated water on the time scale of a few tens of femtoseconds. From the above analysis, one can conclude that the THz pulse dramatically alters the network structure of liquid water on a sub-picosecond time scale. We emphasize that the heating-up process is ultrafast and that the superheated water, right after the pulse, is still found at the density of liquid water at standard conditions.

3.4 Conclusion

In conclusion, a highly intense THz pulse delivering a power per unit area of 5×10^{12} W/cm^2 to room temperature bulk water on a sub-picosecond time scale results in a large energy increase of the water molecules, to a large extent by interaction with their individual permanent dipole moments, which results in a fast breaking-up of the H-bond structure in the bulk. Water molecules respond to the electric field of the pulse mostly through their individual permanent dipole moments, and a small moment of inertia is also needed to quickly respond and rotate. THz pulses of these characteristics have been recently realized using optical rectification of mid-infrared laser pulses in a non-linear organic crystal [113]. According to our *ab initio* molecular dynamics simulations, each water monomer increases its energy during the pulse by about 2300 cm^{-1}, which gives rise to a kinetic temperature increase from 300 K to about 1050 K. Most of the energy increase occurs within a time window of about 100 fs during which the pulse reaches its peak amplitude of 0.6 V/Å. Hindered translational and rotational vibrational modes of the water monomers gain energy rapidly during the duration of the THz pulse, and internal vibrations (HOH bending and OH stretching) follow with a delay of a few tens of femtoseconds through collisions between monomers.

These changes can be monitored experimentally by time-resolved measurement of coherent x-ray scattering pattern of the liquid. One also observes a blue shift of the OH stretching band from about 3400 cm^{-1} to about 3600 cm^{-1}. This effect is due to the breaking of H-bonds in the super-heated water phase and might be followed by probing the absorption of the medium in this spectral range by a THz pump-IR probe scheme. The disappearance of the structure in the power spectrum in the low frequency region (0-400 cm^{-1}) indicates the depletion of the H-bond network and of any transient structures involving several water molecules, which are present at lower temperatures. The transient and hot gas like liquid environment achieved by the THz pulse can have interesting properties as a matrix to study activated chemical processes and this will be discussed in detail in the next chapter.

Chapter 4

Energy Transfer from Solvent to Solute Induced by Highly Intense and Ultrashort THz

4.1 Introduction

Temperature-jump (T-jump) experiments in liquid water have a long history in the study of chemical kinetics [131–134], as already discussed in chapter: 1. With the advent of femtosecond lasers a couple of decades ago, ultrafast T-jump experiments became possible and have since been used to study the very fast kinetics of fundamental steps in chemical reactions [135], folding processes in biomolecules [37, 136, 137], and fundamental aspects of the hydrogen-bond (H-bond) dynamics and energy transfer in liquid water [111, 119, 138–141] and other liquids [142]. T-jumps in water can be induced, e.g., by targeting the first O-H vibrational excitation of liquid water at about 3400 cm^{-1} with an infrared (IR) laser, thus providing T-jumps in the nanosecond to femtosecond timescales [111, 135, 137–140]. Many examples of T-jump in water by O-H excitation have been discussed in chapter: 1. Nonetheless, T-jumps in water of the order of a few tens of kelvin are still small in comparison with the thermal energy k_BT associated with typical chemical reaction barriers in solution. The fact that $\mathrm{k}_B\mathrm{T}$ is much smaller than typical reaction barrier, is the fundamental reason why reactive events are a clear example of dynamical *rare events*.

In chapter: 3, we explored the application of intense, sub-picosecond THz pulses that are able to increase the temperature of bulk water from 300 K to roughly 1000 K. We investigated the structural properties of the resulting superheated (in the sense that it is not in thermodynamical equilibrium) water phase and how the ultrafast heating-up process of bulk water results in an ultrafast energy redistribution and energy transfer from the superheated solvent to dissolved molecules. We find that the structural properties of water achieved after the short THz pulse resemble those of super-critical water, i.e., water at conditions beyond the critical point at 647 K, 22.06 MPa and 0.32 g/cm^3 [143–145]. However, here the heating-up process of the medium is isochoric due to the very fast energy transfer from the THz pulse to bulk water, which results in a transient phase of superheated water still at the usual density of 1 g/cm^3. Super-critical water is known to be an aggressive solvent which can be used, e.g., in the degradation of biomaterials and in which organic substances have an increased solubility with respect to water at ambient conditions [146].

Phenol, as a solute has gained lot of attention due to interesting phenol-water dynamics. An -OH group on phenyl ring places the phenol in between a benzene molecule and a water molecule in terms of physical properties because of its ability to form H-bond [147, 148]. Phenol-Water system has been an interesting complex system to study the size-dependence ([phenol-$(H_2O)_n]^n$) intra-cluster proton-transfer reactions [149] and to analyze the competition between hydrophilic and hydrophobic solvation. In this studies, it was observed that the presence of water cluster around the phenol changes the vibrational frequency of O-H group of phenol [147, 150] due to H-bond formation. Similar to water, phenol molecules also has the ability to interact with each-other and also with water molecules to form hydrogen bonded clusters. Interestingly, the binding energy of a benzene ring and a water molecule is comparable in magnitude to a water-water hydrogen bond [151]. The understanding of hydration of phenol molecules helps to understand the solute-solvent interaction in chemical and biological processes.

Water molecules mainly interact with the THz pulse through their permanent dipole moments and quickly respond by trying to align along the THz polarization axis, while H-bonds are broken during this process(chapter: 3). The ultrafast energy gain of a solvated molecule in the superheated water environment is determined by collisions with solvent molecules until a quasi-equilibrium is reached. As an example system, we investigate energy transfer to the phenol molecule in solution, which is soluble in water and represents a structural motif common in larger organic and biological systems. Interestingly, whereas the phenol molecule gains a large amount of energy within one picosecond after the THz pulse due to collisions with hot water molecules, the same pulse has almost no effect on gas-phase phenol. This effect can be traced to the substantially larger moment of inertia of phenol as compared to water and is discussed later in greater detail. The phenol-water dynamics also changes significantly due to the modification in potential surface between phenol-water because of H-bond depletion.

4.2 Methods

Ab-initio molecular dynamics (AIMD) simulations were performed with the CP2K molecular dynamics package [79, 112]. The method of the simulations are very similar to what used in chapter: 3. Solvated phenol in water was described in a cubic box with 256 water molecules and 1 phenol phenol at a density of 1 g/cm^3. To obtain a thermalized simulation box the geometrical parameters of the system were first optimized and then the temperature was slowly raised up to 300 K using the Nose-Hoover thermostat to maintain thermal equilibrium. Subsequently, a production run of 3 ps was used to collect 10 initial configurations separated by 300 fs and each initial configuration was then propagated microcanonically (NVE) for 1.5 ps in the presence of the THz pulse. The inclusion of the electric field under PBC when solving the self-consistent electronic structure equations was performed using the Berry-phase approach [62, 152]. Applied THz pulse was same as mentioned in chapter: 3. To study the effect of such pulse on solute molecules in aqueous environment, two systems were compared: one phenol molecule in 256 water molecules at a density of 1 g/cm^{-3} and gas phase phenol (isolated).

4.3 Results and discussion

In chapter: 3, we discussed how a short and highly intense THz pulse applied to liquid water results in a large and sudden kinetic energy increase of the water molecules and, consequently, of the temperature of the medium, mostly by coupling to the permanent dipole moments of the individual monomers and disrupting the H-bond structure of the liquid phase.

In the following, we investigate in some detail the mechanism by which a solute molecule gains energy in this environment. As a test solute system, we consider one phenol molecule placed in a simulation box with 256 water molecules. In the following, we compare the THz response of a phenol molecule in vacuum and in solution to characterize the differential effect that the aqueous environment has on the ultrafast heating process.

4.3.1 Energy Transfer from Solvent to Solute Initiated by a THz Pump Pulse

The total kinetic energy of phenol is partitioned into three contributions; translational energy (TE), rotational energy (RE) and vibrational energy (VE), similarly as before for water in chapter: 3, in order to analyze the energy redistribution to various types of degrees of freedom. Since phenol is a neutral molecule, its center of mass does not interact with a spatially homogeneous electric field, and in vacuum the three translational degrees of freedom (DOF) conserve their energy. Therefore these are not shown. Figure 4.1(a) presents the effect of the pulse on the energy of the hindered translational and rotational degrees of freedom as compared to the rotational energy of phenol in vacuum. Interestingly, the increase in rotational energy (RE) in vacuum is negligible in comparison to the increase of RE and of translational energy (TE) of the center of mass in solution. The permanent dipole moment of an isolated water monomer is 1.85 D [153] whereas for isolated phenol, it is 1.224 D [154]. So, it may be at first instance striking that rotations of

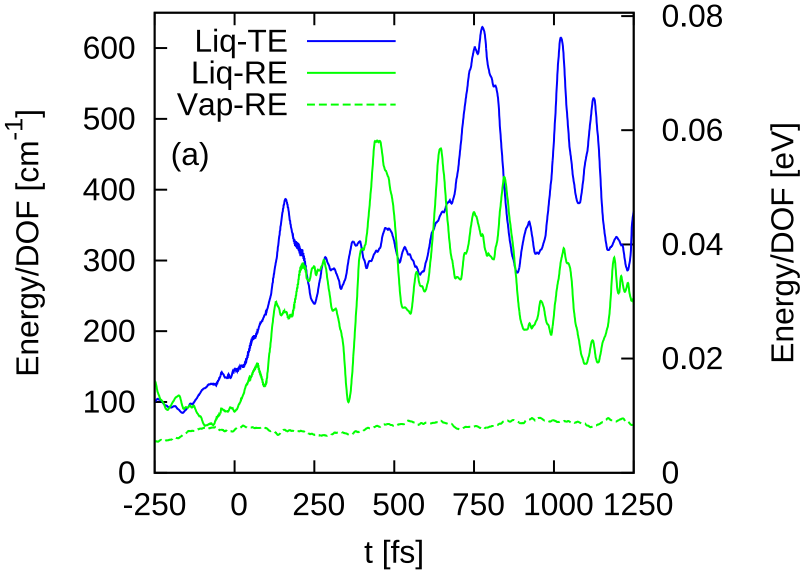

(a)

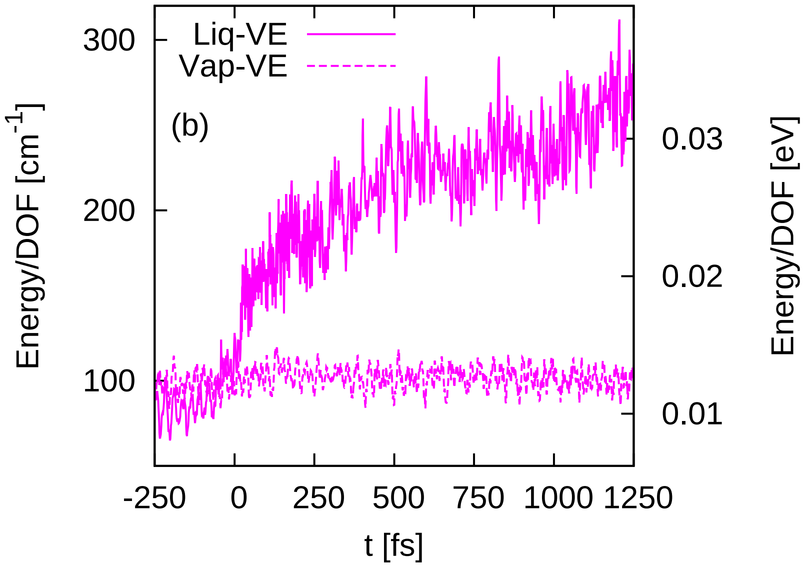

(b)

Figure 4.1: Average kinetic energy of the phenol molecule in different types of degrees of freedom. (a) Translational energy (TE) of the center of mass in the liquid (blue, solid), rotational energy (RE) in the liquid (green, solid) and in vacuum (green, dashed). (b) Vibrational energy (VE) in solution (pink, solid) and in vacuum (pink, dashed).

the phenol molecule are insensitive to the THz pulse in the gas phase as compared to an isolated water molecule [155], at least in view of their not so different permanent dipole moments. For water, the interaction of the monomer's permanent dipole moment with the pulse accounts for a large part of the interaction with the electromagnetic field. The main difference lies in their different rotational constants (or moments of inertia). The three rotational constants are (27.87, 14.51, 9.28) cm^{-1} for a water molecule [156] and (0.19, 0.09, 0.06) cm^{-1} for a phenol molecule [154]. The phenol molecule does not respond to the THz pulse because it is too massive to start rotating within the short pulse duration. In general, many soluble molecules in water will not be able to directly be affected by such a THz pulse, either because of having a small permanent dipole moment, larger moments of inertia than water, or both. This makes the energy transfer mechanism to an aqueous medium with solute molecules using a short and intense sub-cycle THz pulse selective to the molecules of the solvent, which first heat up and then transfer energy to the solute molecules via frequent collisions. During and after the THz pulse, the RE and TE energy contributions of the solvated phenol molecule steadily increase. These motions basically correspond to displacements of the solvated molecule relative to the solvation shell. After the THz pulse, each rotational and translational degree of freedom has increased its mean energy by 150 to 200 cm^{-1} within 1 ps after the pulse. The strong energy variations seen in Fig. 4.1(a) and 4.1(b) result from the limited number of sampled trajectories. A better sampling was not possible due to their high computational cost.

Similarly, the internal vibrational modes of isolated phenol are insensitive to the intense THz pulse, which is seen in the negligible energy increase of the vibrational energy of phenol in vacuum shown in Fig. 4.1(b). Therefore, the vibrational energy increase of the solute is mostly a consequence of collisions with energized solvent molecules. In total, phenol increases its total kinetic energy by more than about 8400 cm^{-1} in the liquid environment as compared to the interaction with the pulse without mediation by the solvent molecules. The heating-up mechanism is clearly illustrated in Fig. 4.2(a), where the average energy increase per DOF is compared for isolated water, isolated phenol as well as bulk water and solvated phenol in water environment. In the isolated water case, we see that the kinetic energy of the molecule increases within the pulse by a similar amount as for water molecules in the bulk. Before the pulse is over, the rotational motion of the water molecule is slowed down again by the pulse by some amount, which is a particularity of the initial conditions of the trajectory shown. Isolated phenol in the gas-phase is insensitive to the pulse as previously discussed, while solvated phenol quickly gains energy from its aqueous environment. Figure 4.2(b) shows the kinetic temperature increase of the solvent water molecules and of the phenol molecule. The temperature of the phenol molecule quickly increases shortly after the surrounding solvent molecules start to gain energy, as seen in Fig. 4.2(b). About half of the temperature increment during the first picosecond takes place after the THz pulse is over, and the final kinetic temperature of phenol reaches about 750 K within 1 ps after the THz pulse. A heating-up curve of the form $\mathrm{T}(t) = \mathrm{T}_0 + \Delta\mathrm{T}_f(1 - \exp(\ln(2)\, t\,/t_{1/2}))$ with $t_{1/2} = 242$ fs, $\mathrm{T}_0 = 350$ K and $\Delta\mathrm{T}_f = 450$ K has been fit to the heating-up curve of phenol obtained from the AIMD simulations. This

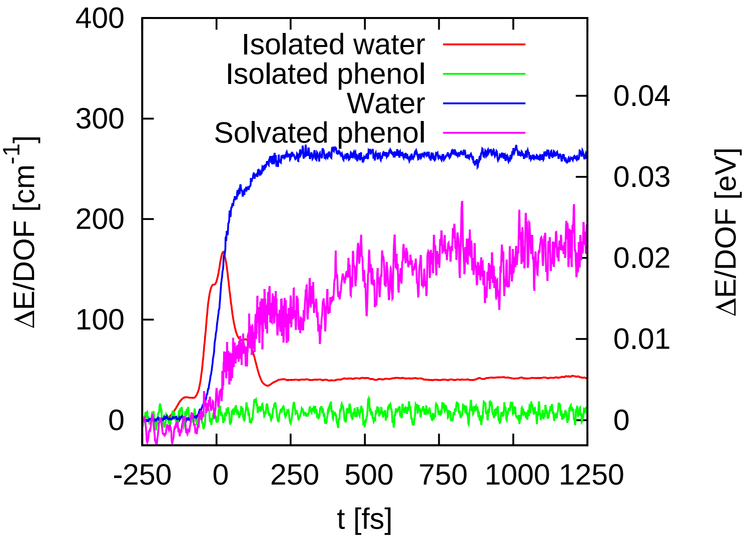

(a)

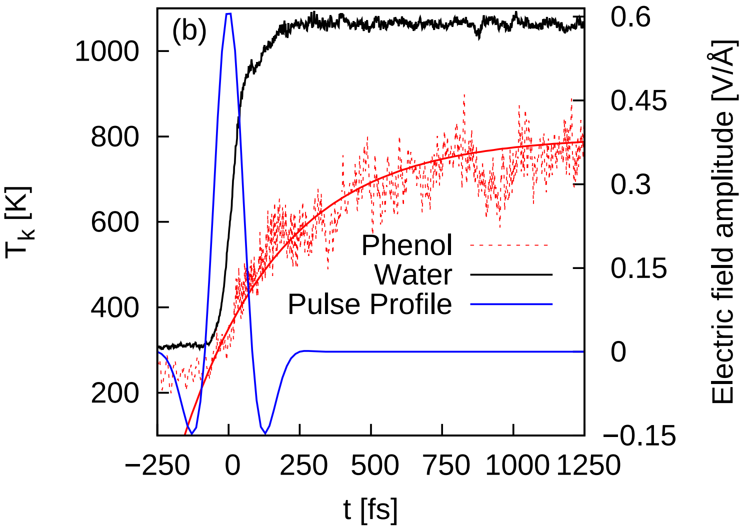

(b)

Figure 4.2: (a) Average kinetic energy increment (ΔE) in each degree of freedom of isolated water (red), isolated phenol (green), bulk water (blue) and solvated phenol in water (magenta). (b) Kinetic temperature (T_K) of water and the dissolved phenol molecule. Water molecules gain energy only for the duration of the THz pulse. The energy of the solvated phenol molecule keeps increasing after the THz pulse due to collisions with water molecules. The solid curve along the phenol dotted red line corresponds to a fit of the form $T(t) = T_0 + \Delta T_f(1 - \exp(\ln(2)\, t\, / t_{1/2}))$ for the heating-up kinetics.

indicates a fast initial energy transfer and corresponding associated temperature increase between 400 and 500 K. However, the asymptotic temperature reached within the simple first-order kinetics model is still more than 200 K away from the final temperature of the bulk. From the length of the propagated trajectories one cannot infer the time-scale of the final equilibriation to the temperature of the surrounding water molecules.

4.3.2 Solvation Dynamics Modification Around the Solute Induced by THz Pump Pulse

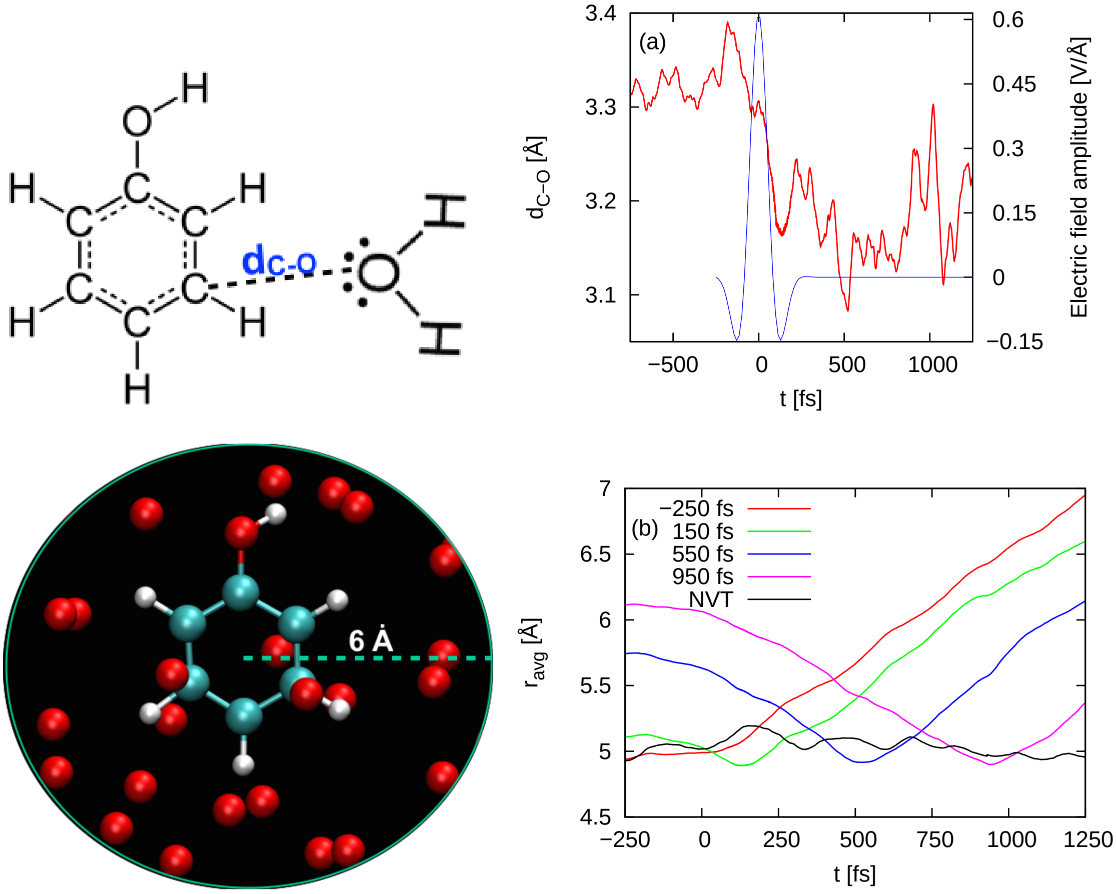

Figure 4.3: (a) Average value of the nearest distance between carbon and oxygen atoms (red), and electric field amplitude of the THz pulse (blue). Only oxygen atoms of the solvent are considered. (b) Average distance between a set of water molecules and the center of phenol ring with time. At each given time the reference set of water molecules was found within the spherical region of 6.0 Å around the center of the phenol ring.

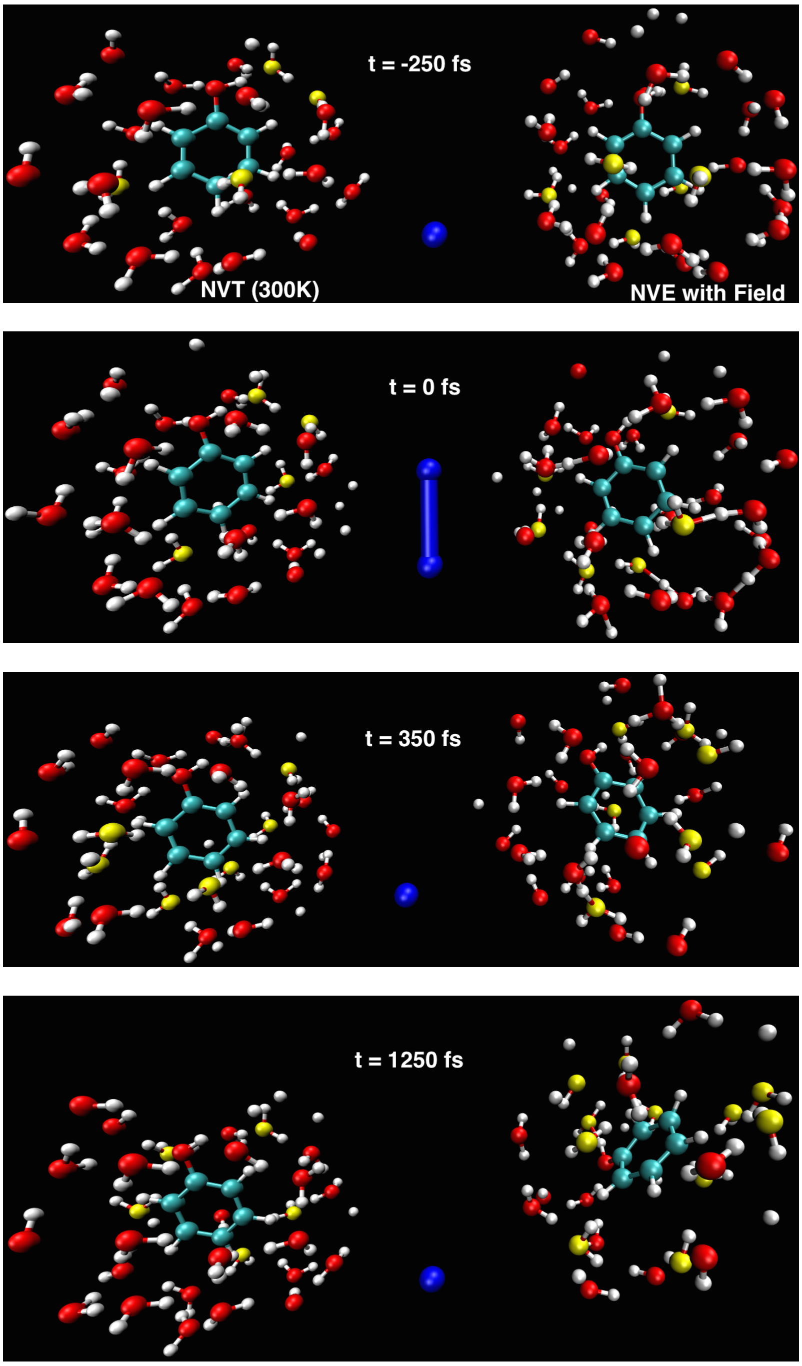

Figure 4.4: Water molecules around phenol within 6 Å are shown. Yellow represents oxygen atoms within 4 Å from carbon atoms (green) and red represents oxygen atoms within 4 Å to 6 Å from carbon atoms. At t = -250 fs, there is no pump pulse. The pump pulse has the peak amplitude at t = 0 fs. By t = 350 fs, the pump pulse is finished.

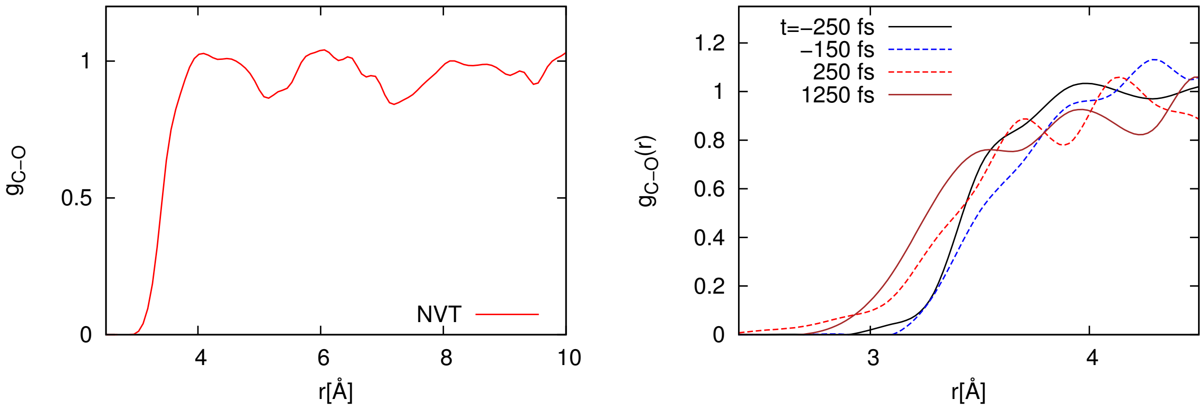

(a) (b)

Figure 4.5: (a) Radial distribution function of C of phenol and O of oxygen (g_{C-O}(r)) for NVT trajectory at 300 K and (b) $g_{C-O}(r)$ at different time-delays during (t = -250 fs, -150 fs) and after the pulse (t = 250 fs and 1250 fs).

As a consequence of the THz pump pulse, the mobility of the water molecules around phenol increases. The more energetic water molecules can overcome to a larger extent the repulsive short range potential with the phenol molecule and consequently the average distance between phenol and neighboring water molecules decreases. The nearest distance between carbon atoms of phenol and oxygen atoms of water (d_{C-O}) is shown in Fig. 4.3(b) as a function of time. During the pulse, d_{C-O} changes from a time-averaged value of 3.38 Å to a minimum of 3.12 Å and then keeps oscillating around a value of about 3.2 Å. By comparing the d_{C-O} graphic and the energy increase of water shown in Fig. 4.2(b), one sees that the shortening of d_{C-O} is insensitive to the particular temporal profile of the THz pulse applied and seems to be a function only of the amount of energy per water molecule. This indicates again that the energy transfer mechanism works by directly transferring energy to bulk water molecules and not by triggering directly the motion of solute-solvent vibrational modes, i.e., displacements of the phenol molecule in its solvation box.

Water molecules in the first solvation shell of phenol exchange at a large rate at the conditions reached after the pulse, whereas there is practically no exchange of the molecules in the first solvation shell at 300 K during in the time scale of a few picosecond. Figure 4.3(d) shows, as a function of time, the average distance between the center of the phenol ring and the centers of the set of water molecules found within a radius of 6 Å of the center of phenol ring at a particular time delay, and compares this distance with its equilibrium value. The rapid exchange of neighbors means that phenol is at all times in contact with very energetic water molecules coming and going from the bulk instead of being surrounded by a static solvation shell. The modification in solvation shell of water can also be observed from radial distribution function g_{C-O}(r) of carbon of phenol and oxygen of water. In fig: 4.5(a), the $g_{C-O}(r)$ is presented for NVT at 300 K. A solvation shell structure of water can be observed around the phenol. Fig: 4.5(b) presents the g_{C-O} at different times (t = -250 fs, -150 fs, 250 fs and 1250 fs). The first non-zero value of g_{C-O} starts at different distances at different times. In discussed above, the average distance between oxygen and carbon (d_{C-O}) decreases due to the pulse, which can be observed from $g_{C-O}(r)$. After the pulse, the g_{C-O} starts from lower value of r. In fig: 4.4, the snapshots of water-phenol systems at different times (t = -250 fs, 0 fs, 350 fs and 1250 fs) during and after the pump pulse, where the water molecules within 4 Å of radius is shown with yellow color and with red color within 4 Å - 6 Å around phenol. In snapshots at different times, it can be observed that Phenol rotates more in presence of the field. The number of water molecules within 4 Å is higher after the pulse. These snapshots present a visual impression of phenol water dynamics in presence of the field compared to the phenol-water dynamics at room temperature. This observation may have consequences, e.g., in the activation of chemical processes in which one or more water molecules may have to play an active role in a chemical reaction. A structured water environment at room temperature activates chemical processes by fluctuations that affect the relative potential energy of reactants, transition state and products geometry [157]. Instead, the superheated environment resulting from the interaction with the THz pulse behaves rather like an idealized environment of hard spheres, which can only activate chemical processes by direct collisions and the transfer of kinetic energy, as is known from chemical reactions occurring within unstructured environments of rare-gas atoms [158].

4.4 Conclusion

A highly intense THz pulse delivering a power per unit area of 5×10^{12} W/cm^2 to room temperature bulk water on a sub-picosecond time scale results in a large energy increase of the water molecules, to a large extent by interaction with their individual permanent dipole moments, which results in a fast breaking-up of the H-bond structure in the bulk (chapter: 3). However, a phenol molecule remains insensitive to the THz pulse when in vacuum due to its higher moment of inertia with respect to water, although its permanent dipole moment is of the same order of magnitude and only less than 50% smaller. In water, the solvated phenol molecule experiences an energy increase of, on average, about 200 cm^{-1} per DOF mostly after the pulse. This corresponds to a T-jump from 300 up to 800 K within one picosecond after the THz pulse. Interestingly, intramolecular vibrations of phenol also gains significantly large amount of energy after the pulse. This energy gain in phenol happens due to collisions by highly energetic and mobile water molecules. Such highly energetic water molecules are able to change the nearest possible distance between water and phenol and is able to go closer to phenol. So, Such THz pulse changes the potential between the phenol and water in sub-ps time-scale. Unlikely to water-phenol at room temperature, the phenol changes its neighbor water molecules very quickly due to strong collisions. The dynamics of solute-solvent appears to be shifted to the state, corresponding to higher temperature (≈800 K) and high diffusivity.

The strong modification in phenol-water dynamics shows that heating by such THz pulse has the advantage of not being mode selective in transferring the energy to the system but to change the dynamics of solvent-solute by increasing the collisions among them. Most of the solutes are either non-polar or having large moment of inertia. Such modification in solute-solvent dynamics is applicable to solutes from polar to non-polar, small to big. Not only dynamics, such heating mechanism is also able to transfer a large amount of energy to internal vibrations of solutes.

Chapter 5

Comparison of *Ab-initio* and Force-field Molecular Dynamics to Describe THz Pulse Interaction

5.1 Introduction

An accurate and universal description of liquid water has always remained a major challenge for theoreticians. *Ab-initio* computational methods have been able to describe structural and dynamical properties of water at different temperatures and densities up to a significant level. However, its not always feasible to use *Ab-initio* techniques due to their high computational cost. To overcome such limitations, the development of accurate force-fields to describe water in all phases has been an area of interest since the beginning of computational molecular science.

There are many water force-fields developed in the past. Example includes 3 point models like TIP3P [159], flexible SPC, SPC/E [160], F3C; 4 point models like TIP4P, TIP4P/2005 [161], TIP4P/2005f [162], TIP4P-Ew, TIP4P-Ice [163], 5 point models TIP5P [164], 6 point model [165] and even polarizable water models [166] etc. A large number of studies on water have been performed using these force-fields, which have produced very similar results as *ab-initio* techniques. The development of such large number of water models illustrates the growing interest in water over time. However, none of the water models have been able to describe the water properties accurately in all the conditions during force-field molecular dynamics (FFMD). For example, some force-fields are good to describe water at low temperature in the ice phase [162, 167] whereas some others explain the liquid phase properties [161] accurately. I. Ohimo *et.al.* showed the molecular dynamics simulation of ice nucleation and growth process leading to water freezing for the first time using the TIP4P water model [167]. Some flexible models can reproduce the vibrational structural of water perfectly [162, 168]. Other models have ability to simulate water well at high temperature and supercritical phase. 3 point models were not able to describe the permanent dipole of water accurately and so, the H-bond network among molecules. To describe the dipole moment and H-bond more accurately, extra virtual charge sites were added in water models [162, 167]. These models with more sites have limitations to describe the polarizability of electronic structure accurately, specially in presence of strong electric fields.

FFMD simulations have also been used extensively to study the chemical or biological processes, but with limitations. To describe the formation or breaking of bond by using force-field is not possible as bonds and angles are defined by fixed potentials. However, FFMD has been widely used to study the processes where restructuring or reorientation of molecules take place. For example, FFMD has been used to study conformational changes in DNA and proteins [169], role of solvent in protein dynamics [170, 171], dynamics coupling of protein modules in protein kinases [172], protein folding [173] and even excited states in reactions in biology [174] like photosynthesis etc. In recent years, efforts are also being devoted to produce force-fields for atoms (known as "Universal Force-fields" [175]) and electrons (known as electron force-field [176]) to describe process where bond formation/breaking or electron movement takes place. So, FFMD has been a successful tool to perform molecular dynamics for studying many physical and chemical properties of solids, liquid and gas with acceptable computational costs, but with the limitations described above.

Here, we studied the pumping of a ultrashort and highly intense THz pulse (similar to chapter:3) on liquid water and studied the energy transfer by the pulse. This study was performed by by using force-field molecular dynamics (FFMD), where forces were calculated using TIP4P/2005f [162] and TIP4P/2005 [161] water force-fields. The kinetic energy gain due to the pump pulse by FFMD was compared with kinetic energy gain via Born-Oppenheimer *Ab-initio* MD (AIMD) simulations. The difference in kinetic energy by both simulation methods were understood by analyzing the energy partitions. The importance of different physical properties like polarization due to electric field, time-scale of simulation, short-range interactions and non-equilibrium dynamics were also discussed to analyze the limitations and advantages of FFMD simulations, in comparison to AIMD. Finally, an effort was made to understand the dynamics of phenol, as an example solute in water solvent.

5.2 Methods

In this chapter, a comparison between FFMD and AIMD was presented for THz pumping on liquid water. AIMD results were presented in chapters: 3 and 4 and used here for comparison. Large-scale Atomic/Molecular Massive Parallel Simulator (LAMMPS) was used as tool to perform all FFMD simulations. Simulation strategies were very similar to what used for AIMD result. In short, the liquid water was thermally equilibriated at room temperature under canonical ensemble. Equilibriated system was then propagated in the presence of THz pump pulse. Here, similar THz pulse (as described in chapters: 3 and 4) was applied in the form of time-varying electric potential. Two kind of water force-fields were used for comparison in energy gain by liquid water which are described below. Potential energy curves (PECs) of water dimer were calculated by using TIP4P/2005f water model in the case of force-field which is compared with PECs calculated by *Ab-initio* method using CP2K.

TIP4P/2005 Rigid Water Model

TIP4P/2005 [161] is a rigid four site model, which consists of three fixed point charges and one Lennard-Jones (LJ) center. This 4^{th} site, known as LJ center or M-site, defines the dipole moment of water accurately. The parametrization of this model is based on a fit of the temperature of maximum density, the stability of several ice polymorphs and other commonly used target quantities. In TIP4P/2005 water model, there is a single LJ interaction site at the oxygen and electrostatic charges at the hydrogens, while the negative charge is placed in M-site along the bisector of the H–O–H angle and co-planar with the oxygen and hydrogens. The intermolecular pair potential has two contributions, Lennard-Jones (u_{LJ}) term and another electrostatic interaction ($u_{electrostatic}$). The important feature of TIP4P/2005 water model is that oxygen does not carry any charge but contributes to LJ potential. Whereas, Hydrogen and M-site are charged but do not contribute to the LJ term. Potential parameters for TIP4P/2005 water force-field are

$$\begin{aligned} \epsilon &= 93.2 \quad K \\ \sigma &= 3.1589 \quad \text{Å} \\ q_H &= 0.5564 \quad e \\ d_{OM} &= 0.1546 \quad \text{Å} \\ r_{eq} &= 0.9572 \quad \text{Å} \\ \theta_{eq} &= 104.52 \quad deg \end{aligned}$$

The total potential energy of the system is the sum of the pair interactions between molecules (chapter 2). This is a rigid force-field which was used with shake algorithm during the simulation. The dipole moment of water is 2.305 D with this model.

TIP4P/2005f Water Model

TIP4P/2005f [162] water model is similar to TIP4P/2005 model but incorporates flexibility for the bond stretching and angle bending. In TIP4P/2005f water model, the intramolecular OH bond is defined by a morse potential. The intramolecular potential energy

($V^{intramolecular}$) is defined by

$$V^{intramolecular} = V_{O-H_1}(r) + V_{O-H_2}(r) + V_{HOH}(\theta) \tag{5.1}$$

where

$$V_{O-H_i}(r) = D_r\{1 - exp[-\beta(r_{OH_i} - r_{eq})]\}^2. \tag{5.2}$$

and

$$V_{HOH} = \frac{1}{2}K_\theta(\theta - \theta_{eq})^2. \tag{5.3}$$

where D_r and β are the parameters of the Morse potential that determine the bond strength and curvature of the potential. r_{eq} is O-H bond length at equilibrium and r_{OH_i} is the instantaneous length. θ_{eq} is angle at equilibrium and θ is the instantaneous angle HOH. K_θ is the angle strength constants.

Potential parameters for water model TIP4P/2005f is

$$\begin{aligned}
\epsilon &= 93.2 \quad K \\
\sigma &= 3.1644 \quad \text{Å} \\
q_H &= 0.5564 \quad e \\
d_{OM} &= 0.1546 \quad \text{Å} \\
r_{eq} &= 0.9419 \quad \text{Å} \\
\theta_{eq} &= 104.52 \quad deg \\
D_r &= 432.58 \quad kJ/mol \\
\beta &= 22.87 \quad nm^{-1} \\
K_\theta &= 367.81 \quad kJ/(mol.rad^2)
\end{aligned}$$

This model also provides the similar dipole moment as in TIP4P/2005.

5.3 Results

In chapter 3, the response of liquid water to THz pump pulse was discussed via AIMD simulations. Keeping in mind the computational cost of AIMD, it is important to explore the possibility of force-field molecular dynamics (FFMD) for such studies. FFMD is known to be computationally cheaper than AIMD. The difference in potential energy surfaces were analyzed for water dimer to understand the the response of water monomers in presence of electric field by both methods. The difference in energy gain by THz pulse provided the limitations of FFMD because of the usage of pre-fitted potential to calculate the energy. The main aim of this study is to establish a ground for FFMD simulation for such studies and find the qualitative boundary up to which FFMD simulations works for such study. AIMD studies were already described in chapter: 3 and 4 by using CP2K.

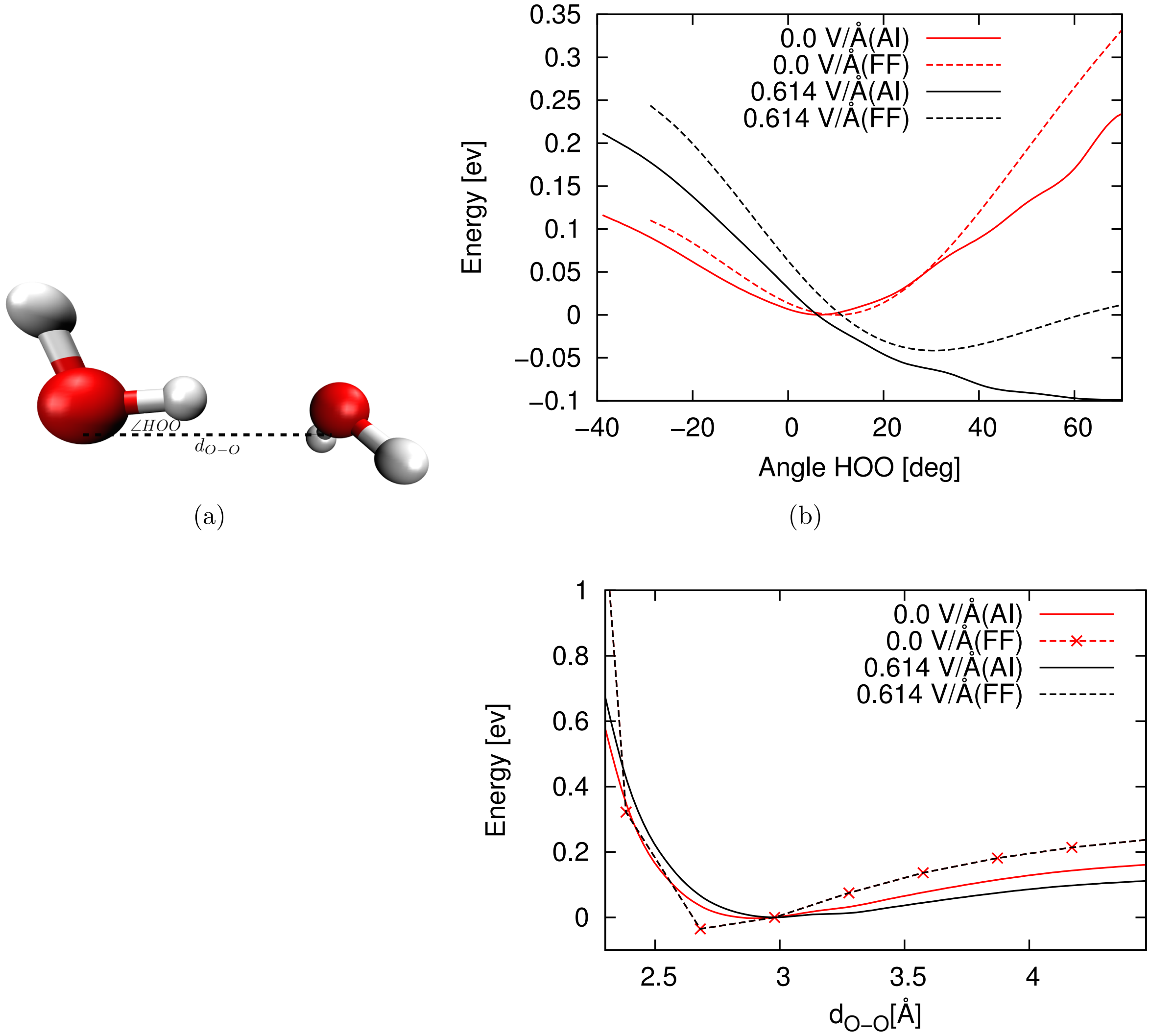

(a) (b)

(c)

Figure 5.1: (a) Schematic of Water dimer to present ∠HOO and d_{O-O}. Potential energy curves of water dimer along the (a) ∠ HOO and (b) O-O distance (d_{O-O}) with electric field amplitude 0.0 and 0.614 V/Å calculated by *Ab-initio*(AI) and fore-field (FF) methods.

5.3.1 Difference in Potential Energy Surface by *Ab-initio* and Force-field

In the fig: 5.1, the potential energy curves (PEC) along the ∠HOO and oxygen-oxygen distance (d_{O-O}) were compared in presence of the electric field with amplitude 0.0 V/Å and 0.614 V/Å calculated via AI and FF methods. The H-bond in the dimer was pointing in the X-direction and electric field was polarized in the same direction. PECs are shifted to zero at the energy value corresponding to minimum energy configuration without field. Without electric field, the PEC for ∠HOO are very similar in the vicinity of minimum energy configuration by both methods, but PEC by FF differs slightly (≈ 0.05 ev) at large ∠HOO (fig: 5.1(b)) with PEC by AI. In presence of static electric field with amplitude 0.614 V/Å, the shape of PEC changes significantly by both methods AI and FF compared to without electric field. PEC for ∠HOO shows dissociative behaviour in presence of electric field calculated with AI. Whereas, the PEC for ∠HOO with FF just shifts to higher ∠HOO for minimum energy configuration but still maintains the shape like a well which is wider and deep than PEC without electric field. So in presence of strong electric field, the PEC for ∠HOO by AI differs significantly to PEC by FF, which will result the different rotational energy by both methods.

The PECs along d_{O-O} are also different by both methods (fig: 5.1(c)) with and without electric field. The Lennard-Jones potential dominates the oxygen-oxygen interaction at the short distance in the case of energy calculation via FF method and water molecules behave like hard wall once they come close to each other than equilibrium d_{O-O} which is 2.98 Å. PECs for d_{O-O} were shifted to zero at 2.98 Å, which is the d_{O-O} for minimum energy configuration and presents the effect on shape of the PEC. Without electric field, there is visible difference in PECs for d_{O-O} at the O-O distance larger than 2.98 Å. In the presence of electric field, it interacts with the permanent dipole moment of water. Here during the calculation, only the distance between the dipoles changes but the orientation with respect to electric field remains same. In the case of FF, energy change due to dipole-field interaction is negligibly small compared to lennard-Jones energy change. So, PECs for d_{O-O} by FF method are strictly similar with and without electric field since the dipole-dipole interaction is identical in both cases in the absence of polarization effect. In the case of AI method, the presence of electric field with amplitude 0.614 V/Å is able to modify the PEC along d_{O-O}. The main reason is the polarizability of electronic cloud due to such strong field.

It is clear that both methods FF and AI provide different potential energy surfaces to water molecules in presence of the electric field. The modification in PECs along ∠HOO as well as d_{O-O} in presence of the field is significantly different calculated by AI and FF methods. So, In the case of bulk water which is the collection of dimers, the change in potential energy surface is significantly large for the calculations with AI method rather than FF method. The effect of different potential energy surface by using two different methods on pumping by FFMD and AIMD was observed in the next section .

5.3.2 THz pumping on liquid water: *Ab-initio* and Force-field MD

We distributed total kinetic energy (KE) in three different partitions like in chapter 3: 1) translational energy (TE), (2) rotational energy (RE) and (3) vibrational energy (VE).

The Energy Transfer to Translational and Rotational modes of Water

In the fig: 5.2, the energy gain in RE (fig: 5.2(a)) and TE (fig: 5.2(b)) due to THz pump pulse were presented, which were calculated by 3 different methods: 1) AIMD, 2) FFMD with shake for rigid force-field and 3) FFMD with flexible force-field. Similar to AIMD results, ΔRE for FFMD doesn't gain energy from starting of the pulse, until the pulse amplitude reaches to a threshold value. It is mentioned in chapters: 3 that THz pulse interacts with the permanent dipole moment of water and water molecules start rotating in the presence of field. The THz pulse requires to have a certain minimum field amplitude to break the H-bond network. The increment in ΔRE happens only, when the intensity of THz pulse is high enough to break the H-bond among the molecules. This shows that water force-fields (TIP4P/2005 and TIP4P/2005f) predict the H-bond strength accurately as in AIMD. Once the pulse crosses the threshold amplitude, the ΔRE increases at similar times for all methods and keeps on increasing few tens of fs after the peak amplitude. Few tens of fs after the pulse, the ΔRE doesn't increase for FFMD. Whereas in AIMD, ΔRE keeps on increasing until the pulse finishes at 250 fs. The increment in ΔRE corresponds to kinetic temperature jump (ΔT) of 780 K by AIMD but, ΔT is only 400 K. The difference in ΔRE can be attributed to the difference in modification in potential energy curve along ∠HOO by AI and FF in presence of the electric field (fig: 5.1(b)). For the case of dimer, the potential energy curve becomes more wider and deeper by AI method than FF in presence of electric field. Once the H-bond among molecule is broken by the pulse, it is easier to rotate the water molecule even by the low field amplitude. That is the reason why the ΔRE increases even by low field amplitude after the peak in the case of AIMD simulation. But in FFMD, this transient state of sudden H-bond breaking in water is not well-defined.

The increment in ΔTE (fig: 5.2(b)) for FFMD is slightly higher than the half of ΔTE calculated via AIMD. Such intense THz pulse breaks the H-bond network among molecules and the water molecules start rotating due to dipole interaction with field. The molecular rotations due to field are highly hindered in liquid water. The increment in ΔTE happens due to highly hindered rotations of the water molecules. ΔTE for FFMD increases with few tens of fs delay comparatively to ΔTE increment by AIMD. The reason behind the delay in ΔTE increment in FFMD compared to AIMD can possibly be the significant modification in PEC for d_{O-O}(fig: 5.1(c)) and polarization of electronic structure in water in presence of such strong field which is well described by AIMD method, but not in FFMD. Interestingly, Saitta and co-worker [62], performed AIMD study of dissociation of Water in presence of strong static electric field. It was shown that such strong electric field

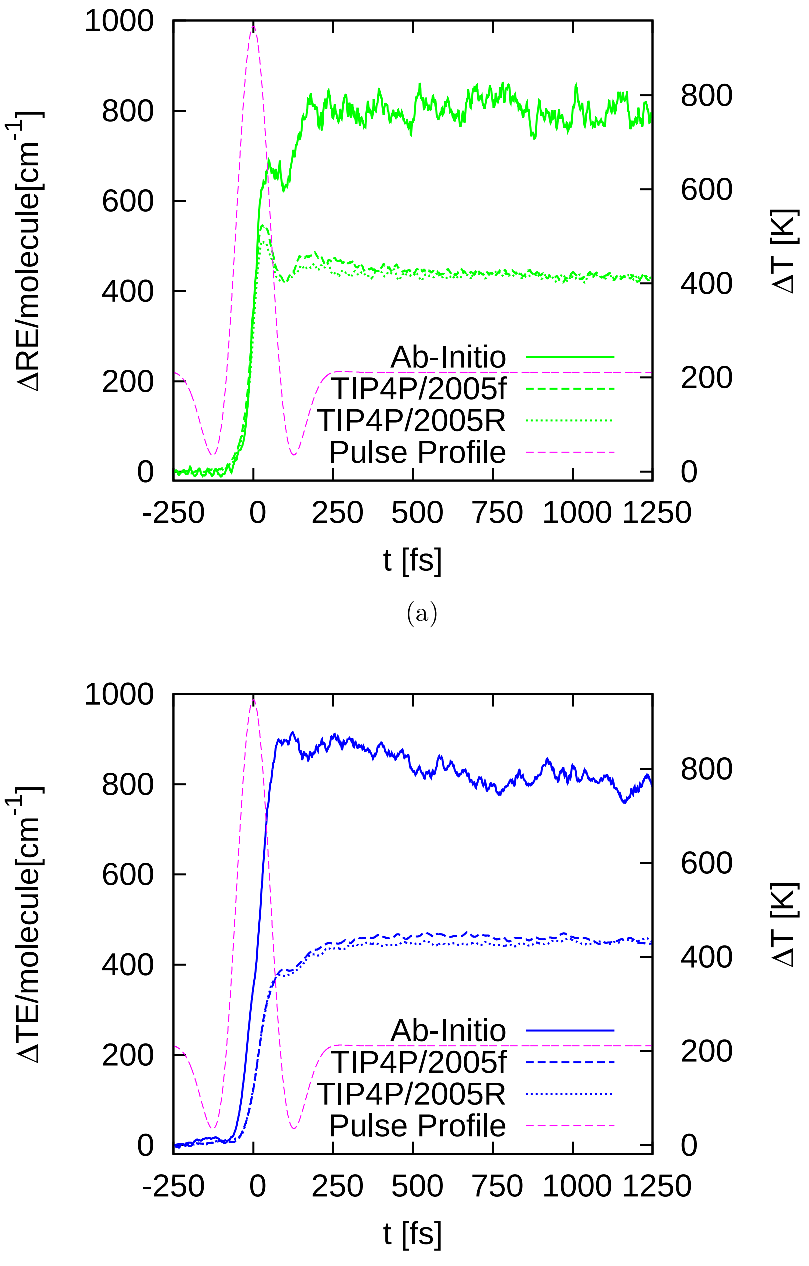

(a)

(b)

Figure 5.2: The gain in (a) translational energy (ΔTE) and (b) rotational energy (ΔRE) of each water monomer computed via AIMD as well as FFMD using TIP4P/2005 (rigid) and TIP4P/2005f (flexible) force-field.

amplitude induces O-H intramolecular polarization, which strengthens the intermolecular O-H interaction during the AIMD simulations. Whereas, FFMD simulations lacks to describe the polarization effect with such water force-fields. Even, static field beyond a threshold of about 0.35 V/Å are able to dissociate molecules [62]. Similar to ΔRE, ΔTE also increases until the pulse ends in AIMD simulations. Whereas ΔTE in FFMD doesn't increase once the field amplitude is lower than threshold value.

Polarization Effect Due to the Field on Water Cluster

Strong electric field can induce the electronic polarization in water [177, 178] and modifies the electronic structure. Polarization is purely a quantum phenomenon. To analyze the effect of THz pump pulse on water polarization, we calculated the quantity of polarized charge in presence of static electric field with amplitudes 0.275 V/Å, 0.475 V/Å and 0.614 V/Å. In the fig: 5.3, the difference in electronic charge density cube with electric field to without electric field was presented for static electric field amplitudes 0.275 V/Å(smallest blob), 0.475 V/Å (middle blob) and 0.614 V/Å(biggest blob) in the water cluster of sizes 2,3,4 and 5 molecules. Here, the applied electric field was polarized along the x-direction. It was observed that the polarized charge density cube expands with increasing the electric field amplitude. Higher electric field amplitude induces the larger polarized charge. This charge density cubes were quantified by calculating the volume of these charge density blobs, which provided the quantity of polarized charge due to the field. The polarized electronic charge density due to electric field were calculated by BADER charge analysis [179, 180] using the charge density cubes. The charge density cubes which were used for charge analysis, are the difference in charge density cubes with field to without field. In the fig: 5.4, the quantity of polarized charge was shown for different electric field amplitudes. If one molecule is negatively polarized, the other is positively polarized at the same time to conserve the charge in the system. The whole system is neutral. So, the molecules having the dipole along the direction of the field are polarized more than the others. The quantity of polarized charge increases with increasing the field amplitude.

AIMD simulations include the polarization effect due to such strong electric field amplitude, because the total electronic energy of the system is computed by solving the SCF equations at each step with the implementation of Berry phase formalism. But, the force-fields don't include the terms for induce polarization. There have been many studies to describe the quantum effects of water molecules and efforts have been made to implement the quantum effects in the force-field. The development of many polarizable force-fields over the period of time have improved the results of molecular dynamic simulations in agreement with experiments. Polarizable water models like polarizable TTM2.1-F force field [181], Amoeba force-field [166] or Martini force-fields [182] etc explained well the hydrogen bonded disordered network of water molecules [183], the orientational relaxation time [184] and breaking and formation of H-bond in ps time-scale. FFMD with TIP4P/2005 and TIP4P/2005f is unable to include such quantum effects in the water system in presence of the strong electric field.

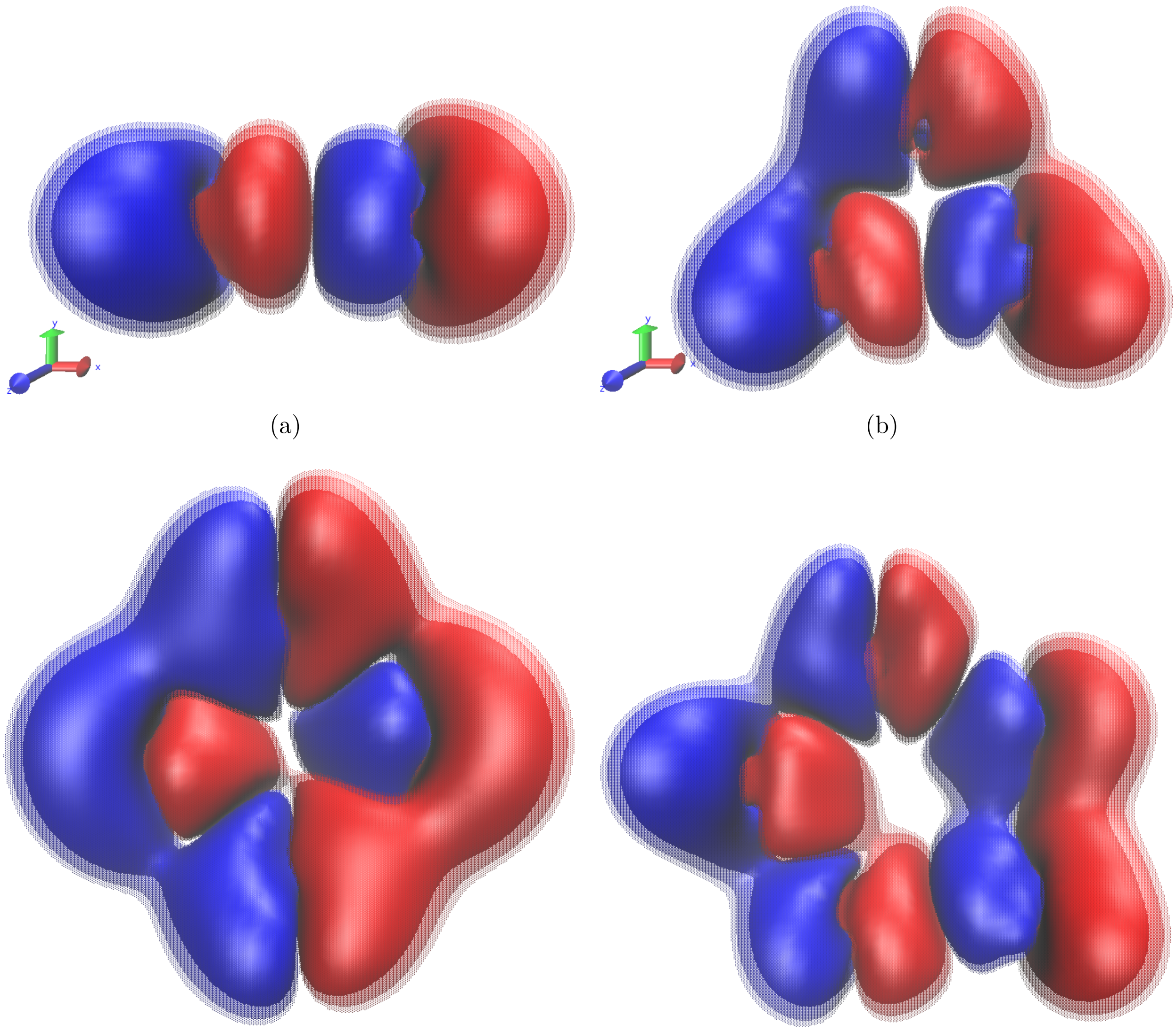

(a) (b) (c) (d)

Figure 5.3: Displaced charge due to polarization in water cluster of sizes 2,3,4 and 5 in presence of electric field with amplitude 0.275 V/Å, 0.475 V/Å and 0.617 V/Å. The polarization direction of applied static electric field was in X-direction. Blob with solid color corresponds to electric field amplitude 0.275 V/Å. Middle blob corresponds to 0.475 V/Å and largest blob corresponds to 0.615 V/Å.

The Energy Transfer to Vibrations of Water

In the fig: 5.5(a), the gain in vibrational energy (ΔVE) is presented for the calculations with both methods AIMD and FFMD with flexible force-field. ΔVE is zero for FFMD

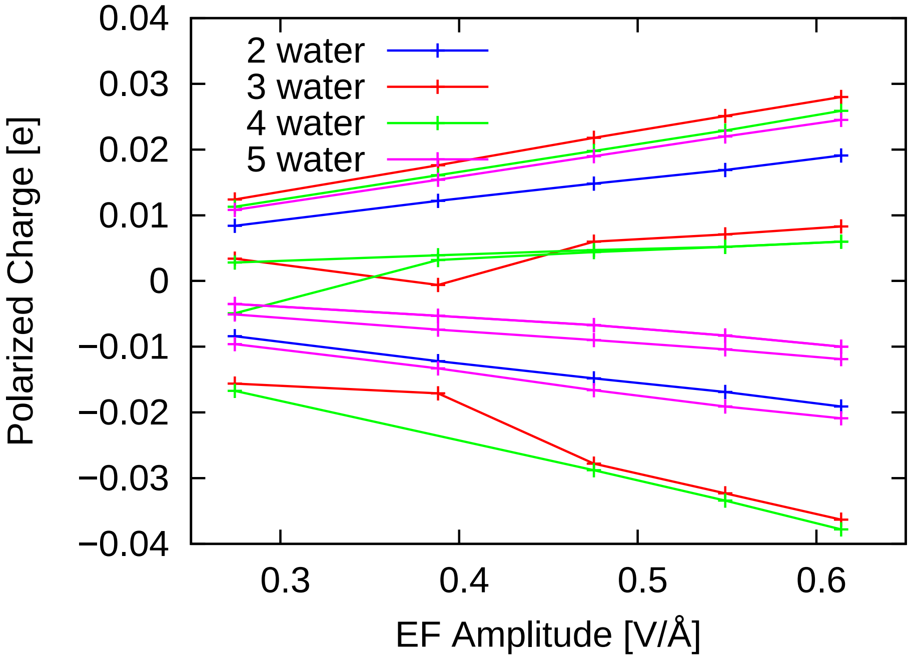

Figure 5.4: Quantity of displaced charge in each water of 2,3,4 and 5 water cluster with static electric field amplitude

with rigid force-field due to use of shake algorithm during the simulation. It was observed in fig:3.1 of chapter 3 that VE increases during the pulse but with few tens of fs time-delay than TE and RE by AIMD method. The vibrational energy increases suddenly during the pulse and keeps on increasing after the pulse. VE gains approx. 800 cm^{-1} of energy within 1 ps after the pulse, which corresponds to 750 K jump in kinetic temperature by AIMD. The significant changes in ΔVE happens very closely to when the pulse is at its peak amplitude. Whereas, there is negligibly small increment in ΔVE during the pulse and very small increment after the pulse by FFMD methods. Total gain in vibrational energy ΔVE within a ps after the pulse is only close to 50 K in terms of kinetic temperature. AIMD and FFMD simulations present very different results for ΔVE in terms of energy gain due to the pulse and time-scale of energy gain.

Basically, total change in ΔVE can be partitioned into two parts: 1) ΔVE during the pulse ($t < 250$ fs) and 2) ΔVE after the pulse ($t > 250$ fs). The changes in ΔVE during the pulse is mainly due to the polarization effect due to strong field intensity as discussed above. As discussed above, the strong field intensity polarizes the electronic structure of atoms, which modifies the dipole moment as well as the H-bond strength. The polarization also changes the O-H stretching vibrations of water molecules. So during the pulse, the increment in ΔVE is mainly due to modification in O-H stretching vibrations with the electronic structure polarization. The changes in ΔVE after the pulse is mainly due to

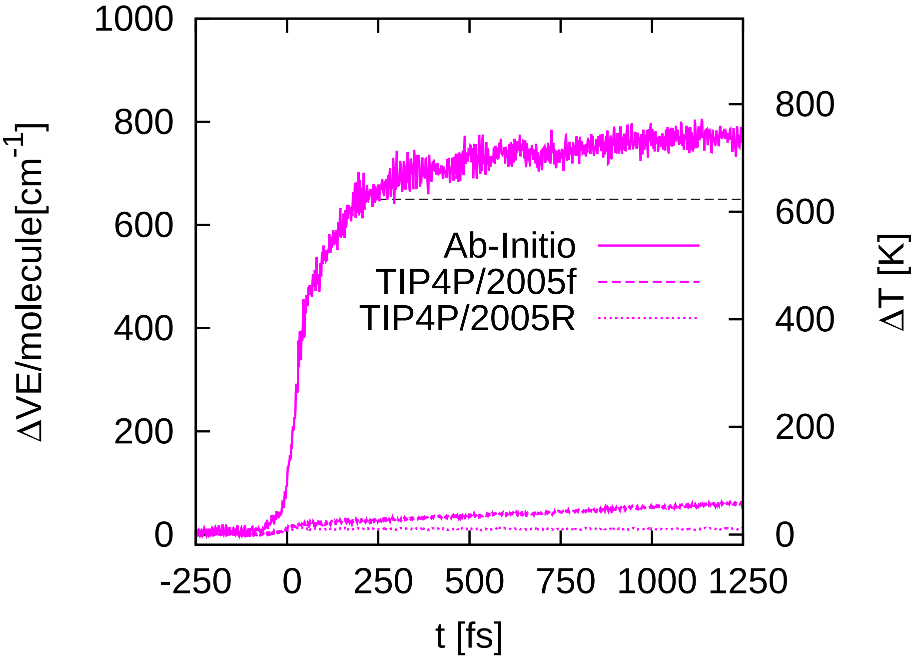

Figure 5.5: The gain in vibrational energy (ΔVE) of each water monomer computed via AIMD as well as FFMD using TIP4P/2005 (rigid) and TIP4P/2005f (flexible) force-field.

collisions among molecules. After the pulse, translational and rotational modes are highly energetic and the energy equilibriation takes place among different modes of water. From the fig: 5.5, it can be observed that FFMD simulations are not able to predict the energy transfer accurately after the pulse. The main reason behind the lack of energy transfer after the pulse can be the non-existence of short range interaction between hydrogen Lennard-Jones potential in the force-field.

Short Range Lenard-Jones Force

TIP4P/2005f force-field considers only oxygen for calculating the Lennard-Jones interactions. It doesn't include the Lennard-Jones terms for hydrogen. In FFMD with such water models, it is feasible to describe the water-water collisions perfectly for the ps timescale and all the degrees of freedom follows Maxwell-Boltzmann distribution at the given temperature. So, FFMD describes the water properties accurately in ps time-scale for equilibrium molecular dynamics. When the collision happens very fast due to large energy transfer, it becomes important to describe the water collisions in time-scales less than ps, where hydrogen interactions with atoms become significant. The OH stretching relaxation has the within 740 fs (< ps). For example, development of F3C water force-field [185] was to use the internal flexibility of the better treatment of protein dynamics or macromolecules

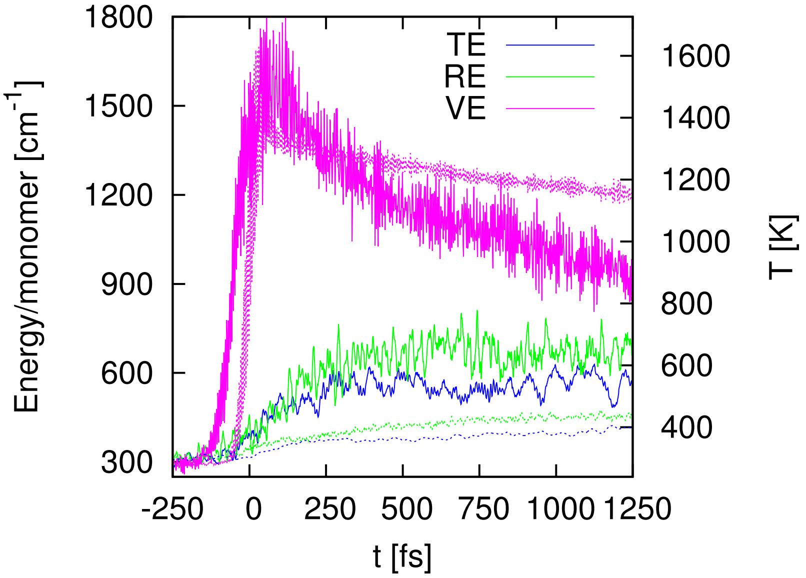

Figure 5.6: Energy partitions translational (TE), rotational (RE) and vibrational energy (VE) of each monomer of liquid water due to IR pump by using AIMD (solid lines) and FFMD (dotted lines).

in solvent by adding Lennard-Jones site on hydrogen atoms as well. Universal force-field could also possibly be helpful to define short-range interaction better. In FFMD, transferring of rotational and translational mode of molecules from 300 K to 700 K within in less than half ps time-scale creates a non-equilibrium state of water in the presence of THz pulse. In the non-equilibrium state of water, different degrees of freedom are in different energetic state. Such state is created within 100 fs of time-scale. FFMD has limitations to describe the water interactions perfectly in fs time-scale for a non-equilibrium dynamics as opposed to AIMD.

FFMD simulation has limitations to describe the non-equilibrium state of the system, which lead to the development of other MD methods like non-equilibrium molecular dynamics (NEMD) to describe well the non-equilibrium system [186, 187]. So, limitations to describe the non-equilibrium state of the system accurately in fs time-scale in FFMD causes the big difference from AIMD.

5.3.3 Infrared Pumping on Liquid Water: Ab-initio and Force-Field MD

To explore the effect of time-scale in energy redistribution, the response of liquid water was analyzed in presence of an Infrared pump pulse. The used infrared pulse has the central frequency of 3500 cm^{-1} which is very close to O-H stretching vibrations. All other characteristics of the pulse were similar to THz pump pulse as described above. In the fig: 5.6, the different energy partitions (TE, RE and VE) were shown for each water monomer due to pump pulse. The energy partitions were compared for AIMD methods with FFMD method. FFMD simulations are performed with TIP4P/2005f force-field. This IR pulse resonates the OH stretching in both methods due to which VE increases during the pulse. In both methods, none of the energy partitions start increasing from starting of the pulse and increases only few tens of fs earlier to peak of the pulse. The O-H stretching doesn't gain energy until the H-bonds softens due to the pulse. Once the H-bond softens, the vibrational energy increases. However, the increment in VE via FFMD starts few tens of fs later than the change in VE by AIMD. This can possibly be the effect of polarization of electronic structure. TE and RE also start increasing in both methods, once the pulse crosses its peak intensity at t = 0 fs. However, the increment in TE and RE increases larger via AIMD than FFMD due to the pulse. During the pump pulse, there is large energy in VE but TE and RE are significantly cold. After the pump pulse, VE starts redistributing among different RE and TE modes due to relaxation. As discussed earlier, the energy redistribution is rather a slow process in FFMD than AIMD due to the lack of accurate description of short range Lennard-Jones forces for hydrogens in the force-field. FFMD lacks to describe the energy redistribution among the different modes of water in the time-scales of less than ps. This can be observed clearly from the fig: 5.6. The final energy gain in VE is approx. 600 cm^{-1} which corresponds to kinetic temperature jump of water from 300 K to 850 K within a ps after the pulse via AIMD. Whereas, VE increases by 900 cm^{-1} corresponding to kinetic temperature jump from 300 K to 1150 K within a ps after pump pulse via FFMD. Large energy gain in VE via FFMD than AIMD is the result of slow energy flow to other modes. The kinetic temperature of RE and TE increases by approx 100 K by FFMD whereas 200 K on average by AIMD. So, the energy relaxation via AIMD is faster than FFMD. This study also supports the argument of inaccurate description of short range forces, which lead to time-scale problem in energy relaxation via FFMD.

5.3.4 THz pumping on solute in liquid water solvent: Ab-initio and Force-field MD

As discussed, FFMD simulation have limitations to describe the energy transfer from THz pulse to liquid water. But, the response of translational and rotational modes to the THz pulse can be described qualitatively up to a certain extent. This makes it interesting to explore the solvent-solute dynamics in presence of THz pulse by FFMD because FFMD provides the flexibility to study significantly large system and long time simulations. In the fig: 5.7(b) and 5.7(a), we compared the translational (ΔTE) and rotational energy (ΔRE) gain by phenol, as an example solute in the water solvent as well as phenol in vapor phase. The response of vapor phenol to the THz pulse via FFMD is very similar to AIMD. In both methods, vapor phenol remains almost unaffected from the THz pulse. The reason is the large moment of inertia of the phenol despite having large dipole moment. The translations

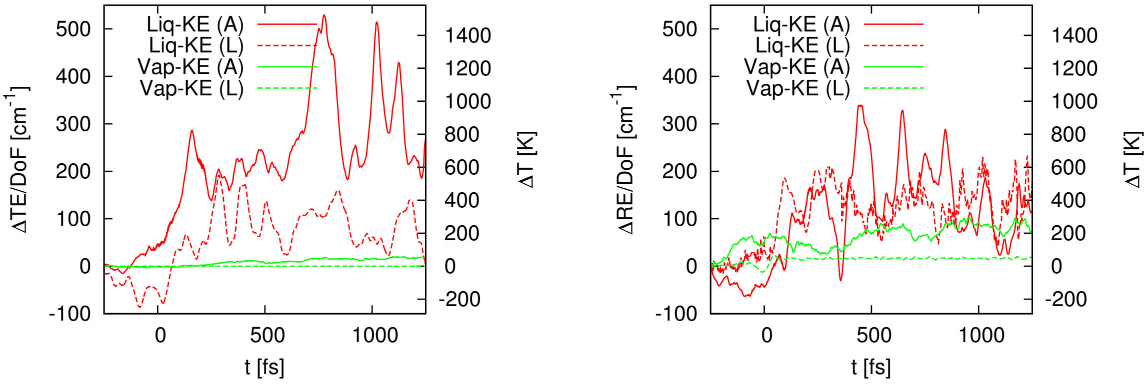

(a) (b)

Figure 5.7: The gain in (a) total kinetic energy (ΔKE), (b) translational energy (ΔTE), (c) rotational energy (ΔRE) and (d) vibrational energy (ΔVE) of phenol, as an example solute, computed via AIMD as well as FFMD using TIP4P/2005 (rigid) and TIP4P/2005f (flexible) force-field. Liq-KE corresponds to phenol in water solvent and Vap-KE corresponds to vapor phenol.

and rotations of phenol in water solvent via FFMD are responsive to the presence of THz pump. The phenol molecule gains the energy in ΔTE(fig: 5.7(a)) and ΔRE(fig: 5.7(b)) via FFMD but less than what it gains via AIMD. ΔVE by FFMD is non-responsive in presence of the THz pulse. The reasons were discussed above for the case of liquid water. The response of ΔTE and ΔRE to the THz pulse by FFMD indicates that FFMD can describe the solvent-solute dynamics.

5.4 Conclusion

Both the methods AIMD and FFMD show that a highly intense and ultrashort THz pulse can transfer a large amount of energy to liquid water. During the computational study of such systems, THz pulse is implemented in the form of a time-varing electric field. In AIMD simulations, energy is calculated by solving the self-consistent field problem at each step, whereas in FFMD, energy at each step is calculated by using the parameterized potential of water. FFMD simulations are able to describe the intermolecular motions well qualitatively in fs time-scale up to a certain limit. The main reason for this is the rigidness of intramolecular vibrations, as described via force-fields which are parameterized either as harmonic or morse type potential. Such strong THz pulse is able to polarize the electronic structure of the atoms. Non-polarizable Force-fields don't include terms for induced polarizability explicitly in force-field. FFMD lacks to include the contribution in energy due to polarization. Another limitations of FFMD is that FFMD describes well the equilibrium system, but it lacks to describe the non-equilibrium system, in which the energy is not equipartitioned in all degrees of freedom. FFMD also have limitations in terms of timescale to define the physical properties. Force-fields also have limitations to describe the fast collisions among the molecules, due to lack of short-range Lennard-Jones potential contribution from hydrogen atoms. Similar limitations are also observed while investigating solute-solvent dynamics using force-field. FFMD lacks to describe the intramolecular vibrations in presence such pulse for the simulations.

In conclusion, FFMD simulations describe qualitatively well to intermolecular modes translations and rotations by freezing the internal vibrations with shake algorithms. The strength of H-bond is perfectly described with force-fields by FFMD which plays key role in THz pumping. FFMD provides the tool to perform the simulations for large systems using the periodic boundary conditions with certain limitations. This can be significant tool to explore the THz interaction with water in different direction and to get a qualitative result. It prepares the ground for exploring the effect of different phases of water on THz pumping. FFMD can also provide qualitative results for chemical and biological processes.

Chapter 6

Sub-ps Energy Transfer From A Highly Intense THz Pulse to Water Cluster and Bulk

6.1 Introduction

Liquid water is a versatile liquid due to its unique dynamic behavior under different circumstances, for example the influence of temperature [188], pressure [189], electric field [62, 190], ultrasound waves [191] and confinements, like slits [192–194] and nanotubes [195–197]. From last few decades, there have been many studies to modify the structure [198] and dynamics [199, 200] of water with electric field. Interestingly, sufficiently strong electric field can modify the strong H-bond network among water molecules and, can even deplete the H-bonds completely in the extreme cases. Due to the H-bond modification, electric field can affect many chemical and biological processes happening in aqueous medium. Examples include the modification in rate constant of folding and unfolding processes of proteins/peptides [201–203], affecting the growth of ice filaments [204, 205], variation in the nucleation process of ice crystallites in cracks on the crystal surface, electrolysis processes and also turning the rate constant of some chemical reaction [206, 207] etc.

To understand the effect of electric field on bulk water computationally has been very complex task due to the complexity involved with the large number of molecules, varying H-bond network and significant modifications in many physical properties due to applying periodic boundary conditions for calculating long range coulombic interactions. There have been several attempts to understand the electric field-water interaction microscopically [208] as well as transformations caused by the field in water clusters. By understanding the water clusters of different sizes systematically in presence of electric field, a guiding line can be drawn for physical properties from water clusters to bulk up to a certain extent. Water in gas phase has permanent dipole moment of 1.85 D [209], which also varies with cluster size and converges to 2.85 for liquid water [210]. In the presence of an electric field, permanent dipole of water interacts with it, exerting a torque. This torque tries to reorient the water dipole along the polarization direction of the field, which perturbs the equilibrium molecular arrangement formed by the H-bond network [211]. If the applied EF is strong enough to overcome the potential energy well of H-bond, the molecules fall into the potential well of the field. The reorientation of the molecules in the direction of EF causes the modifications in molecular arrangement, dipole moment and phase transformation etc. There have been many studies to show the influence of EF on water clusters. For example, the energy of water clusters of different sizes is reduced due to slowly varying electric field in the range of $0.5 * 10^7$-$10 * 10^7$ V/cm [44, 200]. Such intense electric field can also induce the structural transformation in the water cluster's shape like ring to chain [200, 208, 212, 213]. Structural transformation changes the H-bond network and reduce their number on average. Strong electric field polarizes the electronic structure of the atoms (oxygen mainly) and change the dipole moment of monomers, which also depend on cluster size and field strength [214]. Due to weakening H-bond network, the diffusion of water also varies significantly in the presence of the EF [44, 211]. Internal molecular vibrations are also affected in the presence of the EF [212].

Lasers have also been applied on liquid water to make structural and dynamical modifications, as an alternative to apply static electric field. Femtosecond lasers are able to excite internal vibrations by directly putting the energy into the vibrations. When the amount of energy required to break the H-bond is transferred to the system, structural and dynamical changes happen in the liquid. For example, Infrared pulse excites the intramolecular modes of water and energy transfers from intramolecular to intermolecular modes, after the pump pulse. It is possible to break the H-bond network with this energy transfer mechanism. In Ref. [155, 215], liquid water was exposed to highly intense and ultrashort THz pulse and a large amount of energy gain was observed. Interestinglty, it was observed that THz pulse interacts with the permanent dipole moment of water, similar to the application of electric field. THz pump pulse transfers the singificantly large amount of energy to liquid water and modify the H-bond network only, when the pulse intensity is higher than a minimum value, which is similar to the application of static EF. For the computational purpose, the amplitude of a laser pulse profile can be modelled as time-varying EF. The influence of THz pulse on water can also be analyzed with microscopic details as in the case of static EF.

In this work, the behaviour of water clusters of different sizes were analyzed in presence of highly intense and ultrashort THz pump pulse. It was found that the increment in kinetic energy of the clusters due to the pump converges to the bulk water. Potential energy curve in presence of the static EF of the same amplitude as the pulse provided a microscopic picture of water-EF interaction. We also presented a simplistic model for kinetic energy gain in water due to pump pulse in the form of dipole-EF interaction. This study provides a clear physical picture of THz pump on liquid water. The strength of

H-bond among water molecules varies with temperature and density of the system. At temperatures less than the melting point of water, the H-bonds among water molecules are very strong and water is in amorphous solid phase. Density of water is also high at temperatures lower than the melting points. As the temperature increases, the H-bond strength decreases. The water is in liquid phase at temperatures higher than the melting point but lower to the boiling point. At temperatures higher than the boiling point, H-bond network becomes weak or negligible and density decreases. So, the bulk water changes its phase from amorphous solid to gas while changing temperatures from low to high, which results the weaking of H-bond network. As the temperature changes, the water system changes the volume at the atmospheric pressure. The phase-diagram of water for T-ρ suggests [216] that the phase transformation of water is also affected by the density for the closed system. At liquid density (1 g/cm^3) in a closed system, molecules are close enough to form H-bond network even at the temperature higher than boiling point. As the density decreases, both phases of water (liquid and gas) coexist together at temperatures higher than melting point until the density is sufficiently low. Structural phases of water has the significant effect of temperature and density in a closed system and so the H-bond network among molecules is also affected. So, it was interesting to study the interaction of water under different initial conditions temperature (T) and density (ρ) that ranges from amorphous solid to gas phase. A closed system (V=const, N=const) becomes more interesting to study the modifications in H-bond network than an open system. Inertial confinement guarantees the phase transformation in water at short times, as shown, for the case of clusters in vacuum. Otherwise, one can consider the system as really closed by real walls, like in a small experimental cell. From a thermodynamic point of view, if the system has just one phase (high T-low ρ or low T-high ρ) there is no energy loss in doing macroscopic expansion work if the volume in constant, so all the energy pumped is available for whatever process of interest. We presented a comprehensive understanding of THz pump on water under different initial conditions (T and ρ) and discussed the energy transfer mechanism in different modes.

6.2 Computational details

Here, we performed classical molecular dynamics (MD) simulation via LAMMPS, where the forces on atoms in water were calculated using parameterized TIP4P/2005 [161] force field. We used shake algorithm during all MD simulation with using this water model. To study the effect of THz pump pulse on water clusters, 1000 initial configurations were generated for each cluster size from a long canonical (NVT) MD trajectory at 200 K, where each initial configuration was separated by 10 ps time-interval. Nose-Hoover thermostat was used to maintain the temperature during the NVT simulation. We selected the water clusters of the size 1, 2, 4, 8,32 and 64 water molecules. The velocity-verlet algorithm was used to integrate the equation of motion during the dynamics with a time step of 1 fs. The short-range Lennard-Jones interactions were calculated with a cutoff of 15.0 Å. All the water cluster calculations were performed with non-periodic boundaries in all directions to avoid the long range Coulombic interaction due to periodic images of the atoms in the cell. All 1000 trajectories for each water cluster size were propagated under microcanonical (NVE) ensemble in the presence of the for 1.5 ps time with a time step of 1.0 fs. The results presented for water clusters of each size were ensemble average over all 1000 trajectories. The water system with 2048 molecules of density 1 g/cm^3 was also equilibrated at 200 K under NVT ensemble with periodic boundary condition. Equilibrated configuration at 200 K was propagated with NVE MD in presence of electric field, to compare the energy with clusters. To study the effect of temperature of water system on energy transfer by THz pulse, 2048 water molecules in a cubic box were thermally equilibrated at temperatures 200 K, 300 K, 400 K, 500 K and 600 K. The thermal equilibrations were performed for cubic boxes of two different water densities (ρ) 0.296 g/cm^3 and 0.019 g/cm^3. Then, each equilibrated system was propagated microcanonically for 1.5 ps long time in the presence of similar THz pulse. In a similar fashion, to explore the effect of density, similar set of calculations were performed for cubic boxes of 2048 water molecules but with densities 1.00 g/cm^3, 0.296 g/cm^3, 0.064 g/cm^3 and 0.019 g/cm^3. All boxes were thermally equilibrated at 300 K and 500 K. Here, all the simulations were performed under periodic boundary conditions.

THz pump pulse used during the simulation is given by

$$\mathbf{E}(t) = \epsilon(t)\mathbf{u}_z \cos(\omega_c t + \phi), \tag{6.1}$$

where $\epsilon(t) = A\exp\{-(t - t_0)^2/2\sigma^2\}$ is a Gaussian envelope with $\sigma = 84.93 fs$. This corresponds to a full width at half maximum (fwhm) of $\epsilon^2(t)$ of 141 fs. The maximum electric field amplitude $A = 0.6137 V/\text{Å}$ corresponds to a power per unit area of $5 \times 10^{12} W/cm^2$. We consider a mean photon energy $\omega_c = 100$ cm^{-1} (≈3 THz). $\mathbf{u}_z$ is the polarization direction of the electric field and ϕ is the carrier to envelope phase which is $\pi/2$. Such pulse is between a half and a full cycle long. The THz pulse envelope is centered at $t_0 = 0$ fs and microcanonical trajectories start at $t = -250$ fs.

6.3 Result and Discussion

In Refs [155, 215], it was investigated that a one and half cycle THz pulse with peak power per unit area 5×10^{12} W/cm^2 (corresponding to peak field amplitude 0.613 V/Å) of 100 cm^{-1} central frequency, is able to transfer a significantly large amount of energy to the liquid water. Such highly intense and ultrashort THz pump pulse doesn't ionize the water, but successfully breaks the strong H-bond network among the water molecules. This study provided a macroscopic observation of strong THz pulse interaction to the liquid water. Here, we will investigate microscopically the physical properties of water, responsible for such large energy jump due to the pumping.

6.3.1 Interaction of THz Pulse with Water-Cluster

Water Monomer and Dimer

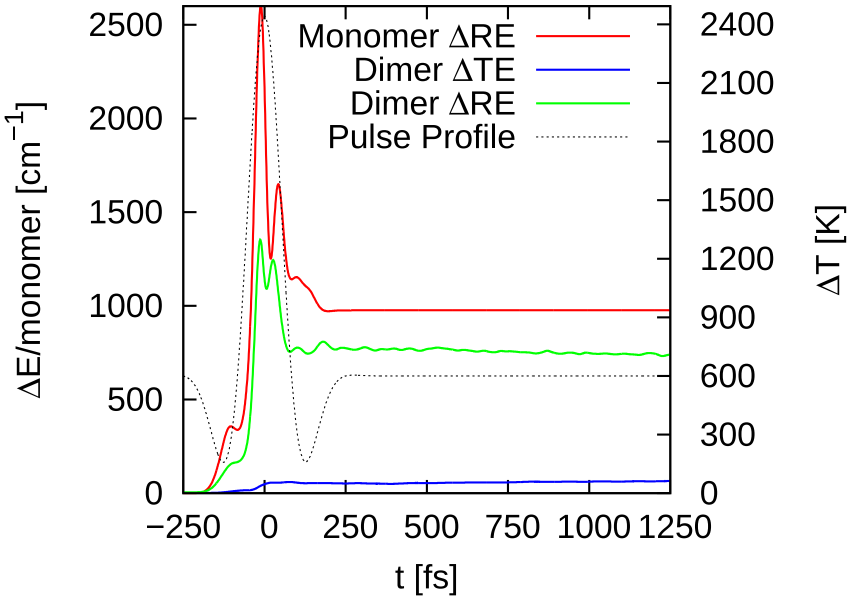

Figure 6.1: the gain in Translational (ΔTE) and Rotational Energy (ΔRE) per water monomer for monomer and dimer is shown along with corresponding kinetic temperature jump (ΔT). The pulse profile is also shown with black dotted line.

In this study, the total kinetic energy (KE) of the system is distributed into three different partitions: 1) translational energy due to the translation of center of mass (TE); 2) rotational energy (RE) due to rotations around the axes and 3) vibrational energy (VE) which include all internal stretching and bending, similar to Ref: [155]. Shake algorithm was used during the simulation, so ΔVE was considered zero during the simulation. In the fig: 6.1, the average ΔTE and ΔRE per water monomer is presented for isolated water and dimer. The energies in fig: 6.1 was averaged over 1000 different different trajectories started with different orientations of the monomer and dimer. The polarization direction of THz pulse was z-direction during the simulation. ΔTE is considered zero for isolated water, because water is a neutral molecule. The increase in KE for isolated water happens only due to the rotation of molecule in the presence of EF. It was observed that when the dipole of water is along the polarization direction of the EF, there is no rotation in the molecule and hence, no energy gain in KE. ΔRE jump significantly only few tens of fs earlier than the pulse reaches to its peak amplitude (fig: 6.1). ΔRE for isolated water is showing the structures at the times, when the pulse changes its polarization direction. ΔRE changes during the pulse, and remains constant after the pulse. Interestinglty for the water dimer, the ΔTE and ΔRE both increase during the pump pulse. ΔTE becomes significant only after the pump pulse crosses certain minimum intensity (≈0.3 $V/\text{Å}$). The oscillating behavior of ΔRE of isolated water due to change of polarization of pulse doesn't appear in the case of ΔRE of dimer.

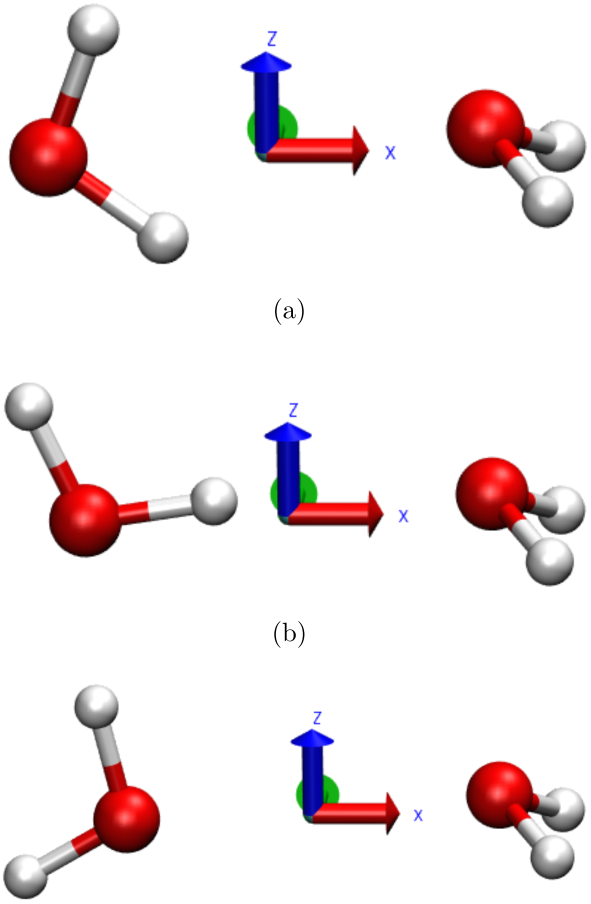

(a)

(b)

(c)

Figure 6.2: 3 different possible orientation of monomers in the water dimer. Water monomers at (a) minimum angle, (b) equilibrium angle and (c) maximum angle configuration without EF corresponding to which PECs for ∠HOO were calculate.

It is well known that the intra-molecular stretching and bending modes are high frequency modes which falls in infrared frequency region [101]. So, THz pulse does not excite any particular intramolecular mode, but rather interacts with the collective modes in liquid water, which include more than one molecules [68]. From the above analysis, it can be observed that there are two types of vibrational modes, which are affected due to THz pump: 1) translational modes related to the center of mass motion and 2) rotational modes corresponding to rotations of the water molecules. To understand the microscopic picture of energy gain, the potential energy curves (PECs) of the water dimer were analyzed in the presence of the static electric field (EF) of different intensities. In the fig: 6.3, PECs are computed along the ∠HOO for the water dimer. The PECs were calculated by using TIP4P/2005 water force-field parameters.

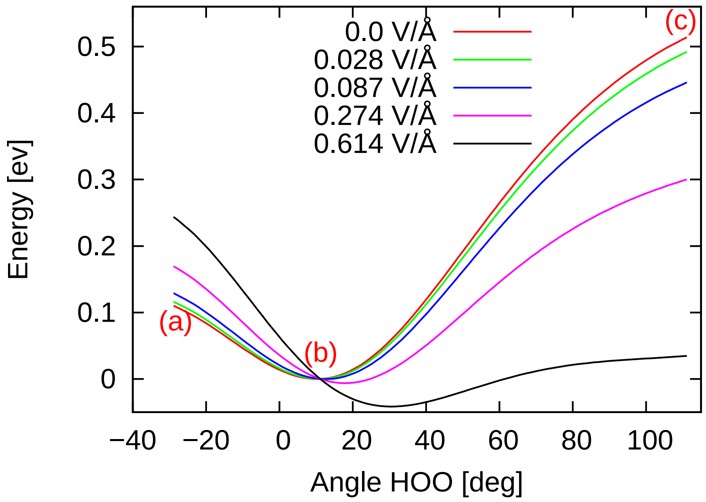

Figure 6.3: Potential energy curve for HOO angle with different electric field amplitude and compared without field. The labels (a), (b) and (c) correspond to the water dimer configurations as shown in fig: 6.2.

In the minimum energy configuration of dimer, two water monomers reorient themselves at a certain equilibrium angle with respect to each other to form the Hydrogen-bond (H-bond), while keeping them close together. The applied static EF is polarized along the X-direction which is the direction of the H-bond in the minimum energy configuration configuration of dimer (fig: 6.2(b)). For PECs along the ∠HOO, the donor water molecule was rotated in the XZ plane i.e. around the Y axis. The PECs were shifted to zero at their corresponding ∠ HOO ($\approx$ 6 degree) of minimum energy configuration so that PECs present the comparative effect on the shape of the potential in presence of EF. PECs were compared for the static EFs with amplitudes 0 (no field) , 0.028, 0.087, 0.274 and 0.614 V/Å which correspond to peak power per unit area of 0, 10^{10}, 10^{11}, 10^{12} and 5×10^{12} W/cm^2, respectively in the case of a pulse. Changing the field intensity from 0.274 V/Å to 0.613 V/Å, the potential changes significantly large in comparison to other lower intensities. Interestingly, the PEC for ∠HOO shows drastic changes in the presence of EF with amplitude 0.614 $V/$Å than without EF. Such high EF is able to create a very deep potential well for the water molecules. The PEC at 0.614 $V/$Å changes abruptly in comparison to other low intensities and this behaviour signifies the dissociation of molecular rotations in the presence of such large amplitude field(fig: 6.3). Due to such potential energy state, molecules reorient themselves in the direction of the field, which is far from equilibrium orientation of the molecules. So, in presence of the EF, the potential well of

H-bond opens and molecules gets trapped in the potential of the field. The molecular rotations from the minimum energy configuration breaks the H-bond network. From the fig: 6.3, it can be pointed out that THz pulse interacts with the permanent dipole moment of water due to the fact that the pulse has sufficiently long wavelength to affect the moment of inertia of the water molecule, rather than interacting with any particular inter or intra-molecular vibrational modes. This is the main reason why energy increment in water monomer happens in rotational contribution only. A delayed gain in TE in fig: 6.1 accounts for that fact that until the intensity of the pulse is higher than the certain minimum value, molecular rotations are not sufficiently hindered to break the H-bond network to make rotations out of their preferred orientation and starts moving away from each other. It is well known that water molecule has a permanent dipole moment of 2.85 D [74, 217] in liquid phase. But, the dipole moment is just one term in the multipole expansion. Higher order multipole terms like quadrupole, octupole and hexadecapole etc. also exist in the multipole expansion. There have been many studies to find the importance of quadrupole or higher pole moment on the properties of liquid water [218, 219]. Quadrupole contribution becomes significant in orientationally ordering in a dense water system [218, 220, 221] and can also affect dielectric constant of water [222]. But, there is no observation on the effect of higher ordered multipole moments except dipole moment of water in the presence of the static electric field. In a simplistic view, the significant changes in the PECs for ∠HOO in presence of the strong EF is accounted for the interaction of dipole moment of water with EF. Liquid water can also be viewed as the sea of interacting dipoles which are bounded by Lennard-Jones potential as well. So, the THz pulse pumping on liquid water can be understood well by understanding the dipole-electric field interaction. THz pulse was employed as time-varying EF during the simulations.

For the bulk water, the total energy (E^{tot}) of the system in the presence of the EF consists of the following terms:

$$E^{tot} = E^{w-w}_{pair} + E^{w-field} \tag{6.2}$$

E^{w-w}_{pair} accounts for the pairwise energy due to water-water interaction and $E^{w-field}$ accounts for the energy due to water-EF interaction. The force applied on a water molecule due to electric field ($\mathbf{E}$) can be written as

$$\mathbf{F}_{coul} = \sum_{i=1}^{N}\sum_{k=1}^{3} q_k \mathbf{E}, \tag{6.3}$$

where q_k is the effective partial charge of kth atom of the molecule. $E^{w-field}$ is the interaction energy between the permanent charges of water molecules and the external field, which is similar to dipole interaction with field (eq: 6.4).

$$E^{w-field} = -\sum_{i=1}^{N}\sum_{k=1}^{3} q_k(\mathbf{r}^i_k.\mathbf{E}) = -\sum_{i=1}^{N} \mu\mathbf{E}, \tag{6.4}$$

r_k^i is the position vector of the k^{th} point charge of the i^{th} molecule, μ is the total dipole moment of the water molecule and E is the external field directed along a polarization direction.

So, considering the water as dipole, the potential energy for two interacting dipoles with dipole moments(fig: 6.4) μ_i and μ_j at time t during the field can be written as

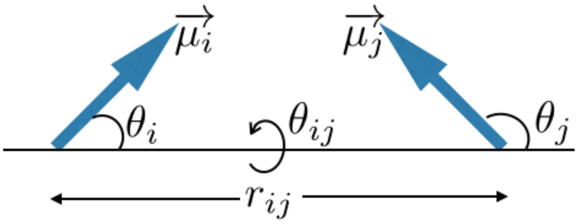

Figure 6.4: Schematic diagram of two dipoles having dipole moments μ_i and μ_j is shown where θ_i and θ_j are their respective angles with line joining to them.

$$V_{i,j}(t) = -\frac{\mu_1\mu_2}{4\pi\varepsilon_0 r_{ij}(t)}(\cos\theta_{ij}(t) - 3\cos\theta_i(t)\cos\theta_j(t)) \tag{6.5}$$

where $r_{i,j}(t)$ is the distance between the center of mass of two dipoles. $\theta_{i,j}(t)$ is the relative angle made by i^{th} and j^{th} dipoles, whereas $\theta_i(t)$ and $\theta_j(t)$ are the angles formed by the two dipoles with respect to the lines connecting to their centers. EF tries to rotate the dipoles along the field direction. The application of time-varing electric field changes the relative angles $\theta_{i,j}$ between dipoles as well as their respective angles θ_i and θ_j, which changes the potential energy due to dipole-dipole interaction. So, the application of the time dependent electric field tries to change the orientation of the dipoles (θ_i, θ_j) as well as the relative distance between the dipoles($r_{i,j}$) at every time step. In the fig: 6.5(a), the minimum energy configuration of water dimer is presented where two water molecules are forming a H-bond and their respective dipoles having dipole moment μ, are pointing in the opposite directions. It was observed that dipoles try to align in the polarization direction of the field (fig: 6.5(b), 6.5(c) and 6.5(d)). In the presence of strong EF, the molecular dipoles align themselves in the direction of the field. When the dipoles are in the same direction, the molecules are in higher potential energy state and try to go away from each other. This dipole-dipole interaction in presence of the EF results the rotations as well as translations in the molecules. Due to Lennard-Jones forces, molecules can not come closer than minimum distance. Once there is no electric field, hindered and energetic water molecules try to come again in minimum potential energy state. The liquid water has all possible configurations of dipole-dipole interactions. So, the electric field changes the potential energy surface for the whole water system. When the water dipoles try to realign in the direction of the field, Lennard-Jones force resists them to come closer to each-other beyond a distance, which forces the center of mass of the molecule to move. This will change the translational and rotational component of kinetic energy. The application

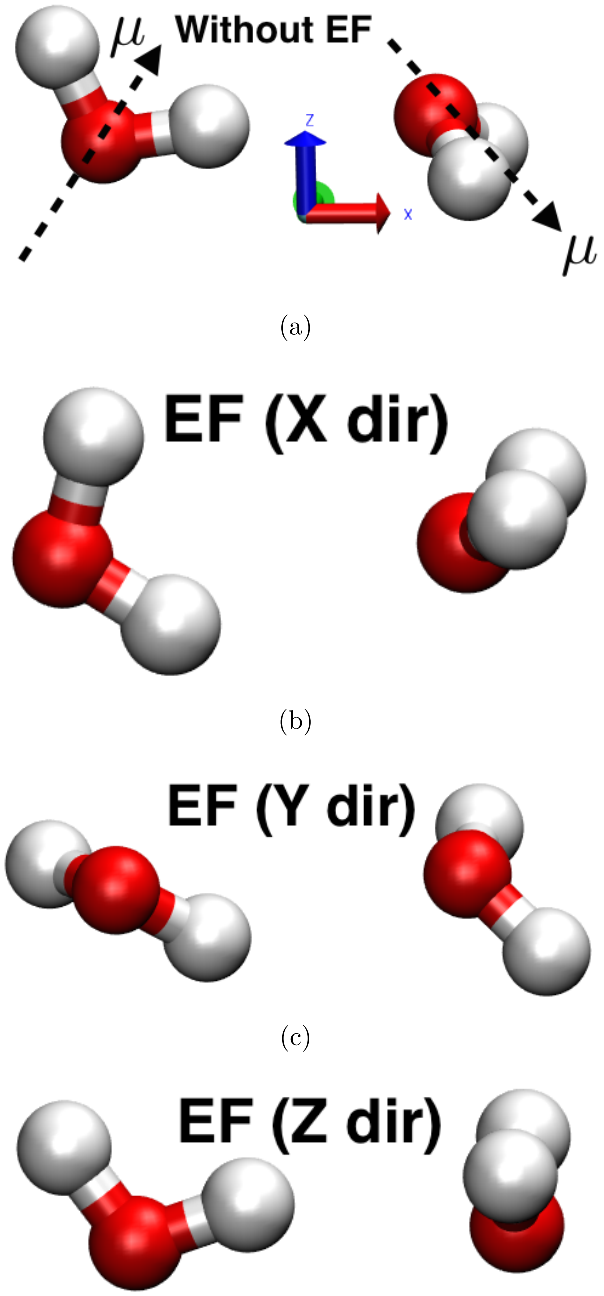

(a)

(b)

(c)

(d)

Figure 6.5: Snapshot of water dimer when (a) there is no EF and EF points in the (b) X-direction, (c) Y-direction and (d) Z-direction. In the fig:(a), the dotted lines are presenting the dipole direction of the water.

of EF leads to a nonzero and nonconserved total angular momentum of molecules which affects the translational and rotational motions of the individual water molecules.

The water dipole-dipole interaction leads to the formation of strong H-bond network among molecules. The H-bond strength is 23.8 KJ/mol [223]. It is observed that the strong H-bond network can't become weak or broken until the electric field amplitude is above a certain value [200, 212]. E_c is the minimum electric field amplitude required to induce significant H-bond modification and structural changes in liquid, which is found to be between $0.2 \sim 0.15$ $V/\text{Å}$. Total THz pulse which is rather a time-dependent electric field, can be divided into two different parts:

1) When $E < E_c$;

Until when the EF amplitude is zero or low ($E < E_c$), reorientations of the dipoles are more or less subject to the same environmental torques due to the motions at the given temperature [199]. The EF ($E < E_c$) has insufficient energy to rotate the water molecules out of their strongly bonded H-bonded orientation. Such EF amplitude is far from inducing any appreciable macroscopic polarization. Water molecules do not experience any coulombic force from a uniform electric field, as they are neutral. Due to dipole - field interaction, they feel only torques. The torques exerted by the field on the water molecules, enhance their rotational motion. But such low field could not increase the ability of water molecules to overcome steric hindrances of neighbor molecules, which are bounded through the H-bond network.

2) When $E > E_c$;

When the EF is stronger than E_c ($E > E_c$), the molecules acquire the energy to come out the potential well of neighbors and gets trapped in the potential well of the EF. The tumbling librations of the water dipoles get progressively decoupled from the spinning rotations about the dipole axis due to EF. In a sense, molecular rotations occur on separate, well distinguished time scales in presence of field which is different than diffusive thermal molecular rotations. In the presence of strong EF, the molecular dipoles are trapped in a deep, single-well potential $V(\theta) = -\mu E \cos(\theta)$ of the field. For such strong EF, force exerted by EF on molecules becomes stronger than hydrogen bonded interactions among molecules because a different type of potential governs the molecular spinning motions around the dipole axis. A water molecule has $C_{2\nu}$ symmetry [224]. In very strong field, a water molecule can also be considered as spinning on a plane, in a symmetric two-well potential of the form $-V_0 \cos^2 \varphi$, due to alignment of each dipole with field as well as its symmetry, where φ is the azimuthal angle of the vector joining two hydrogens ($\overrightarrow{HH}$). Under the influence of non-linear torques from its neighbors, a molecule can perform excursions from one well to the other equivalent one. The physical model which would be most appropriate for the description of rotational motions in the case of a strong field, is that one of a frustrated plane rotor. The structural changes in a water cluster experiences under the influence of a strong and uniform electric field are elongation, dipole alignment along the field direction and destruction of the tetrahedral hydrogen-bonding pattern which have as a result on the dramatic changes in dynamics as well. The external field breaks the spherical symmetry of the cluster and introduces a strong anisotropy in the system's translational and orientational modes.

Energy Transfer by THz Pulse to Water Clusters

Many water molecules form tetrahedracally coordinated structure in equilibrium. When the water clusters becomes larger than the dimer, the average number of H-bond formed by each water molecule becomes higher than one. In the fig: 6.6(a), the kinetic energy gain ΔKE due to THz pump pulse was presented for the water cluster sizes 4, 8, 32, 64 and bulk. The temperature of the water clusters and bulk was 200 K before the pump pulse was applied. As shown in fig: 6.6(a), let's us define 2 different times t_1 and t_2. t_1 is the time, when ΔKE starts increasing significantly whereas t_2 is, when ΔKE is maximum (ΔKE_{max})(fig: 6.6(a)). Water cluster with 4 molecules showed a fast change in ΔKE just few 10s of fs before the pulse reached to peak. The ΔKE for 8 water cluster followed the ΔKE for 4 water cluster, but with a delay of few tens of fs. So t_1 and t_2 for 8 water cluster are higher than the smaller cluster. It was observed from fig: 6.6(a) that t_1 and t_2 are increasing with with larger cluster sizes, but converges to the values corresponding to bulk. For sufficiently large cluster (64 water cluster), ΔKE increases similar fashion with similar t_1 and t_2. Fig: 6.6(a) presents the convergence of ΔKE_{max} from cluster to bulk water. The energy transfer by such THz pump pulse takes place within 100 fs time window. With increasing the number of molecules in the cluster, the number of molecules on the surface increases, but volume to surface ratio decreases. When the number of molecules in the cluster is sufficiently large and volume to surface ratio starts converging, the average number of H-bond in each molecule becomes constant.

In the figs: 6.6(b) and 6.6(c), partitions of ΔKE, the translational (ΔTE) and rotational (ΔRE) energy change per water monomer were presented for different water clusters and bulk water, similar to ΔKE. It is interesting to observe that ΔTE increases (fig: 6.6(b)), whereas ΔRE decreases(fig: 6.6(c)) with making the cluster size larger. Bulk water gains the largest for ΔTE whereas smallest water cluster gains maximum energy in ΔRE. For the bulk system, ΔTE and ΔTE and ΔRE were very different for smallest cluster. But this difference in ΔTE and ΔRE becomes smaller for the larger cluster. The main reason is the H-bond network among the molecules. Smaller clusters have more water molecules on the cluster surface due to which molecules require less energy to come over the potential well of H-bond. In the presence of the THz pump pulse, molecules of smaller cluster have more freedom to rotate. For the large clusters and bulk, large number of molecules are inside than on the surface. Inner molecules in the large clusters require large energy to come over the potential well of H-bond formed with neighbours that surface water molecules. So, inner molecules are not as free as the surface molecules to rotate and molecular rotations become frustrated for such waters. Here, this transition from cluster to bulk for ΔRE can

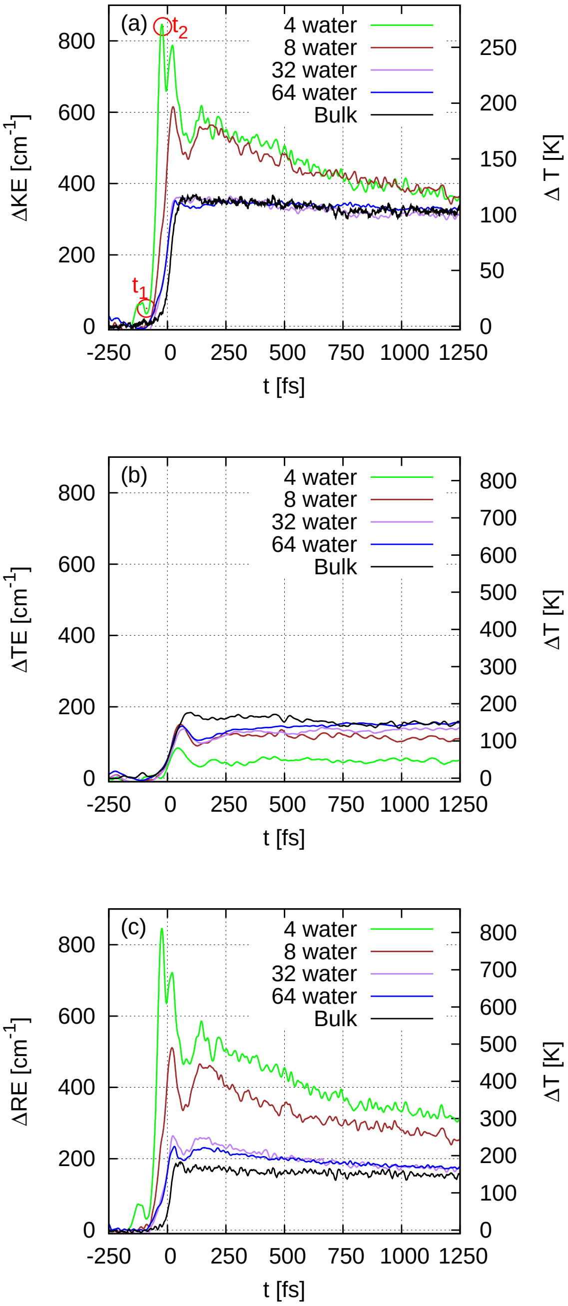

Figure 6.6: Increment in (a) kinetic energy (ΔKE) and its partitions (b) translational (ΔTE) and (c) rotational energy (ΔRE) for the water clusters of sizes 4, 8, 32 and 64 and bulk at 200 K. Red circles are showing the points t_1 and t_2 for 4 water cluster only. t_1 is the point when significant change happens in ΔKE and t_2 is the point when ΔKE is maximum.

also be termed as the transition of water behavior from free rigid rotor to frustrated rigid rotor.

Inertial Confinement in Large Clusters

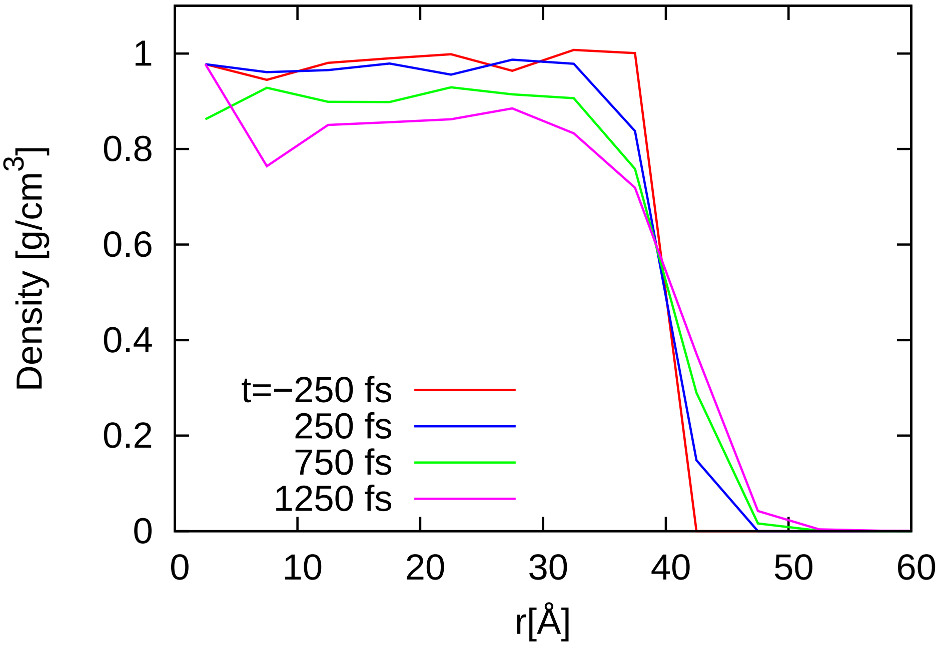

Figure 6.7: Number density as a function of radius (r) at times -250 fs, 250 fs, 750 fs and 1250 fs.

As already discussed, any significant change in liquid water due to EF occurs only when the electric field amplitude is higher than critical value E_c ($\approx$ 0.3 V/Å). So the kinetic energy changes only within a time-window of 100 fs during the pulse, when the electric field is higher than E_c. All the simulations for the bulk water were performed under microcanonical ensemble in the presence of the field with an assumption of constant volume. It was assumed that the timescale of energy transfer to the bulk water by such ultrashort pulse is too small to make any significant expansion in volume. To verify the fact of constant volume, we performed NVE simulation in the presence of the THz pulse on a spherical water cluster of radius 40Å, which contains 8843 water molecules. The spherical water cluster used for calculation was taken out from a thermally equilibrated bulk water at 300K. During the NVE simulation, this cluster was in the middle of a very big cubic box (400Å) and long-range coulombic forces due to periodic images were switched off. In the fig: 6.7, the number density (ρ_N) of water molecules were calculated with radius (r) of the sphere by binning the whole space into the spherical shells of 5 Å width. At the times -250 fs (before the pulse) and 250 fs (after the pulse), ρ_N are very similar in the inner region up to 35 Å of the cluster. Only the spherical shell at the surface could expand and molecules on the surface could fly away from cluster surface. ρ_N on the outer region ($>$ 35 Å) decreased with time but very much. While propagating this trajectory with such highly energetic water molecules after the pump, the cluster expansion was observed in the inner region ($<$ 35 Å) as well and ρ_N decreased within a ps (fig: 6.7). But this change in ρ_N was very small which accounted for only 5% of the total density within a ps after the pulse. This result is important for possible experiments performed in liquid jets or other setups where the volume is not constrained, and shows that for the short times of interest considered here, the system behaves as if confined to a fixed volume.

6.3.2 THz pulse Interaction with Bulk Water at Different Temperatures and Densities

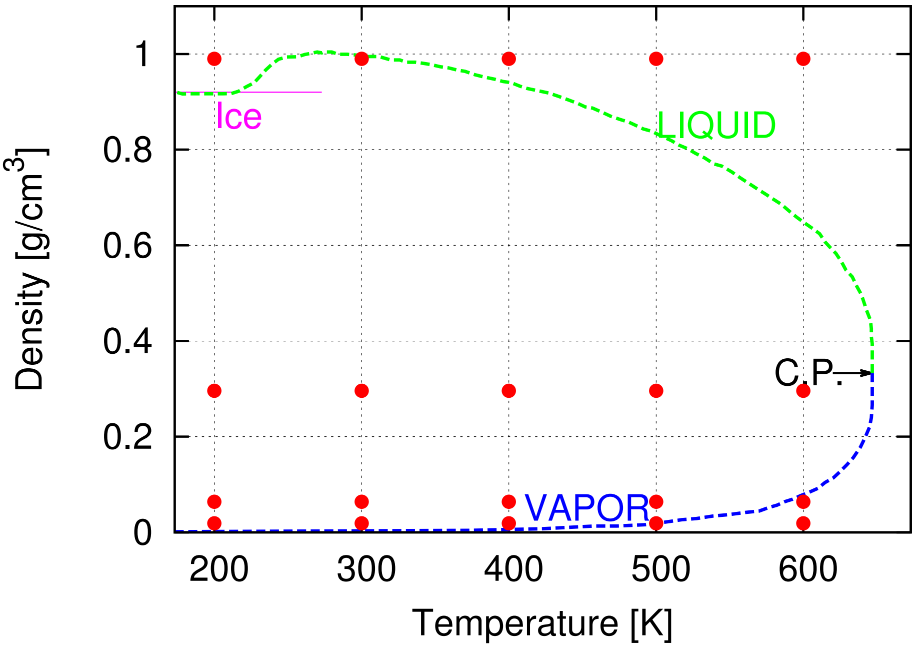

Figure 6.8: Temperature (T)-density (ρ) phase diagram of water. C.P. is the critical point. Red dots are the state of water in phase diagram, which has been used to explore the effect of THz pump.

We have discussed above how an intense, sub-cycle THz pulse interacts with an isolated water molecule and with water clusters of various sizes. Summarizing, an isolated water molecule interacts with the pulse through its permanent dipole moment thus gaining a large amount of rotational energy. Only when several water molecules are in close proximity can part of the rotational energy be transformed into relative translational energy owing to the coupling between rotational and relative translational motion of the water monomers in the cluster.

In the following, we explore the interaction of the THz pulse and the subsequent energy transfer dynamics in bulk water and different constant densities and equilibrated at different initial temperatures. Regarding initial temperature, this parameter is in principle controllable in experimental realizations and, as we will see, it has a noticeable impact on the amount of energy that can be transferred by the THz pulse. As for density, we have already shown that, in the time scales of interest and even for relatively small clusters, the inner part of the cluster remains at its initial density during the interaction with the pulse and is inertially confined by the outer shell. Therefore, simulations at the constant density (i.e. constant volume) of the liquid phase, 1 g/cm^3, are justified. Moreover, density is a well defined macroscopic parameter under real physical confinement of the interaction volume by e.g. hard walls during and after the heating-up process. Therefore, we consider various densities ranging from very low up to normal liquid density. Depending on the density and initial temperature of the confined system in equilibrium, the aggregation state of water may vary from gas phase to liquid or amorphous solid phases and the coexistence of the two. This is illustrated in the saturation diagram of pure water shown in Fig. (6.8) [225]. In the regions inside the curve vapor and liquid water coexist. Outside the curve only one phase is present, either water vapor or condensed water. The dynamics of energy transfer from the THz pulse and the subsequent energy redistribution and among rotational and translational degrees of freedom are strongly dependent of the possible aggregation states found in the diagram. Those initial conditions at which simulations have been performed are marked with a red dot in Fig. (6.8).

There are three distinctive features of the heating-up dynamics of water clusters that vary strongly as a function of the size of the cluster. *First*, for isolated water molecules and for clusters up to 8 monomers the amplitude profile of the THz pulse is imprinted in the rotational energy of the water molecules. This is indicative of none or few hydrogen bonds per monomer as compared to the bulk or to larger clusters. As a consequence, water molecules are rotationally accelerated and shortly thereafter slowed down in the presence of the THz field before they can have significant collisions with neighboring monomers. This can be observed in Figs 6.1 and 6.6c. *Second*, an equilibration between the rotational and translational components of the kinetic energy is only achieved for clusters after a certain minimum size. In our simulations we find equilibration between rotational and translational energy components for clusters of 32 or more water molecules. Smaller clusters fragment before equilibration through collisions can complete. An extreme example of this corresponds to the water dimer and tetramer. *Third*, the total kinetic energy of the clusters with four and eight monomers decreases during the first picosecond as the clusters expand, which is mirrored by the corresponding increase of potential energy as the monomers separate from each other against attractive electrostatic interactions. This effect is not observed for larger aggregates, which mostly maintain their structure.

These basic features can be recognized when letting bulk water interact with the THz

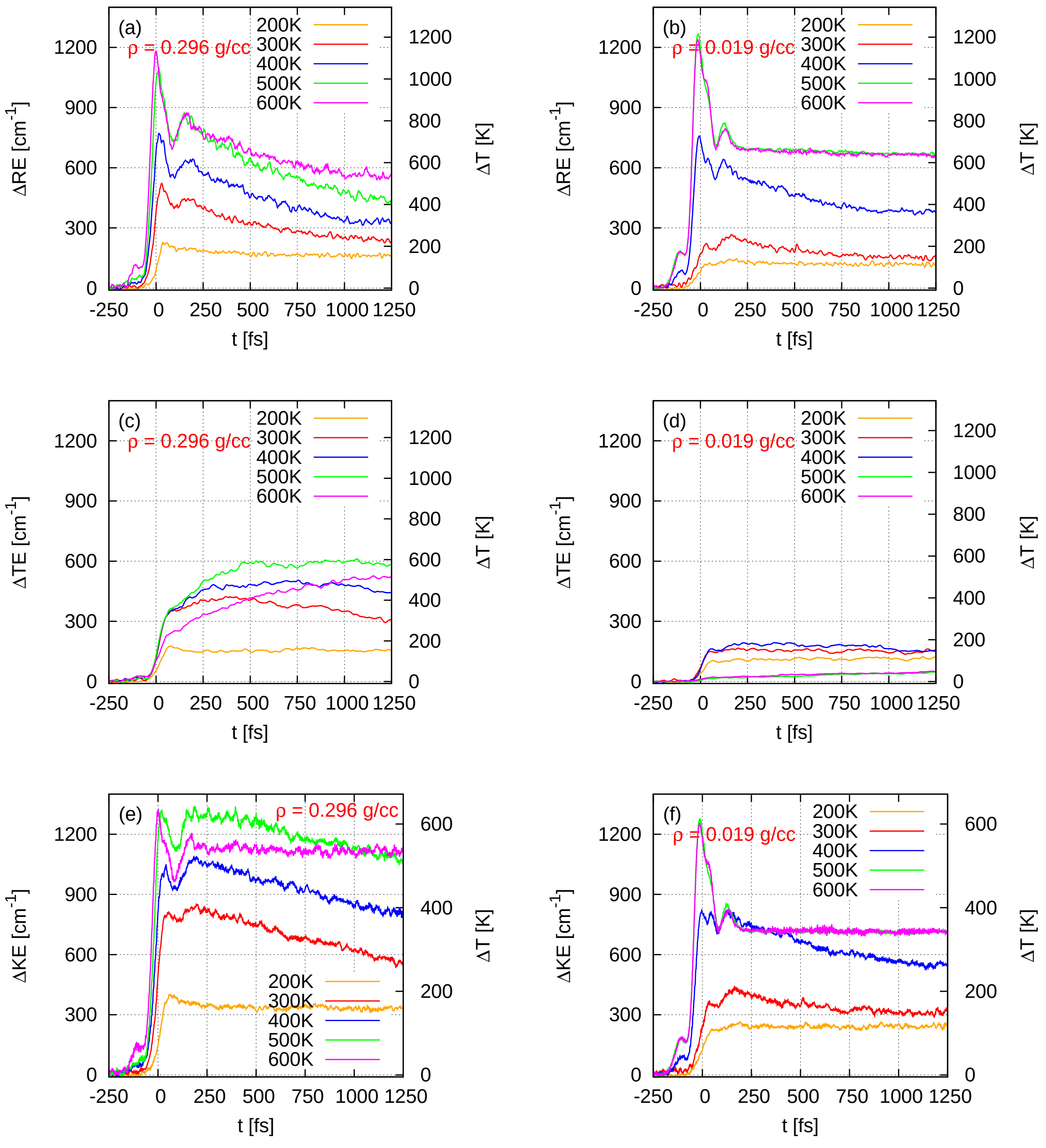

Figure 6.9: Total kinetic energy (ΔKE), translational energy (ΔTE) and rotational energy (ΔRE) per water molecule at different temperatures for the density of the system (a) 0.296 g/cm^3 and (b) 0.019 g/cm^3.

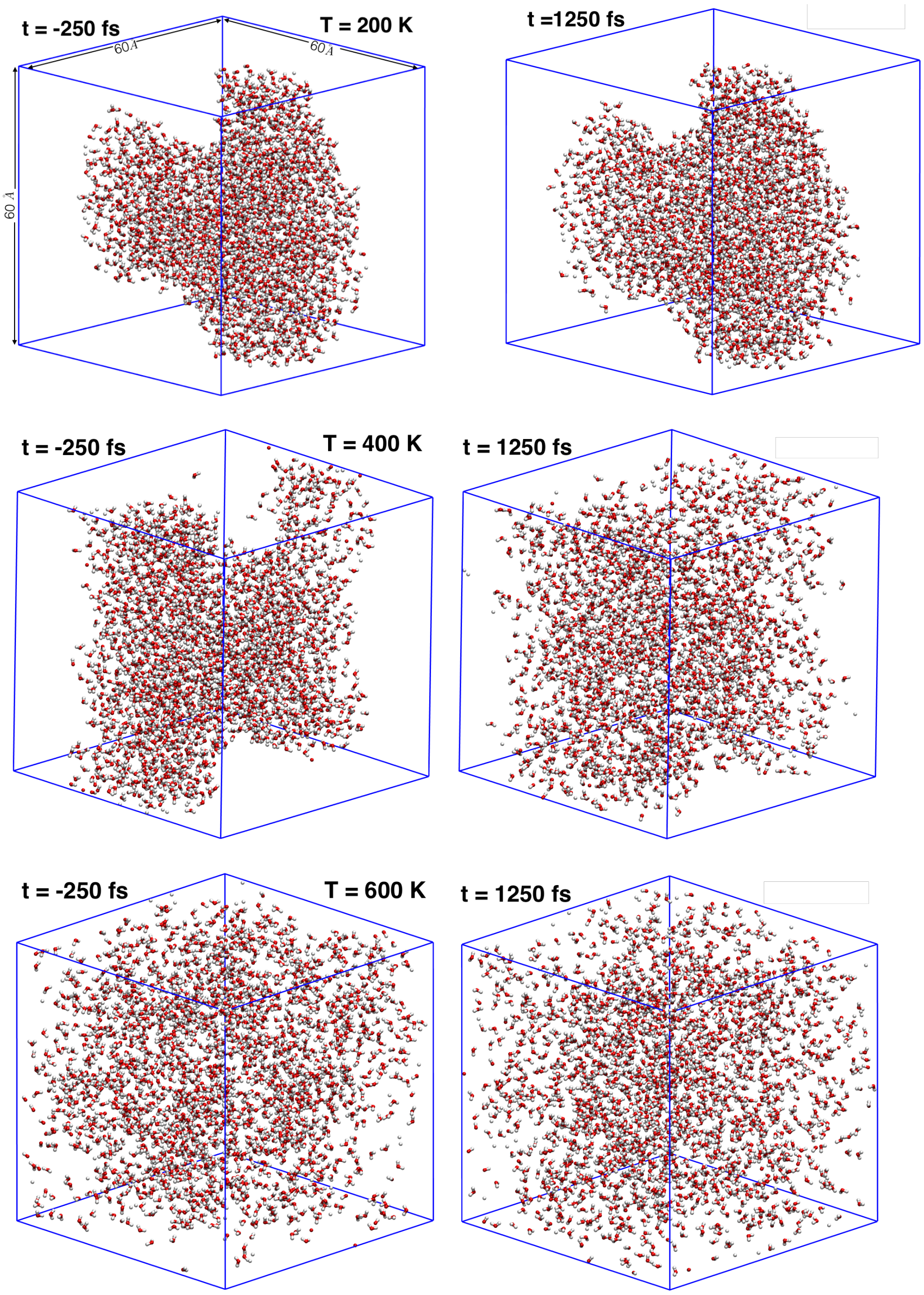

Figure 6.10: Snapshots at water systems with density 0.296 g/cm^3 and different temperatures (T= 200 K, 400 K and 600 K) before the pulse (t = -250 fs) and one ps after the pulse (t = 1250 fs).

pulse at different densities and initial temperatures. Snapshots of 2048 water molecules at a density of 0.296 g/cm^3 for different initial temperatures of 200, 400 and 600 K are shown in Figs. 6.10(a), 6.10(c) and 6.10(e) respectively. The system at 200 K corresponds essentially to a piece of amorphous ice with small internal energy. The system at 400 K is made of a large droplet of hot liquid water with several water molecules around it in the vapor state, whereas the system at 600 K is made of almost homogeneously distributed water molecules with a large mobility and collisional rate. This leads immediately to very different heating-up dynamics. The colder system gains in total less energy due to the more hindered water monomers. The equilibration between rotational and translational energy is however almost instantaneous due to the tight interactions between the monomers. As the temperature increases the amplitude profile of the THz pulse manifests more strongly in the rotational energy component because the interactions between neighboring water molecules become progressively weaker, as seen in Fig. 6.9a. For T$\leq$300 K the energy transfer between the rotational and translational components of the kinetic energy is now not instantaneous anymore (cf. Fig. 6.9b). The slowest energy transfer to translational motion occurs at 600 K as a consequence of the larger separation and weaker interactions between water molecules. A decrease of the total kinetic energy shortly after the pump pulse occurs for systems initially between 300 and 500 K due to substantial evaporation of monomers from the outer shells of the liquid portion. This can be seen by comparing the snapshots in Figs. 6.10(d) and 6.10(f).

As compared to the previous examples, a reduced density of 0.019 g/cm^3 leads to differences mostly for the high temperature cases. At T= 500 K and T=600 K the water molecules are homogeneously distributed across the available volume and at a large average distance from one another. This results in dynamics of the rotational degrees of freedom similar to those of isolated monomers and characterized by a slow rate of energy transfer to translational degrees of freedom due to infrequent collisions. This can be seen by comparing the increase of translational energy shown in Figs. 6.9c and 6.9d. At this density, only the colder systems at T= 200 K and T= 300 K achieve equilibration between rotational and translational degrees of freedom because most of the water molecules are condensed in ice and liquid droplets, as seen in Figs. 6.10(a) and 6.10(b). This leads to coupled hindered rotational and translational motion in the condensed phase and the corresponding fast energy transfer.

At temperatures T=500 K and T=600 K the amount and rate of energy transfer from the THz pulse to rotational motion is relatively independent of the density of the system, as can be seen in Fig. 6.11b. Independently of the density, the high temperatures result in weak hydrogen bonding and the rotational degrees of readily respond to the THz pulse. However, the collisional energy transfer from the rotational to the translational degrees of freedom at these high temperatures is strongly dependent on the density of the system, as illustrated in Fig. 6.11d. At low densities almost no collisions occur whereas at 1 g/cm^3 the rotational and translational temperatures are equilibrated within 1 ps.

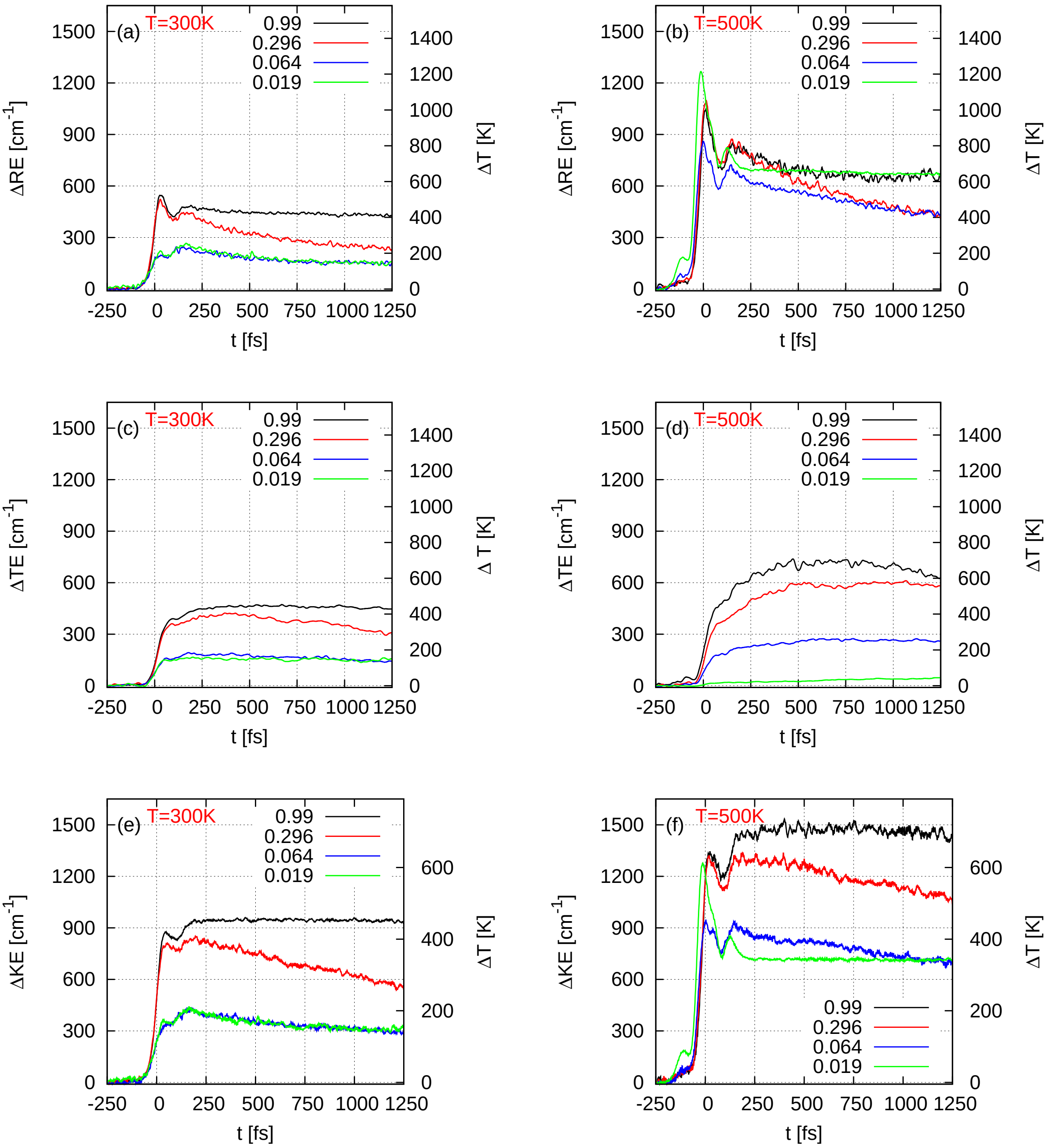

Figure 6.11: Total kinetic energy (ΔKE), translational energy (ΔTE) and rotational energy (ΔRE) per water molecule at different densities for initial temperatures (a) 300 K and (b) 500 K of the system.

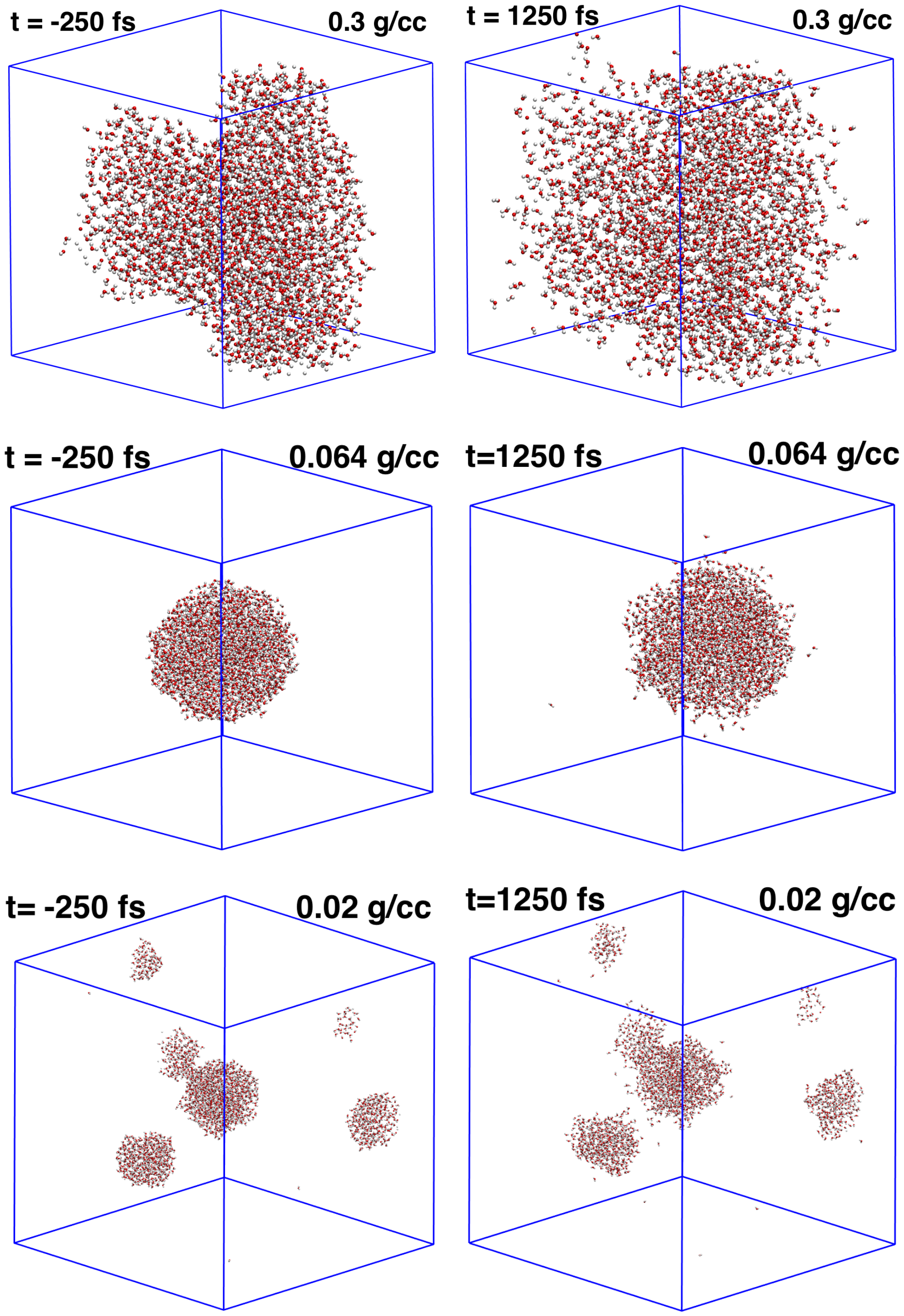

Figure 6.12: Snapshots at water systems with temperature 300 K and different densities (0.296 g/cm^3, 0.064 g/cm^3 and 0.019 g/cm^3) before the pulse (t = -250 fs) and after the pulse (t = 1250 fs).

6.4 Conclusion

We have discussed in detail the mechanisms by which a highly intense (5×10^{12}W/cm^2) and ultrashort (500 fs) THz pulse couples to clusters of water molecules and to bulk water and transfers a large amount of energy to the system. The fundamental coupling mechanism between the THz pulse and the water molecules is through the permanent dipole moment of those with the electric field component of the pulse. Therefore, the THz pulse transfers energy only to rotational motion of isolated water molecules and translational motion of the center of mass remains unaffected due to their electrical neutrality. For the clusters with two or more molecules, coupling between hindered rotations and translations exist and the translations also gain energy during and after interaction with the THz pulse. Inspection of the potential energy curve (PEC) of the OOH angle of the water dimer in the presence of a static electric field shows small changes for a EF amplitude up to 0.087 V/Å. Beyond this field strength, a small variation in the EF will induce a significantly large change in the PEC. At an electric field amplitude of 0.614 V/Å, the PEC shows that the EF can break the hydrogen bond in the water dimer and bring the permanent dipole moments of the two monomers to orient with the polarization axis of the EF.

We studied the interaction of confined water at well defined initial temperature and different densities. Even relatively small clusters lead to inertial confinement of the water molecules below the most external shells, which justifies investigations of bulk water at constant density of 1 g/cm^3. We also investigated lower densities, which can result from physical confinement either by macroscopic physical walls or even in nanostructures. High temperatures of 500 and 600 K lead to a rotational dynamics similar to isolated water molecules. Lower temperatures, in which the interactions between water monomers are stronger, lead to a smaller energy transfer from the THz pulse. The density of the system plays a key role in the collisional energy transfer between rotational and translational motion. For large temperatures, a large density leads to a high collision rate and quick equilibration whereas a small density prevents collisions and no equilibration can occur. For small temperatures, a large fraction of the system is in a condensed state and equilibration between rotational and translational motion occurs almost instantaneously.

These results might pave the way towards studies of thermally activated chemical and biological processes in which the water medium is used as a channel to deliver the energy of a THz pump pulse to the molecules of interest. The trends identified in terms of temperature and density of the system might be used to design strategies in which the heating-up rate of substances dissolved in water is controlled by such thermodynamic parameters.

Chapter 7

Effect of Pulse Parameters on the Energy Transfer Dynamics to Water

7.1 Introduction

Terahertz (THz) region of electromagnetic radiation spectrum is basically defined by the frequency range from 0.1 THz to 10 THz (10^{12} cycles per second). THz radiation lies in between infrared and microwave radiation. But this is resistant to the pulse generation techniques commonly employed in these well-established neighboring spectral regions. THz spectroscopy is used by chemists and astronomers for the spectral characterization of the rotational, vibrational and thermal-emission lines of atoms and molecules [69] for a long time. In recent years, there has been a revolution in the capability of lasers operating in THz regime [78, 108, 226], which has lead to many interesting applications on solid materials [227] and up to gas [228] phase molecules. Even in biological processes, time-domain THz (TD-THz) instrumentation is crucial for the study of protein dynamics in water [106]. The main reason is that biomolecules solvated in water unfold within mili or microseconds and, therefore the terahertz absorption properties of the protein-liquid mixture change on the same time scale. Advances in THz research develop many measurement techniques like THz time-domain spectroscopy (THz-TDS), THz imaging, and high-power THz generation by means of nonlinear effects. With such development, THz radiation is used in variety of applications including semiconductor and high-temperature superconductor characterization, tomographic imaging, label-free genetic analysis, cellular level imaging, security and chemical biological sensing and many more.

THz-emission power is shown as a function of frequency in the fig: 7.1 [108]. Fig: 7.1 presents the different techniques, which are used to generate the THz radiation of various frequencies and peak power. There are basically three kind of mechanism to generate the THz sources: 1) Optical THz generation, 2) THz-Quantum Cascade Lasers (THz-QCL) and 3) Solid-state electronic devices. The developments in THz sources by these mechanism

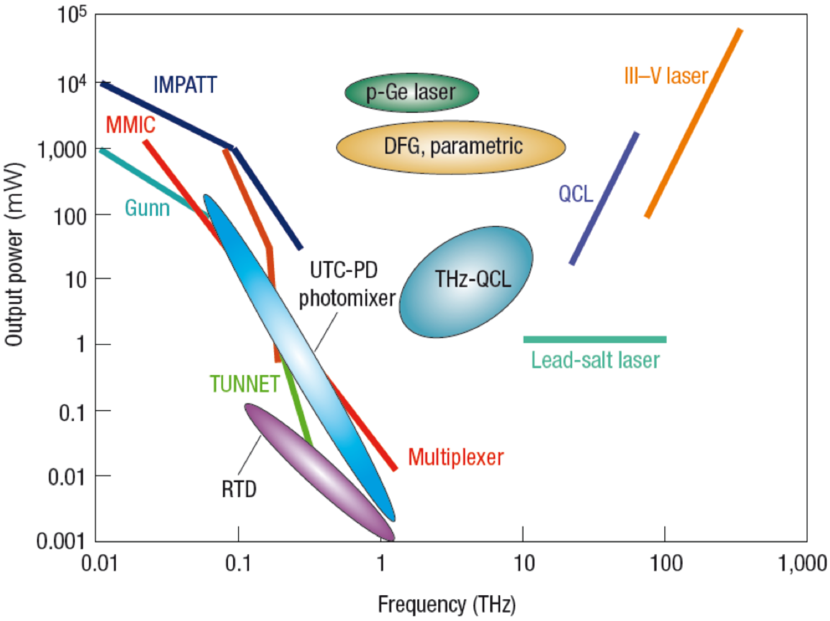

Figure 7.1: THz-emission power as a function of frequency. Solid lines presents the conventional THz sources; IMPATT diode means impact ionization avalanche transit-time diode, MMIC means microwave monolithic integrated circuit, TUNNET means tunnel injection transit time and the multiplexer is an SBD frequency multiplier. Ovals denote recent THz sources. The values of the last two are indicated by peak power; others are by c.w. power, taken from ref: [108]

have been discussed in chapter 1.

As discussed in chapter: 3, librational modes of liquid water is located between 400 to 1000 cm^{-1} (12 - 30 THz) in the far-infrared frequency region. Librations are intermolecular modes which involve more than one water molecule and are affected by the strength of H-bond. However, there is not much known about the detailed intermolecular dynamics, for example the frequency modulations of the librations as well as hindered translation motions and the energy relaxation processes between librations to other modes. There have been many studies to understand the energy relaxations among librations. It has been found that the ultrafast loss of the correlation of the librations happens on the time scale of approximately 110 fs. The energy relaxation from the librations to other low frequency motions takes place with the time-scale of $\approx$ 180 fs [67].

In the chapters: 3 and 4, we presented the results for the pumping with THz pulses of intensity 5×10^{12} W/cm^2 and central frequency 3 THz ($100cm^{-1}$). In this chapter, we explored the response of liquid water to pump pulses of different THz frequencies having different peak power per unit area. The study with THz pulses of different intensities will basically help the experimentalists to design a possible experiment to achieve significantly larger temperature-jump (T-jump). We studied the effect of peak field amplitude to break the hydrogen bond network and the energy of the pump pulse to generate the T-jump in water. The liquid water also has intermolecular modes like librations in the far-infrared (far-IR) region. It is interesting to understand the response of water to the pump pulse of 20 THz. We analyzed the energy gain in different modes of water with such pump pulse. The laser sources to generate the pulses in the far-IR region are easily available for producing high intensity pulses [229]. Similar to chapter: 3, the energy transfer by the pump pulse of 20 THz to liquid water at 300 K with density 1.0 g/cm^3 was analyzed to compare the energy transfer by THz pump pulse. Similar to chapter: 6, the role of the H-bond which depends on the phase of the system, was also analyzed for 20 THz pump pulse. This chapter presents the comparison between the energy transfer mechanism for the pump pulses of 3 THz and 20 THz.

7.2 Method

It is shown in chapter: 5, that force-field simulations are not able to produce the similar results as *ab-initio* molecular dynamics (AIMD) quantitatively. However qualitatively, FFMD presents the similar mechanism to transfer the energy to liquid water as by AIMD. Here, TIP4P/2005f water force field was used during the simulations. A cubic box of 2048 water molecules with density 1 g/cc was propagated for NVT molecular dynamics simulations to thermalize the system at 300 K. The thermalized system was then propagated under microcanonical ensemble (NVE) in the presence of the electric field. The THz pulses were implemented during the simulations in the form of time-dependent electric field. The pulse profile, used during the simulation was

$$\mathbf{E(t)} = \mathbf{E_0} \exp(-\frac{(t-t_0)^2}{2\sigma^2}) \cos(\omega t + 2\pi\phi) \tag{7.1}$$

where $\mathbf{E}_0$ $(= |\mathbf{E}_0|\hat{u})$ is the peak field amplitude in the polarization direction $(\hat{u})$. Here, $\hat{u}$ is $\hat{z}$-axis in the Cartesian system. t_0 is the pulse center and σ corresponds to the width of the pulse. σ = FWHM/2.3548, where FWHM is the full width at half maximum of the pulse. ω is the central frequency and ϕ is the phase of the pulse. The intensity (I) of the pulse which is the peak power per unit area, is defined by

$$I = \mathbf{E_0}^2 \times 3.50944 \times 10^{16} \tag{7.2}$$

where I has the unit W/cm^2 and E$_0$ is in a.u.. Different pulse profiles were used during the NVE simulations by varing the E_0 corresponding to different intensity, σ and ω. The simulations in presence of the 3 THz pump pulse were performed with using shake algorithm.

The simulations were also performed in presence of the pump pulse with 667 cm^{-1} (20 THz), 1600 cm^{-1} and 3500 cm^{-1} to compare the temperature jump by different methods. The pump pulses of central frequencies 1600 cm^{-1} and 3500 cm^{-1} resonate the internal bending and OH stretching mode of water. So, the NVE simulations in presence of the pulses of 1600 cm^{-1} and 3500 cm^{-1} were performed without using shake algorithms . To understand the response of 20 THz pulse on liquid water, the water clusters of monomers, dimers and octamers were also propagated in presence of the pulse under microcanonical ensemble. The energy analysis for these water clusters was the ensemble average over 300 trajectories started with different initial configurations. These initial configurations were collected from a long NVT trajectory thermally equilibriated at 200 K. A NVE simulation in presence of 20 THz pump pulse was also performed on liquid water with 2048 molecules in a cubic box which was thermally equilibriated at the density of 1 g/cm^3 and 300 K temperature. To analyze the effect of density and temperature for 20 THz pump, we equilibriated the box of 2048 water molecules with different box sizes and temperatures with canonical (NVT) ensemble. We studied the water with density 0.3 g/cm^3, 0.064 g/cm^3 and 0.02 g/cm^3 at temperatures 200 K, 400 K, 500 K and 600 K. All the simulations in presence of 20 THz pump pulse were performed with shake algorithm to freeze the internal vibrations. The reason of using the shake has been discussed in detail in chapter: 5.

7.3 Results

It was already discussed in chapter: 6 that water molecules are connected through the strong H-bond network in the liquid phase and this H-bond network can be broken by electric field only when the field amplitude is higher than a certain minimum value. The strength of H-bond depends on the temperature and density of bulk water. Here, we investigated the effect of intensity and photon energy of the pulse on the transfer to liquid water. Later, we also presented the comparison in energy transfer mechanism by 3 THz and 20 THz pump pulses.

The peak intensity of pump pulse depends on how tightly the source beam was focused during the generation. If the source beam with total energy E is focused in the area A, the peak intensity of the pulse is

$$I = \frac{E}{t \cdot A} \tag{7.3}$$

where t is the pulse duration. So, the peak power of pump the pulse can be modified by varing the total energy or fluence (E) of the pulse as well as the pulse duration (t) considering the same focusing area.

7.3.1 THz Pump Pulses of Same Pulse Duration but Different Fluences

In the fig: 7.2(b), the total kinetic energy transfer to each water monomer was presented for the THz pulse of central frequency 100 cm^{-1} ($\approx$ 3 THz), but with different peak powers per

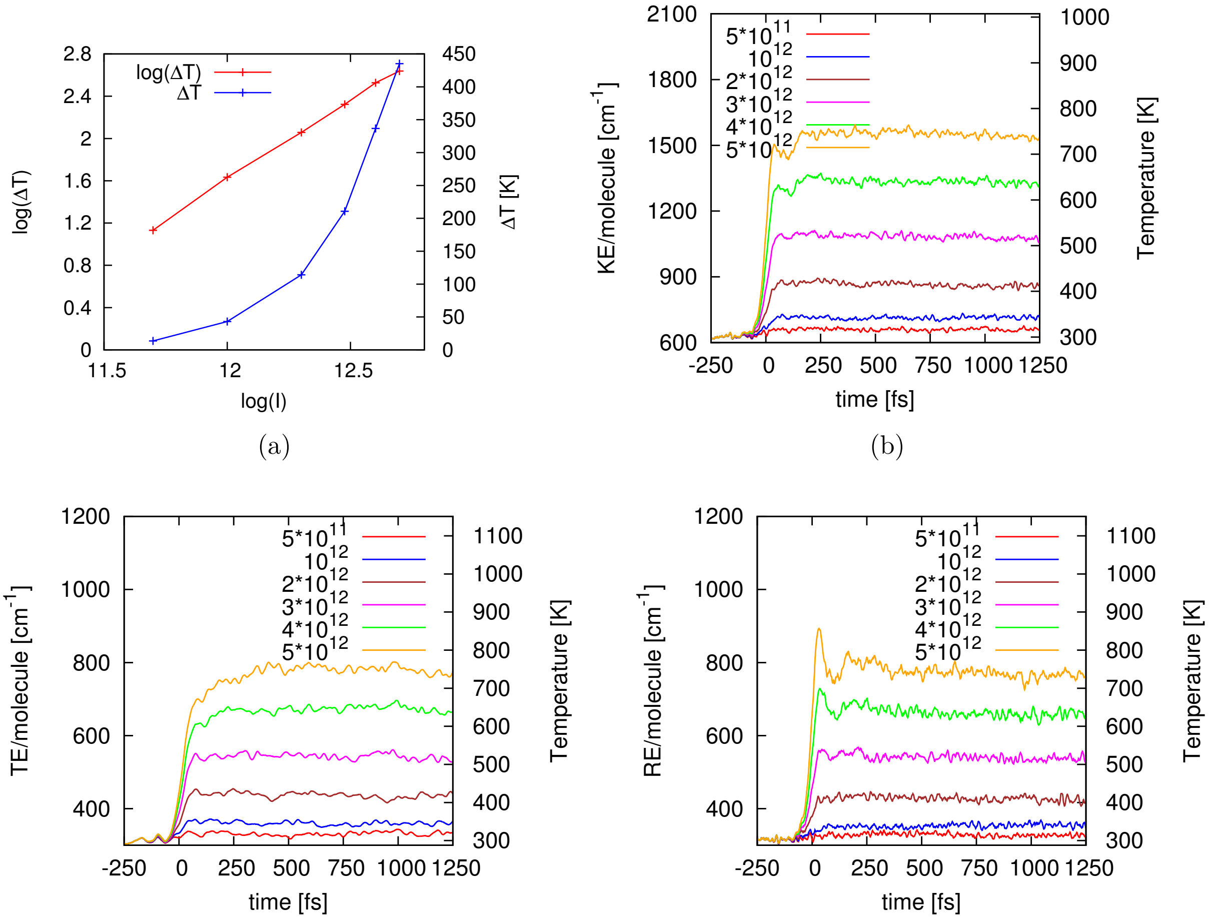

(a) (b)

(c) (d)

Figure 7.2: (a) Kinetic Temperature change (ΔT) in liquid water for THz pump pulse of different intensities (log(I)) as well as log(I) with log(ΔT). (b) Total kinetic energy (KE), (c) translational energy (TE) and (d) rotational energy (RE) of each water monomer due to pump pulse of different intensity. The center of pulse is at 0 fs. Intensity is shown in W/cm^2 unit.

unit area of 5×10^{11} W/cm^2, 10^{12} W/cm^2, 2×10^{12} W/cm^2, 3×10^{12} W/cm^2, 4×10^{12} W/cm^2 and 5×10^{12} W/cm^2. All the pulses have the same pulse duration with $\sigma = 84.43$ fs but have different fluence. So, the pulse with higher peak power carries higher pulse energy in the same time duration. Therefore, it is interesting to observe the response of water to the peak fluence to break the H-bond network. It is interesting to observe that the liquid water doesn't gain energy with the pump of THz pulse with intensity 5×10^{11} W/cm^2. Pulse with intensity 5×10^{11} W/cm^2 is not able to break the H-bond network among the molecules and the water system remains almost unaffected in the presence of such low intensity pulse.

The pulse with intensity 5×10^{11} W/cm^2 corresponds to the electric field amplitude 0.194 V/Å. The pulse with 10^{12} W/cm^2 has the EF amplitude 0.274 V/Å, which is above the threshold EF (E_C) to break the H-bond among the molecules. Therefore, the pulse with intensity 10^{12} W/cm^2 or higher is able to break the H-bond network among the molecules (fig: 7.2(b)). The kinetic temperature jump (ΔT) of water due to the pump is related to pulse intensity (I) by

$$\Delta T = C \cdot I^P$$
$$log(\Delta T) = P \cdot log(I).$$

where P is the slope of the line joining to $log(I)$ vs $log(\Delta T)$ and C is a constant. The fig: 7.2(a) shows that $log(I)$ vs $log(\Delta T)$ is a linear curve with slope 1.507. Therefore, increment in kinetic temperature (as well as total kinetic energy) with peak power of the pulse seems a non-linear process. This is due to the fact that once the H-bond is broken among the molecules, the rest of the energy directly contributes to the hindered rotations of the molecules.

The similar behaviour can also be observed from the partitions of total kinetic energy: translation energy (TE)(fig: 7.2(c)) and rotational energy (RE)(fig: 7.2(d)) of each water monomer. Even if THz pulse interacts with the permanent dipole moment of water, the water dipole is not able to rotate in the presence of the pulse with intensity 5×10^{11} W/cm^2. It is interesting to observe that rotations and translations gain energy in almost same timescale for all intensities. It shows that once molecules have sufficient energy to break the H-bond and rotate, they start pushing each other to go away and rotations become hindered. Such hindered rotations lead to movement in center of mass of molecules and so energy gain in translations.

7.3.2 THz Pump Pulses of Different Frequencies but Same Fluence

Here, we studied the pumping with THz pulses of different intensities and frequencies but carrying the same fluence. All the pulses are single cycle pulse. The EF intensity profile (square of the envelop) of each pulse has the same area under the curve. In fig: 7.3(a), the shape of different pulses is presented. The pulse with intensity (I) 10^{12} W/cm^2 has the central frequency (ω) 0.5 THz, others with I = 2×10^{12} W/cm^2 belongs to ω = 1.5 THz, I = 3×10^{12} W/cm^2 belongs to ω = 2 THz and I = 5×10^{12} W/cm^2 belongs to ω = 3 THz (fig: 7.3(a)). All the pulses are centered at 0 fs. T-jump due to such pulses is analyzed in fig: 7.3(b). It is observed that the pulse with highest intensity has a very sudden increase in temperature than the other lower intense pulses. As the pulse intensity decreases, the energy transfer to water decreases and T-jump also decreases. However in all cases, the T-jump happens only once the pulse field amplitude has crossed threshold field required to break the H-bond as discussed in chapter:5. The THz pulses with intensities

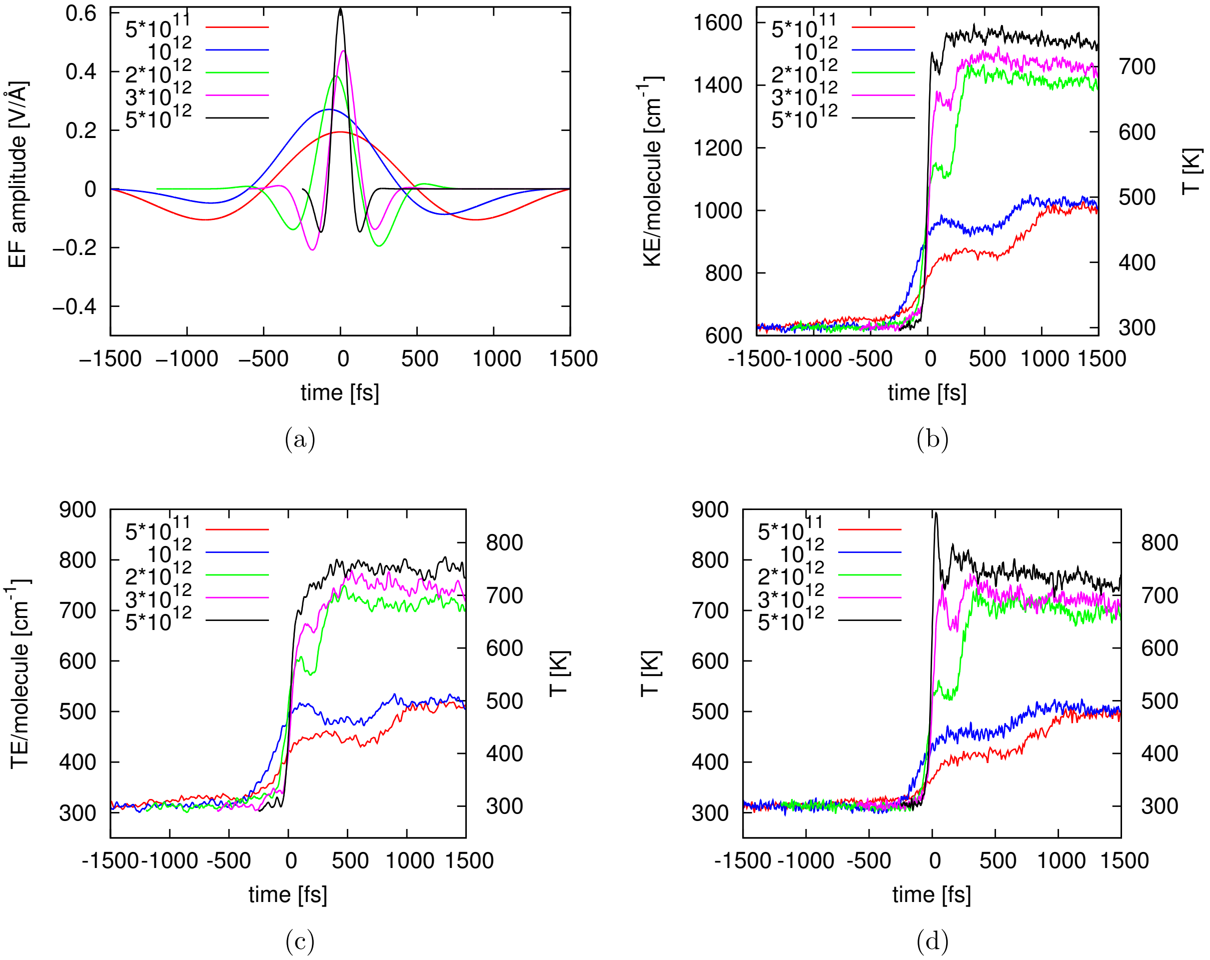

(a) (b)

(c) (d)

Figure 7.3: (a) The shape of the THz pump pulse of different central frequencies (ω) and different intensities but carrying same energy. Red curve presents the pulse of 0.5 THz, blue curve the 1.5 THz pulse, green the 2 THz pulse, and black the 3 THz pulse. (b) Total kinetic energy (KE), (c) translational energy (TE) and (d) rotational energy (RE) of each water monomer due to pump pulse. Intensity is presented in W/cm^2 unit.

$2{\times}10^{12}$ and higher provide roughly similar amount of temperature jump to liquid water. Basically, if maximum field amplitude of the pulse (E$_{max}$) is higher than E$_C$ (E$_{max}$ > E$_C$), the temperature jump is very similar for same fluence. However, the temperature jump (ΔT) in liquid water by the pulse with intensity 10^{12} W/cm^{12} is almost half of what it gains because of other pulse. It is interesting to observe that as the pulse length increases, the energy transfer to liquid water becomes slower. The temperature starts increasing at the very similar timescale for the pulse with intensity $2{\times}10^{12}$ W/cm^2 and higher. The main difference becomes the time-scale over which temperature jump happens. It is longer

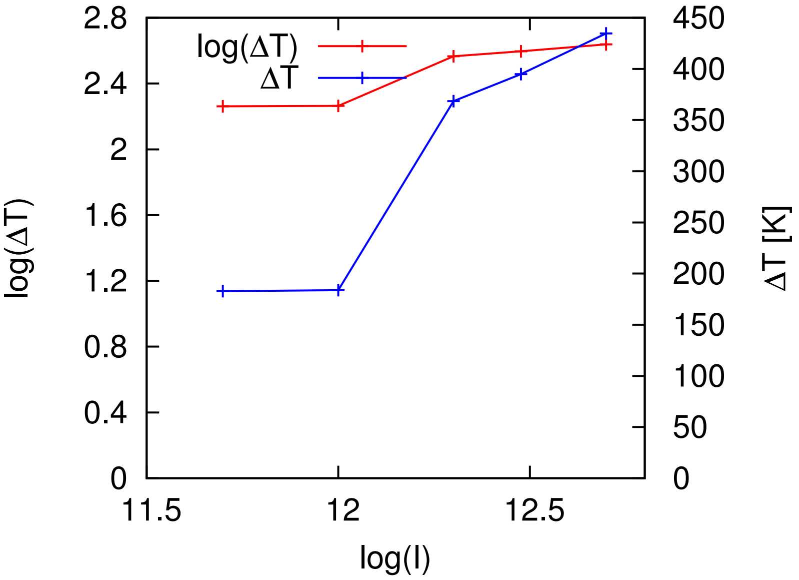

Figure 7.4: log(ΔT) with log(I) for the relation $\Delta T = I^P$ where ΔT is temperature jump 1.5 ps after the peak of the pump pulse and I is the peak power per unit area of the pulse.

for the pulse with lower intensity. In the fig: 7.4, the log(Δ) vs log(I) is presented. The slope (P) of the the curve log(Δ) vs log(I) seems certainly less than 1 for $log(\Delta) = Plog(I)$ or $\Delta T = I^P$.

The fig: 7.3(c) and 7.3(d) present the kinetic temperature of translational and rotational motions of each water monomer. The temperature of rotational motions starts increasing at similar times. Similar behaviour is also observed for translational motions. It is worth noting that intensity of THz pulse plays a key role in breaking the H-bond, even if the energy carried by the pulse is large enough. Once the H-bond among molecules is broken by the pulse, the energy transfer to water monomer depends on portion of the pump pulse, which has the field amplitude higher than E_C. So it was explored that the pulse with intensity 2×10^{12} W/cm^2 or higher is able to transfer large amount of energy to the water. Basically, both the intensity and energy of a THz pulse play a key role in breaking the H-bond and transferring the energy.

7.3.3 Effect of Pulse Frequency

In the above analysis, the response of liquid water to sub-cycle THz pulses of different intensities at constant duration and at constant fluence was discussed. Such THz pulses interact with the permanent dipole moment of water. However, to generate the highly THz pulse in the frequency range between of 0.3 to 10 THz has been a tedious task and is still subject to explore. It is also been shown that a THz pulse with intensity beyond a limit

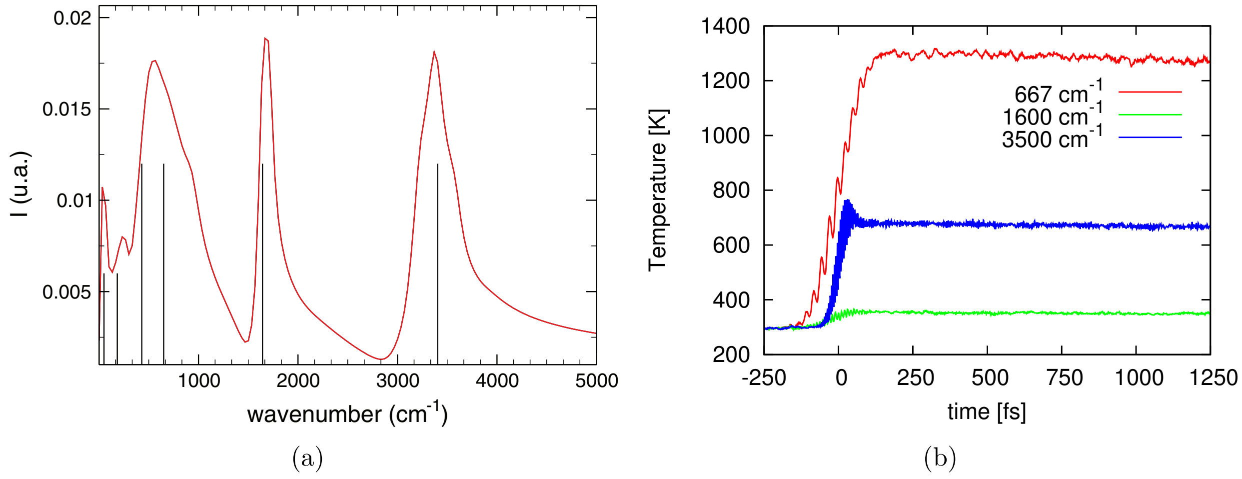

(a)

(b)

Figure 7.5: (a) Spectrum of densities of state of liquid water for TIP4P/2005f water model in the ref: [162]. (b) Kinetic temperature of liquid water due to different pump pulse.

doesn't seem feasible to generate with the existing mechanism [230, 231]. The pulses in the higher frequency range starts exciting different intramolecular modes of water molecules. In the fig: 7.5(a), the power spectrum (spectral density) of liquid water is presented for TIP4P/2005f force-field from the ref: [162]. The water shows basically 3 different peaks in the frequency range higher than 300 cm^{-1}. The peak around 600 cm^{-1} corresponds to librations [232]. Another peak in the power spectrum is at 1670 cm^{-1} corresponding to H-O-H bending modes. O-H stretching modes belongs to peak at 3400 cm^{-1}. It becomes interesting to explore the response of liquid water if these molecular vibrational modes are directly excited. We performed the FFMD simulations using the pulse with frequency 667 cm^{-1} (20 THz), 1600 cm^{-1} (48 THz) and 3500 cm^{-1} (105 THz). All pulses have the peak power per unit area of 5×10^{12} W/cm^2 which corresponds to peak field amplitude of 0.613 V/Å with width σ of 84.33 fs. The bulk water of 2048 molecules used for the simulation was equilibriated at temperature 300 K at a density of 1.0 g/cm^3. It was observed that the pulse with wavenumber 667 cm^{-1} is able to transfer significantly large amount of energy to the liquid water. The kinetic temperature of the system jumps from 300 K to 1300 K with this pulse. In contrast, the system is almost insensitive to the pulse of 1600 cm^{-1}. It seems that it is not feasible to resonate the H-O-H bending of the water molecule. The most common method to generate the T-jump in water is to excite the O-H stretching. The pulse at 3500 cm^{-1} is also able to create the T-jump from 300 K to 650 K by targetting the O-H vibrations. The energy transfer by such IR pump pulse to different water modes was also discussed in detail in chapter: 5. With such pump pulse, the intermolecular modes i.e. translation and rotations remain colder than intramolecular vibrations which is basically O-H vibrations. Here, I will focus on the possibility of using a pump pulse with central frequency 20 THz, which is producible with high intensity and ultrashort timescale.

7.3.4 Far-Infrared Pumping on Liquid Water

It is interesting to observe in fig: 7.5(b) that THz pulse of central frequency 20 THz (667 cm^{-1}) is also able to transfer a large amount of energy. None of internal vibrations (bending or stretching) absorb this frequency. However, the librations of liquid water have absorption in this frequency range. The librations are intermolecular modes of water which include hindered rotations and translations of the water monomer.

Pump Pulse of 20 THz on Water Clusters

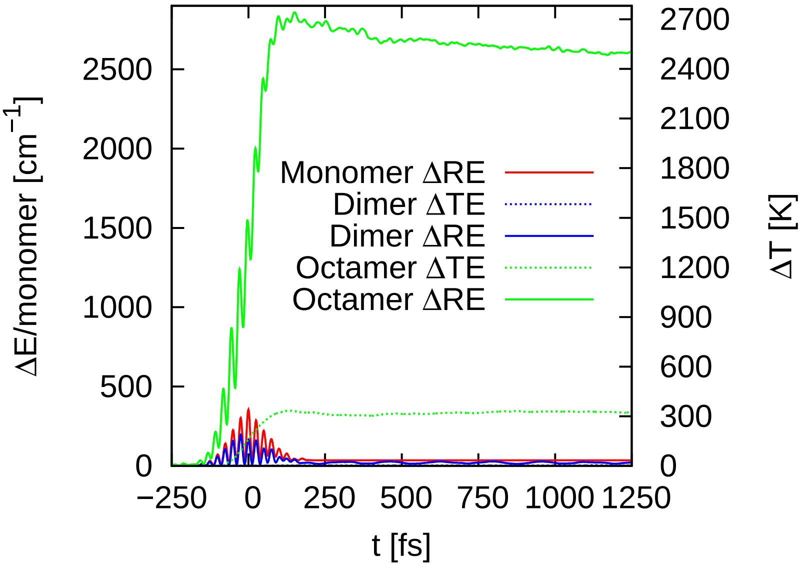

Figure 7.6: The gain in translational energy (ΔTE) and rotational energy (ΔRE) due to pump pulse of 20 THz in water monomer, dimer and octamer. ΔTE is presented with dotted lines and ΔRE is solid lines.

The translational energy gain (ΔTE) and rotational energy gain (ΔRE) by 20 THz pump pulse in different water clusters (monomer, dimer and octamer) are shown in the fig: 7.6. ΔTE is considered zero for the isolated water because water is an neutral molecule. The isolated water molecule gain energy in rotations during the pulse but after the pulse, the rotational energy gain is negligibly small. Such pump pulse resonates the rotations directly which are related to librations. The structure of the pulse amplitude can be observed in the rotational energy transfer to the water monomer. Similar behaviour was also observed for the water dimer. There is no gain in translational energy as well. Whereas in the case of 3 THz pump pulse as discussed in chapter: 6, water monomer gains maximum energy in rotations during the pulse and also after the pulse. Even water monomers gain significantly large energy in rotations as well as in translations in water dimer with pump pulse of 3 THz. In the case of water cluster of 8 molecules, each water monomer gains significantly large amount of energy to the rotations once the pulse crosses the threshold field amplitude and translational energy also increases during the pulse (fig: 7.6). In the case of 3 THz pump, isolated water gains maximum energy and the energy decreases for the larger clusters. Such behavior of energy transfer to water clusters by 20 THz pump pulse is opposite to energy transfer by 3 THz as discussed in chapter: 6. The reason is that 3 THz pump pulse interacts to the permanent dipole moment of water whereas, 20 THz pump pulse resonates the librations directly. Libration motions become significant for the larger clusters than the isolated or smaller clusters.

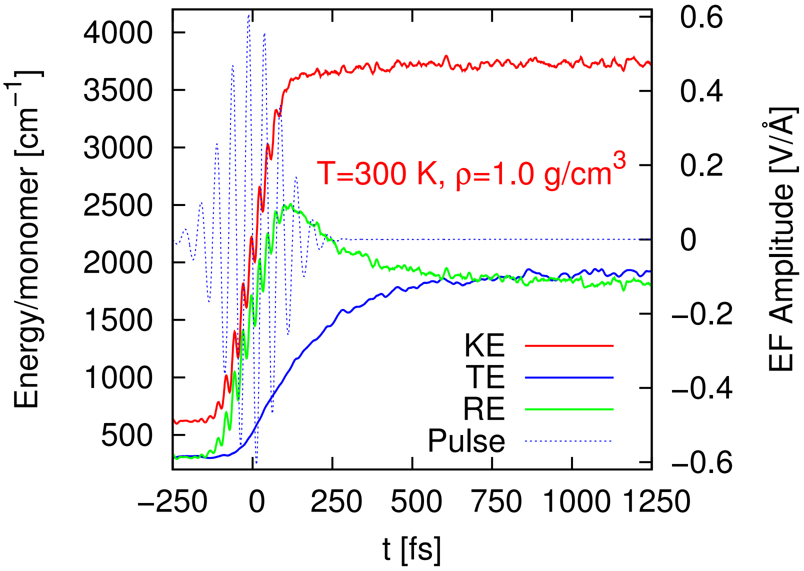

Figure 7.7: Total Kinetic energy (KE) along with its partitions translational (TE) and rotational energy (RE) of each water monomer due to the pump pulse of 20 THz central frequency and 5×10^{12} W/cm^2 intensity on liquid water of 1.0 g/cm^3 at room temperature. The pulse profile is also shown in blue.

Energy Transfer to Bulk Water at 300 K and 1 g/cm^3

To analyze the energy transfer by a 20 THz pulse, the total kinetic energy (KE) along with translational (TE) and rotational energies (RE) are shown in figure: 7.7. Each water monomer gains approx. 3000 cm^{-1} of KE which corresponds to a temperature jump of 1250 K. This energy gain is higher compared to energy gain with 3 THz pulse as presented in chapter 5. During the pulse, KE increases only when the pulse crosses a threshold field amplitude. In the fig: 7.7, the pulse profile is superimposed on KE. It can be seen that fluctuations of the field amplitude of the pulse also causes the fluctuations in KE. The delay in increment in KE again is due to the strength of H-bond network of water which can be modified only when the EF amplitude is higher than the critical field ($E < E_C$) as discussed in detail in chapter: 6. During the pulse, the main contribution in KE is mainly due to the energy gain in RE. In contrast to 3 THz pulse where RE and TE increases on a very similar timescale, 20 THz pulse transfers the energy directly to rotations. TE follows RE slowly with a time-delay of 150 fs. Significant increment in TE happens only after the pulse crosses its peak amplitude and keep on increasing after the pulse as well. Once the pulse amplitude becomes lower than a certain value after the pulse, the librations are no more affected by the field variation. Now, the RE decreases whereas TE increases. In the case of 3 THz pulse (chapter: 5), TE and RE increases within same timescale and the most of the energy gain happens within 100 fs time window which include the peak of the pulse. So, 3 THz is transferring the energy to water without being mode specific. Within a ps after the pump, the rotational energy relaxed and transferred to translational modes. If the energy transfer or other processes occurring in water are supposed to be studied in ps timescale 20 THz pump techniques can turn out to be useful. Due to force-field limitations as discussed in chapter: 5, the shake algorithm was used during the simulation and the response of internal vibrations can not be studied with such pulses.

Effect of Temperature and Density

The density and temperature affects the H-bond strength significantly. In chapter: 6, the effect of initial temperature and density on energy transfer to liquid water was analyzed for pump pulse of 3 THz. THz pulse with 20 THz transfers the energy to librations during the pulse in contrast to 3 THz, which transfers the energy to water through dipole interaction. It becomes interesting to explore the response of liquid water of different densities and temperatures with 20 THz pulse .

In the figs: 7.8(a) and 7.8(b), the rotational (ΔRE) and translational energy (ΔTE) gain were presented for temperature 600 K at densities 0.3 g/cm^3, 0.064 g/cm^3, 0.02 g/cm^3. With 20 THz pulse, the ΔRE gains maximum energy during the pulse for higher density, which is opposite to pump with 3 THz for the same temperature (fig:6.10(b)). At higher density, the molecules are close to each other due to which there are significantly large librations than lower density. 20 THz resonates the librations directly so, it transfers large energy to the molecules for the higher density. It is easier to rotate the molecule in the low density system at high temperature due to less or no H-bond network among water and the behaviour of water monomers in bulk become similar to isolate water. During the pulse, ΔRE is maximum for 0.3 g/cm^3 with 20 THz pulse, whereas for 3 THz pulse, ΔRE is maximum at 0.02 g/cm^3. Once the envelop of the 20 THz pulse crosses the peak amplitude, ΔTE starts increasing and keep on increasing after the pulse. For the lower density, the increment in ΔTE is very small, whereas ΔTE increases significantly for higher

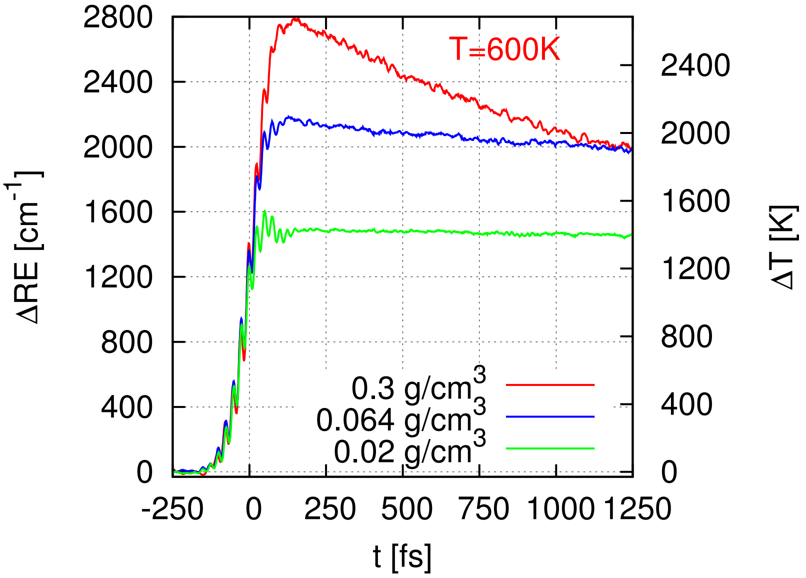

(a)

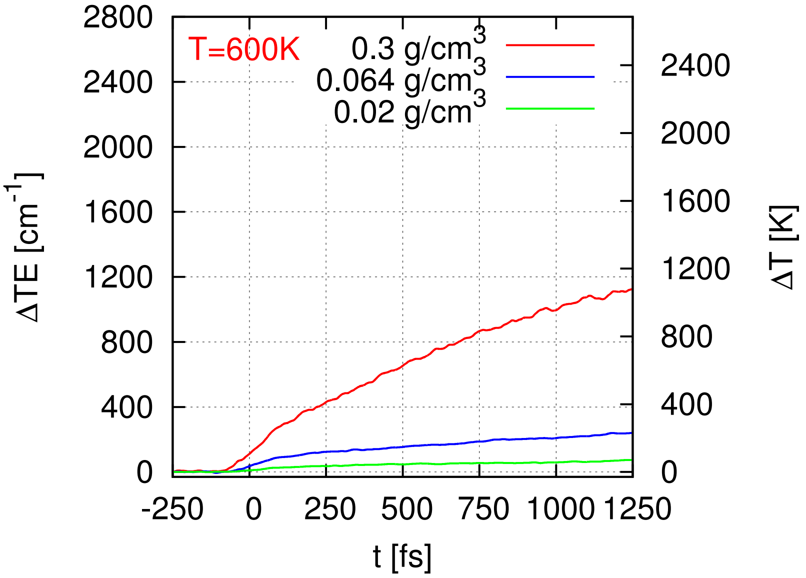

(b)

Figure 7.8: The change in (a) rotational energy (ΔRE) and (b) translational energy (ΔTE) of each water monomer due to THz pump with central frequency 20 THz (60 cm^{-1}) and intensity 5×10^{12} W/cm^2 on liquid water at temperature 600 K with densities 0.3 g/cm^3, 0.064 g/cm^3 and 0.02 g/cm^3.

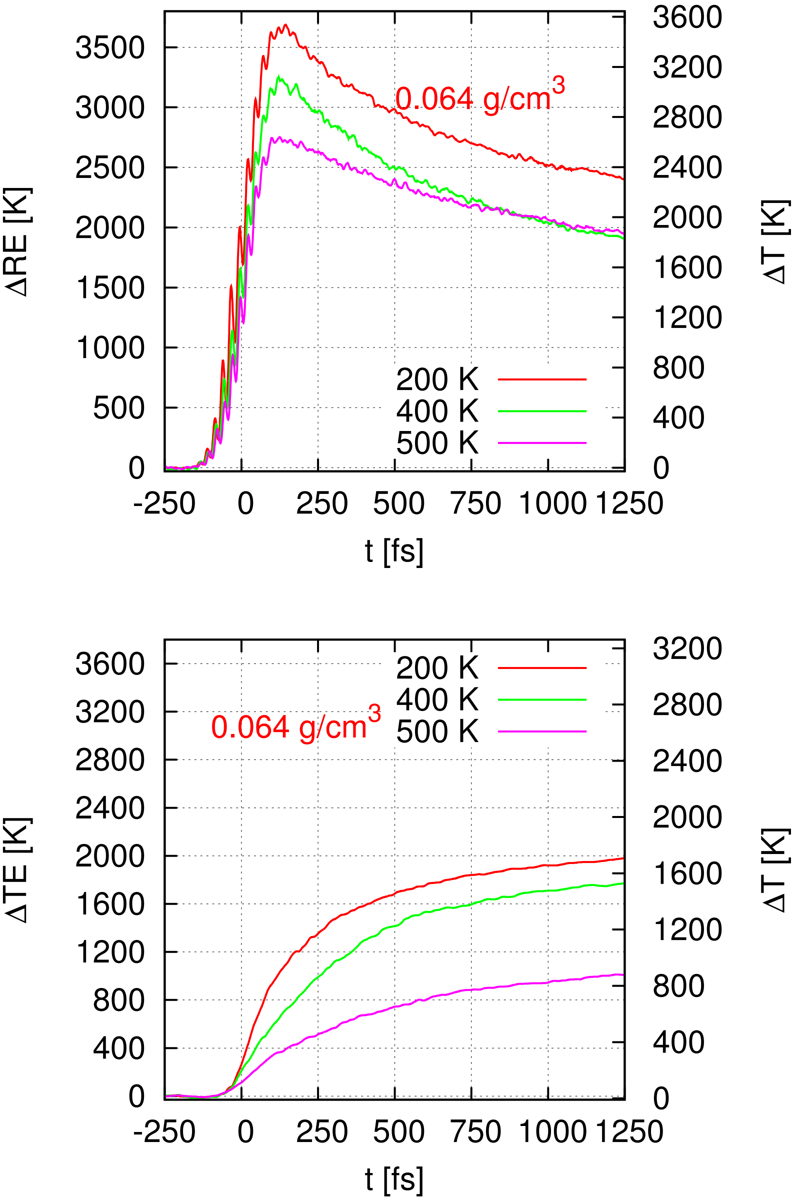

Figure 7.9: The change in (a) rotational energy (ΔRE) and (b) translational energy (ΔTE) of each water monomer due to THz pump with central frequency 20 THz (60 cm^{-1}) and intensity 5×10^{12} $\mathrm{W/cm}^2$ on liquid water with densities 0.064 $\mathrm{g/cm}^3$ at temperatures 200 K, 400 K and 500 K.

density due to large energy transfer from ΔRE after the pulse. In the case of 3 THz, ΔTE is larger for higher density similar to 20 THz pump pulse because ΔTE is the result of collisions among molecules, which will be larger for high density. But, the ΔTE for 3 THz pulse doesn't change so rapidly after the pulse for higher density as in 20 THz pulse and becomes constant very soon. ΔTE increment becomes significant only after the depletion of the H-bond network. So in short, the response of 20 THz pump pulse on ΔRE is opposite to the response for 3 THz pulse.

In the fig: 7.9, we presented the ΔRE (fig: 7.9(a)) and ΔTE (fig: 7.9(b)) of each water monomer for the pump pulse with 20 THz central frequency on liquid water at temperatures 200 K, 300 K and 500 K with density 0.064 g/cm^{-3}. It is interesting to observe that such THz pulse transfers the large energy to ΔRE of each water monomer at low temperature, which is opposite to pump with 3 THz pulse. The reason is similar as described above. The water molecules have more librational modes at low temperature at this density. During the 20 THz pump pulse, ΔRE gains maximum energy for low temperature and as the temperature increases, the energy transfer to RE decreases. At 200 K, the ΔRE decreases after the pump and transfers a large amount of energy to ΔTE. The water monomers are free to rotate at higher temperature and low density and so gains maximum energy from 3 THz pump pulse. At 200 K, the ΔTE and ΔRE increases in very similar timescale and remain constant after the pulse. At low temperature, the energy relaxation is rather fast than high temperature due to the fact that the water is still in condensed phase at low temperature which lead to more collisions. Such THz pulses which are in the frequency range of far-infrared also have the ability to transfer the large amount of energy to the system but the energy transfer doesn't depend only on the strength of the H-bond but also the librations of molecules. The response of vibrations could not be treated at the FF level of the theory and remains an question in this regime.

7.4 Conclusion

The THz pulse of frequency 100 cm^{-1} (3 THz) and full width half maximum of 84.33 fs interacts with the permanent dipole moment of water. Because of water dipole interaction with electric field, the molecules try to rotate in presence of THz pulse but rotations are possible only when the peak amplitude of the pulse is sufficiently large to break H-bond network. The pulse with intensity less than 10^{12} W/cm^2 is not able to break H-bonds among molecules and so, it does not transfer the energy to liquid water at room temperature. The pump pulse with intensity 10^{12} W/cm^2 or higher can break the H-bond network and transfers a large amount of energy to the liquid. The energy transfer to the liquid by the 3 THZ pulses of different fluences in the same pulse duration is a nonlinear process. Once the pulse breaks the H-bond network in water, it transfers all the energy directly to water monomers. Even if the pulse carries a total large energy, the threshold field amplitude is the key parameter required to break the H-bond and transfer the energy to the system. The THz pulses in the frequency region 0.3-3 THz have very similar mechanism to transfer the energy to the water, but the basic requirement is to have the necessary threshold field amplitude.

The pump pulse in the far-IR region also provides a possibility of transferring a large amount of energy to liquid water. Such pulses do not interact with intramolecular mode like bending or stretching. But, the librations have absorption in that frequency range. The pump pulse of 20 THz resonates the librational modes of water. During the pulse, most of the energy is transferred to rotations and once the rotations are sufficiently excited, translations gain energy due to collisions. Interestingly, the pump pulse of far-IR region can also transfer a large amount of energy to the water system. The energy transfer to vibrations with 20 THz pump pulse is still a subject to investigate. Comparing both methods of ultrafast heating of water, the energy transfer mechanism by THz pulse is indirect by rotating the dipoles of water whereas, it is a direct method to transfer energy through resonating the librations of water with an far-IR pump pulse. The pumping with a far-IR pulse can be an adequate tool to transfer the energy to all vibrational modes in sub-ps timescale similarly as lower frequency pulse at 3 THz. The response of solvent-solute dynamics at 20 THz is still unknown to such far-IR pulse.

Chapter 8

Summary and Outlook

The advent of lasers opened the door to initiate the chemical process with a pump pulse and probe the dynamics in femtosecond (fs) timescale. However, the pump-probe studies on chemical processes have been limited only to photoactivated processes, which are minor fraction of all chemical processes. In this dissertation, I investigated the avenues to achieve pump-probe experiments on the thermal chemical reactions in condensed phase with ultrashort and highly intense THz pump pulses via *ab-initio* molecular dynamics simulations. It is discussed in chapter:1 that it is important to generate the temperature-jump (T-jump) in ultrashort time-scale for the pump-probe experiments on thermal chemical processes, so that a significant fraction of reactants acquires the energy in ultrashort timescale to cross the transition state. Importantly, the trigger for the reaction should be shorter than the dynamics of process for clocking the reaction. The pump-probe experiments have increased significantly over the last decade ranging from solids to liquids and biological molecules due to the development of techniques to generate the pulses of a particular frequency fully synchronized with other pulses. These pumping techniques provide a tool to transfer the energy to the system on a picosecond to femtosecond timescale. To resonate the O-H stretching with an infrared pump pulse is a commonly used technique to generate the T-jump in liquid water, the most favorite solvent medium for chemical and biological processes. However, such experiments have been limited to T-jump up to few tens of K until now. The thermal chemical reactions require T-jumps of thousands of kelvin to initiate the process. Interestingly, THz pulse doesn't interact with the internal vibrational mode of water, but rather it excites the collective modes at low intensity which can produce heating like effect. Liquid water has also significantly large absorption cross-section in this spectral region. So in principle, THz pulse offers a possibility to pump the liquid water without being mode selective in transferrig the energy.

Energy Transfer by THz Pulse to Water

In the chapter: 3, I studied that a THz pulse of 3 THz (100 cm^{-1}) central frequency and full width half maximum of 84.43 fs can transfer significantly large amount of energy to the liquid water. Such pump pulse with peak power per unit area of 5×10^{12} which corresponds to peak field amplitude 0.614 V/Å generates the T-jump in liquid water up to 1050 K from 300 K. Most of energy to liquid water is transferred within 100 fs time-scale during which the pulse crosses the peak field amplitude. The pump pulse transfers the energy to translational part (TE) due to the translation of center of mass of molecule, rotational energy due to the rotations around principle axes (RE), and vibrational energy (VE) which includes stretchings and bending. Rotations and translations gain energy in similar timescale, whereas the vibrations follow them within few tens of fs time-delay. It is shown in the chapter: 6 that such large energy gain in water monomers happens mostly due to the interaction of permanent dipole with the electric field, which can be observed from the fact that only rotations gain energy for an isolated water case. In liquid water, highly intense pulse breaks the strong H-bond network among water molecules and molecules start rotating. Such energetic water molecules perform highly hindered rotations and make collisions with neighbors. It is also pointed out in the chapter: 6 that a significantly strong electric field also polarizes the electronic structure of the molecules, which modifies the H-bond strength. It is important for breaking or modifying the H-bond that the pump pulse must have the electric field amplitude higher than the threshold value. If the peak field amplitude is lower than the threshold value, the pulse can not break the H-bond and there will be no energy gain in the liquid.

Structural and Vibrational Transformations in Water by THz Pulse

The large energy transfer to liquid water within sub-ps timescale by such THz pulse causes the significant structural and vibrational modifications, which correspond to thermodynamically high temperature water system. It is already known that coherent X-ray scattering signal of liquid water shows two peak structure at room temperature where one peak at 2 $Å^{-1}$ corresponds to oxygen-oxygen tetrahedral structure and another peak at 3 $Å^{-1}$ corresponds to H-bond density. I investigated in chapter: 3 that the time-resolved coherent x-ray scattering spectrum transforms from two peak structure to one peak structure due to the pump pulse. One peak structure of coherent x-ray scattering signal has been known for liquid water structure at extreme conditions. This structural transformation due to energy transfer by the pump pulse was also justified by time-resolved radial distribution functions (TR-RDF) in chapter: 3. TR-RDF for oxygen-oxygen (g_{O-O}) in chapter: 3 shows the depletion of solvation shell structure of a liquid due to the pump pulse and TR-RDF for oxygen-hydrogen (g_{O-H}) indicates the depletion of H-bond network among molecules. T-jump produced by the THz pulse can also be followed by measuring a transient infrared absorption spectrum as a function of the time-delay. Right after the pulse, the O-H stretching at 3430 cm^{-1} blue shifts, whereas librations red-shifts from 585 cm^{-1}. H-O-H bending remains almost unaffected. In the low frequency region 10 - 400 cm^{-1}, the liquid water shows two peaks at room temperature. One at 60 cm^{-1} corresponds to vibrations of cage structure formed by various water molecules and another peak at 250 cm^{-1} is related to O-O intermolecular stretching vibrations which are hindered translations of H-bond molecules. Both bonds have disappeared after the pump pulse. Within sub-ps time-scale, such a THz pump pulse transforms the liquid water into an environment which is extremely hot gas like dense medium. Due to such ultrashort timescale for transferring the energy, the whole process is isochoric in nature.

Solvent to solute Energy Transfer by THz Pump Pulse

In the chapter: 4, it was discussed that the hot and gas-like liquid medium created by THz pump can also transfer significantly large amount of energy to solute molecules. Phenol, chosen as an example solute, is almost insensitive to such THz pulse in vapor phase, but gains large amount of energy in liquid medium during and after the THz pulse. It is striking that as compared to the water molecule, phenol has a smaller but substantial permanent dipole moment. Even then, isolated phenol gains no energy from the pulse. The main reason is the moment of inertia of phenol, which is too large to rotate the molecule in the short duration of the THz pulse. In general, most of the solutes are either non-polar or have a large moment of inertia, due to which solutes will be insensitive to such THz pulse. The reason behind such large energy transfer to phenol in liquid medium is the strong collisions with highly energetic water molecules. Kinetic temperature jumps from 300 K to 800 K within a ps after the pump pulse. The THz pump pulse modifies the solute-solvent dynamics significantly, which becomes highly diffusive and corresponds to a high temperature state. Phenol molecules changes its neighbor water monomers very quickly due to fast solvent-solute dynamics. Therefore, such a response of phenol in liquid opens the possibility of pump-probe experiments on chemical or biological processes having an energy barrier of the order or lower the achieved T-jump.

Effect of Condensed Phase of the Water on THz Pumping

THz pulse transfers the energy only to rotations of an isolated water, whereas the translations also gain energy in the case of water dimer. This can be well understood by the modifications in potential energy surface in the presence of the static electric field which was investigated in the chapter: 6. Due to the dipole interaction with the electric field, the potential energy curve (PEC) along ∠HOO for water dimer becomes very wide and deep in comparison to the PEC for no field, which shows the dissociative behavior of H-bonds. Even, the effect of electronic structure polarization in presence of strong electric field is also responsible for the modification in PEC for oxygen-oxygen distance (d_{O-O}) in dimer. Bulk water is the mixture of dimers, trimers and big water chains formed with H-bonds. Sufficiently large cluster behaves similar to bulk and gains similar amount of energy in each monomer by the THz pulse due to similar average number of H-bonds in each monomer. So, the strength of H-bond plays a key role in transferring the energy to water by THz pulse. The strength of H-bond depends on the phase of the water system. Ice-phase contains stronger H-bond than liquid phase whereas the gas phase system has no H-bond. Basically, the phase of the water depends on the temperature and density of the closed system and so, the strength of H-bond also depends on them. At a given temperature, the energy transfer to water monomers by THz pulse is higher for the higher density due to strong collisions among molecules. Similarly, the energy transfer to monomers by THz pulse is higher for the higher temperature for the given density due to weak or short lived H-bond at high temperatures. The gas phase system gains large energy only in rotations, whereas condensed phase systems gain energy in rotations as well as translations due to collisional energy transfer. In reference to the THz pump, the behavior of water monomers can be viewed as free rigid rotor in the gas phase and as frustrated rigid rotor in the condensed phase.

The Effect of Frequency, Fluence and Pulse-Duration of THz Pump Pulse

In the chapter: 7, it was shown that THz pulse in the frequency range of 0.3 to 3 THz basically interacts with the permanent dipole of water and transfers the energy to the liquid indirectly without resonating with any particular vibrational mode. However, the fluence and pulse duration are the two important parameters on which the peak power of the pulse depends. It was investigated in chapter: 7 that the 3 THz pump pulse with intensity lower than $5{\times}10^{11}$ W/cm^2 with in half ps pulse duration can not break the H-bond among molecules due to which molecules are not able to rotate and so, there is no energy transfer to liquid water with such a pump pulse. On increasing the intensity beyond $5{\times}10^{11}$ W/cm^{12} with increasing the fluence of the pulse in the same pulse duration, the energy transfer to water is non-linear. Once the H-bond is depleted for the field amplitude (E) higher than the threshold value (E_C), the pump pulse transfers all the energy to the water monomers. Interestingly when the pump pulses have similar fluence but different pulse duration, the energy transfer to water becomes a sub-linear process. Highly intense THz pulses are efficient to transfer large energy to all vibrations of water in sub-ps timescale. If we explore the other ways of energy transfer, far-infrared spectral region also provides a possibility for large T-jump in water. The water has librational modes ($\approx$20 THz) in this region. A pump pulse of 20 THz resonates with the librations directly which are intermolecular modes and breaks the H-bond by shaking the entire molecule. Such a mechanism can possibly be an efficient mechanism to transfer large amount of energy to liquid water on a ps timescale. The difference from THz pump would be the energy transfer to rotations directly during the pulse and then the energy redistribution in other mode which is rather fast process.

Computational Molecular Dynamics Methods

In this dissertation, we presented for the first time the application of time-varying electric field with periodic boundary condition in the ground state using *Ab-initio* molecular dynamics (AIMD) with berry-phase formalism. As discussed in chapter: 2, Born-Oppenheimer based AIMD is an efficient computational method (AIMD) for the ground electronic state dynamics. QUICKSTEP module in CP2K package is an efficient and computationally cheaper tool than others *ab-anitio* methods due to the usage of hybrid basis set and pseudopotential. Time-dependence of electric field was implemented with an external code in combination with CP2K. AIMD simulations also include the polarization effect of electronic structure explicitly in presence of such strong electric field. At the sametime, molecular dynamics with non-polarizable force-fields doesn't include the polarization effect due to such strong field. In chapter: 5, we outlined that force-field molecular dynamics also has limitations to describe collisions among molecules and energy relaxation among different modes in the timescale of less than ps. Intermolecular motions like translations and rotations can be described well qualitatively by freezing the internal vibrations via force-field methods.

Outlook

This study needs an urgent attention of experimentalists to perform the pump-probe experiments on liquid water. THz pump - X-ray probe experiment at XFELs and THz pump - infrared probe experiment with table top sources may open a unique window for chemical dynamics investigation in liquid water.

This study primarily focuses on the basic mechanism of the THz pumping. These basic mechanisms should be used to study whether the rate constant of a chemical or biological reaction can be modified. If it is possible, the range of energy barrier and dimension of reactants should also be investigated for the significant change in rate constant.

20 THz pulse also provides an interesting frequency range to investigate the effect on liquid water. The effect of resonating librational modes on internal vibrations of water is still not fully known. The low intensity pulse in this frequency range can also possibly generate the large T-jump, which should be investigated in more detail.

From a computational point of view, a new force-field should be developed which can describe the strong collisions among molecules and energy relaxation among different modes in less than ps time-scale such that relaxation and energy transfer to intramolecular modes can be properly accounted for. The inclusion of connecting short-range interactions and polarization effect in the force-fields will be key to perform similar studies on large systems of chemical and biological relevance.

Acknowledgment

The time spent at CFEL is the most learning period of my life. First and foremost, I would like express my deepest gratitude to my PhD supervisors **Dr. Oriol Vendrell** and **Prof. Dr. Robin Santra** for providing me the opportunity to work in a young research field of ultrafast science. I thank them from the bottom of my heart for their wonderful guidance, supervision as well as their patience during the discussions. They provided me an excellent atmosphere of scientific research, which was filled with enthusiasm and curiosity. I am very grateful to **Dr. Oriol Vendrell**, in particular for his critical comments and support during the preparation of manuscripts, which has been one of the important learning of my PhD. Doors of the office of **Dr. Oriol Vendrell** have always been open for the discussions and solutions to any problem.

I am very thankful to **Prof. Dr. Michael Thorwart** for his kind willingness to write a report on my dissertation.

I also express my gratefulness to **"Helmholtz Virtual Institute of Dynamic Pathways in Multidimensional Landscapes"** for the financial support during my PhD. The computational work of my PhD would have never been possible without the computing time support on JUROPA cluster by **Jülich Supercomputing Centre**. It was absolutely my pleasure to be the member of graduate school of **The Hamburg Center for Ultrafast Imaging**, which provided me many opportunities to attend winter schools and symposiums.

It has been a great pleasure for me to be the part of **CFEL-DESY Theory Division**, where I learnt about many different aspects of ultrafast and x-ray sciences. It would not have been possible to enjoy my PhD without the cakes and coffee at **h-bar** with colleagues from many countries. I would like to warmly thank to **Sang-Kil Son**, **Malik M. Abdullah**, **Ludger Inhester** and **Vikrant Saxena** for their comments on my thesis. In particular, the translation of abstract in german would not have been possible without the support of **Ludger Inhester**. I am grateful to **Berit Heiser** for her support and care for administrative issues. A special thanks also goes to **Otfried Geffert**, who have always been available to help for cluster and coding related issues. I benefited a lot from the discussions with **Stefan Pbast**, who helped me in starting days of my PhD.

Last but not least, I thank my family and friends who have been a constant source of motivation. Particularly, I am grateful to **Pooja Sahu**, **Swathi Sasikumar**, **Rudrakant Sollapur** and **Krishna Murari** for their company and support during the times, when I felt nostalgic about my home. I owe a debt of gratitude to my parents for their constant encouragement, motivation and blessings to move ahead in life.

Eidesstattliche Versicherung

Hermit erkläre ich an Eides statt, dass ich die vorliegende Dissertationsschrift selbst verfasst und keine anderen als die angegebenen Quellen und Hilfsmittel benutzt habe.

I hereby declare, on oath, that I have written the present dissertation by my own and have not used other than the acknowledged resources.

Hamburg, date Signature

Bibliography

[1] K. A. Connors, *Chemical Kinetics: The Study of Reaction Rates in Solution* (VCH, 1990).

[2] P. Atkins and R. Friedman, *Molecular Quantum Mechanics*, edited by 4th, 978-0-19-927498-7 (Oxford University Press, 2005).

[3] A. Szabo and N. S. Ostlund, *Modern Quantum Chemistry: Introduction to Advanced Electronic Structure Theory* (Dover, 1996).

[4] A. H. Zewail, *Femtochemistry: Ultrafast Dynamics of the Chemical Bond, Vols. 1 and 2* (World Scientific, Singapore, 1994).

[5] Y. T. Lee, Science **236**, 793 (1987).

[6] J. C. Polanyi and D. C. Tardy, J. Chem. Phys. **51**, 5717 (1969).

[7] R. D. Levine and R. B. Bernstein, *Molecular Reaction Dynamics and Chemical Reactivity* (Oxford Univ. Press, New York, 1987).

[8] R. B. Bernstein, *Chemical Dynamics via Molecular Beam and Laser Techniques* (Oxford Univ. Press, New York, 1982).

[9] Y. T. Lee, J. D. McDonald, P. R. LeBreton, and D. R. Herschbach, J. Sci. Instrum. **40**, 1402 (1969).

[10] D. W. Chandler and P. L. Houston, J. Chem. Phys. **87**, 1445 (1987).

[11] A. H. Zewail, Science **242**, 1645 (1988).

[12] P. R. Brooks, Chem. Rev. **88**, 407 (1988).

[13] H. J. Foth, J. C. Polanyi, and H. H. Telle, J. Phys. Chem. **86**, 5027 (1982).

[14] D. Imre, J. L. Kinsey, A. Sinha, and J. Krenos, J. Phys. Chem. **88**, 3956 (1984).

[15] R. B. Metz, T. Kitsopoulos, A. Weaver, and D. M. Neumark, J. Chem. Phys. **88**, 1463 (1988).

[16] K. A. Holbrook, M. J. Pilling, and S. H. Robertson, *Unimolecular reactions* (Wiley, 1996).

[17] M. J. Rosker, M. Dantus, and A. H. Zewail, Science **241**, 1200 (1988).

[18] A. H. Zewail, J. Chem. Soc., Faraday Trans. 2 **85**, 1221 (1989).

[19] U. Banin and S. Ruhman, J. Chem. Phys. **98**, 4391 (1993).

[20] R. Schoenlein, L. Peteanu, R. Mathies, and C. Shank, Science **254**, 412 (1991).

[21] R. J. Sension, S. T. Repinec, A. Z. Szarka, and R. M. Hochstrasser, J. Chem. Phys. **98**, 6291 (1993).

[22] W. Fuss, W. E. Schmid, and S. A. Trushin, J. Chem. Phys. **112**, 8347 (2000).

[23] J. J. H. Beynon, *Application of Transition State Theory to Unimolecular Reaction: An Introduction* (John Wiley & Sons, 1984).

[24] B. G. Barman and G. Tollin, Biochemistry **11**, 4746 (1972).

[25] M. Brunori, C. Greenwood, and M. T. Wilson, Biochem. J. **137**, 113 (1974).

[26] G. C. Kresheck, E. Hamori, G. Davenport, and H. A. Scheraga, J. Am. Chem. Soc. **88**, 246 (1966).

[27] H. Staerk and G. Czerlinski, Nature **205**, 63 (1965).

[28] D. H. Turner, G. W. Flynn, N. Sutin, and J. V. Beitz, J. Am. Chem. Soc. **94**, 1554 (1972).

[29] S. Ameen, Rev. Sci. Instrum. **46**, 1209 (1975).

[30] S. Chen, I. Y. S. Lee, W. A. Tolbert, X. Wen, and D. D. Dlott, J. Phys. Chem. **96**, 7178 (1992).

[31] C. Wan, M. Gupta, and A. H. Zewail, Chem. Phys. Lett. **256**, 279 (1996).

[32] A. Takamizawa, S. Kajimoto, J. Hobley, K. Hatanaka, K. Ohta, and H. Fukumura, Phys. Chem. Chem. Phys. **5**, 888 (2003).

[33] H. Ma, C. Wan, and A. H. Zewail, J. Am. Chem. Soc. **128**, 6338 (2006).

[34] P. Wernet, G. Gavrila, K. Godehusen, C. Weniger, E. T. J. Nibbering, T. Elsaesser, and W. Eberhardt, Appl. Phys. A **92**, 511 (2008).

[35] J. Hobley, S. Kajimoto, A. Takamizawa, K. Ohta, Q. Tran-Cong, and H. Fukumura, J. Phys. Chem. B **107**, 11411 (2003).

[36] O. Mohammed, G. Jas, M. Lin, and A. Zewail, Angew. Chem. Int. Ed. **48**, 5628 (2009).

[37] C. M. Phillips, Y. Mizutani, and R. M. Hochstrasser, Proc. Nat. Acad. Sci. **92**, 7292 (1995).

[38] S. Williams, T. P. Causgrove, R. Gilmanshin, K. S. Fang, R. H. Callender, W. H. Woodruff, and R. B. Dyer, Biochemistry **35**, 691 (1996).

[39] G. Grübel, G. B. Stephenson, C. Gutt, H. Sinn, and T. Tschentscher, Nuclear Instruments and Methods in Physics Research Section B: Beam Interactions with Materials and Atoms **262**, 357 (2007).

[40] N. Huse, H. Wen, D. Nordlund, *et al.*, Phys. Chem. Chem. Phys. **11**, 3951 (2009).

[41] T. B. v. Driel, K. S. Kjær, E. Biasin, K. Haldrup, H. T. Lemke, and M. M. Nielsen, Faraday Discuss. **177**, 443 (2015).

[42] A. Rahman and F. H. Stillinger, The J. Chem. Phys. **55**, 3336 (1971).

[43] A. Vegiri, J. Mol. Liq. Recent Progress in Liquid State Theory. A collection of papers in the honour of Professor Myroslav Holovko on the Occasion of his 60th birthday, **112**, 107 (2004).

[44] A. Vegiri and S. V. Schevkunov, J. Chem. Phys. **115**, 4175 (2001).

[45] S. Vaitheeswaran, H. Yin, and J. C. Rasaiah, J. Phys. Chem. B **109**, 6629 (2005).

[46] J. Kou, H. Lu, F. Wu, J. Fan, and J. Yao, Nano Lett. **14**, 4931 (2014).

[47] Winarto, D. Takaiwa, E. Yamamoto, and K. Yasuoka, The J. Chem. Phys. **142**, 124701 (2015).

[48] S. O. Yesylevskyy, L. V. Schäfer, D. Sengupta, and S. J. Marrink, PLoS Comput Biol **6**, e1000810 (2010).

[49] P. Ren and J. W. Ponder, J. Phys. Chem. B **107**, 5933 (2003).

[50] H. A. Stern and B. J. Berne, The J. Chem. Phys. **115**, 7622 (2001).

[51] A. G. Donchev, N. G. Galkin, A. A. Illarionov, *et al.*, Proc. Natl. Acad. Sci. **103**, 8613 (2006).

[52] G. Ciccotti and G. Jacucci, Phys. Rev. Lett. **35**, 789 (1975).

[53] G. Ciccotti, G. Jacucci, and I. McDonald, J. Stat. Phys. **21**, 1 (1979).

[54] M. W. Evans, The J. Chem. Phys. **77**, 4632 (1982).

[55] M. W. Evans, The J. Chem. Phys. **78**, 5403 (1983).

[56] S.-B. Zhu, J. Lee, and G. W. Robinson, Phys. Rev. A **38**, 5810 (1988).

[57] S.-B. Zhu, J.-B. Zhu, and G. W. Robinson, Phys. Rev. A **44**, 2602 (1991).

[58] R. Reale, N. J. English, J.-A. Garate, P. Marracino, M. Liberti, and F. Apollonio, The J. Chem. Phys. **139**, 205101 (2013).

[59] T. James, D. J. Wales, and J. H. Rojas, The J. Chem. Phys. **126**, 054506 (2007).

[60] P. Umari and A. Pasquarello, Phys. Rev. Lett. **89**, 157602 (2002).

[61] K. Kunc and R. Resta, Phys. Rev. Lett. **51**, 686 (1983).

[62] A. M. Saitta, F. Saija, and P. V. Giaquinta, Phys. Rev. Lett. **108**, 207801 (2012).

[63] A. M. Saitta and F. Saija, Proc. Natl. Acad. Sci. **111**, 13768 (2014).

[64] S. Woutersen, U. Emmerichs, H.-K. Nienhuys, and H. J. Bakker, Phys. Rev. Lett. **81**, 1106 (1998).

[65] S. Woutersen and H. J. Bakker, Nature **402**, 507 (1999).

[66] T. Yagasaki and S. Saito, The J. Chem. Phys. **134**, 184503 (2011).

[67] T. Yagasaki and S. Saito, J. Chem. Phys. **135**, 244511 (2011).

[68] M. Heyden, J. Sun, S. Funkner, G. Mathias, H. Forbert, M. Havenith, and D. Marx, Proc. Natl. Acad. Sci. **107**, 12068 (2010).

[69] B. Ferguson and X.-C. Zhang, Nature Materials **1**, 26 (2002).

[70] D. Hashimshony, A. Zigler, and K. Papadopoulos, Phys. Rev. Lett. **86**, 2806 (2001).

[71] D. W. Van der Weide, J. Murakowski, and F. Keilmann, IEEE Trans.Microwave Theory Tech. **48**, 740 (2000).

[72] A. Oppelt, R. Abela, B. Beutner, B. Patterson, and S. Reiche, Proc. of FEL 2009, Liverpool UK (2009).

[73] G. Zhao, R. N. Schouten, N. van der Valk, W. T. Wenckebach, and P. C. M. Planken, Rev. Sci. Instrum. **73**, 1715 (2002).

[74] A. V. Gubskaya and P. G. Kusalik, J. Chem. Phys. **117**, 5290 (2002).

[75] C. Vicario, A. V. Ovchinnikov, S. I. Ashitkov, M. B. Agranat, V. E. Fortov, and C. P. Hauri, Opt. Lett. **39**, 6632 (2014).

[76] O. Schubert, M. Hohenleutner, F. Langer, *et al.*, Nat Photon **9**, 119 (2014).

[77] F. Blanchard, L. Razzari, H.-C. Bandulet, *et al.*, Opt. Express **15**, 13212 (2007).

[78] M. Shalaby and C. P. Hauri, Nat Commun **6** (2015), 10.1038/ncomms6976.

[79] J. VandeVondele, M. Krack, F. Mohamed, M. Parrinello, T. Chassaing, and J. Hutter, Comput. Phys. Commun. **167**, 103 (2005).

[80] D. Marx and J. Hutter, *"Ab Initio Molecular Dynamics: Theory and Implementation" in "Modern Methods and Algorithms of Quantum Chemistry" (p. 301-449)*, edited by J. Grotendorst (NIC, FZ Jülich, 2000).

[81] P. Hohenberg and W. Kohn, Phys. Rev. **136**, B864 (1964).

[82] W. Kohn and L. J. Sham, Phys. Rev. **140**, A1133 (1965).

[83] G. Lippert, J. Hutter, and M. Parrinello, Mol. Phys. **92**, 477 (1997).

[84] R. N. Barnett, U. Landman, A. Nitzan, and G. Rajagopal, J. Chem. Phys. **94**, 608 (1991).

[85] A. Willand, Y. O. Kvashnin, L. Genovese, *et al.*, The J. Chem. Phys. **138**, 104109 (2013).

[86] S. Goedecker, M. Teter, and J. Hutter, Phys. Rev. B **54**, 1703 (1996).

[87] M. Allen and D. Tildesley, *Computer Simulations of Liquids* (Claredon Press, Oxford, 1987).

[88] R. Resta, J. Phys.: Condens. Matter **12**, R107 (2000).

[89] M. Krack, A. Gambirasio, and M. Parrinello, J. Chem. Phys. **117**, 9409 (2002).

[90] M. E. Tuckerman, *Statistical Mechanics: Theory and Molecular Simulation* (Oxford Univ Press, 2010).

[91] D. Frenkel and B. Smit, *Understanding Molecular Simulation: From Algorithms to Applications* (Academic Press (2nd revised edition), 2001).

[92] T. Darden, D. York, and L. Pedersen, The J. Chem. Phys. **98**, 10089 (1993).

[93] V. Rühle, Am. J. Phys (2007).

[94] D. J. Evans and B. L. Holian, The J. Chem. Phys. **83**, 4069 (1985).

[95] P. Ball, Chem. Rev. **108**, 74 (2008), pMID: 18095715.

[96] F. H. Stillinger, Science **209**, 451 (1980).

[97] Y. Levy and J. N. Onuchic, Annu. Rev. Biophys. Biomol. Struct. **35**, 389 (2006).

[98] J. D. Smith, R. J. Saykally, and P. L. Geissler, J. Am. Chem. Soc. **129**, 13847 (2007).

[99] M. F. Kropman and H. J. Bakker, Science **291**, 2118 (2001).

[100] S. K. Pal, J. Peon, B. Bagchi, and A. H. Zewail, J. Phys. Chem. B **106**, 12376 (2002).

[101] S. Ashihara, N. Huse, A. Espagne, E. Nibbering, and T. Elsaesser, Chem. Phys. Lett. **424**, 66 (2006).

[102] U. Heugen, G. Schwaab, E. Bründermann, M. Heyden, X. Yu, D. M. Leitner, and M. Havenith, Proc. Nat. Acad. Sci. **103**, 12301 (2006).

[103] C. A. Schmuttenmaer, Chem. Rev. **104**, 1759 (2004), pMID: 15080711.

[104] D. F. Plusquellic, K. Siegrist, E. J. Heilweil, and O. Esenturk, Chem. Phys. Chem. **8**, 2412 (2007).

[105] S. Ebbinghaus, S. J. Kim, M. Heyden, *et al.*, Proc. Natl. Acad. Sci. **104**, 20749 (2007).

[106] S. J. Kim, B. Born, M. Havenith, and M. Gruebele, Angew. Chem. Int. Ed. **47**, 6486 (2008).

[107] S. Biedron, J. Lewellen, S. Milton, *et al.*, Proc. of the IEEE **95**, 1666 (2007).

[108] M. Tonouchi, Nat. Photon. **1**, 97 (2007).

[109] C. Bressler, C. Milne, V.-T. Pham, *et al.*, Science **323**, 489 (2009).

[110] D. Fausti, R. I. Tobey, N. Dean, *et al.*, Science **331**, 189 (2011).

[111] N. Huse, S. Ashihara, E. T. Nibbering, and T. Elsaesser, Chem. Phys. Lett. **404**, 389 (2005).

[112] T. D. Kühne, M. Krack, F. R. Mohamed, and M. Parrinello, Phys. Rev. Lett. **98**, 066401 (2007).

[113] C. Vicario, B. Monoszlai, and C. P. Hauri, Phys. Rev. Lett. **112**, 213901 (2014).

[114] M. Krack and M. Parrinello, Phys. Chem. Chem. Phys. **2**, 2105 (2000).

[115] N. Goldman and L. E. Fried, J. Chem. Phys. **126**, 134505 (2007).

[116] G. Hura, D. Russo, R. M. Glaeser, T. Head-Gordon, M. Krack, and M. Parrinello, Phys. Chem. Chem. Phys. **5**, 1981 (2003).

[117] G. E. Walrafen, M. R. Fisher, M. S. Hokmabadi, and W. Yang, J. Chem. Phys. **85**, 6970 (1986).

[118] J. E. Bertie, M. K. Ahmed, and H. H. Eysel, J. Phys. Chem. **93**, 2210 (1989).

[119] A. J. Lock and H. J. Bakker, J. Chem. Phys. **117**, 1708 (2002).

[120] M. Praprotnik, D. Janezic, and J. Mavri, J. Phys. Chem. A **108**, 11056 (2004).

[121] J. Martí, J. A. Padro, and E. Guárdia, J. Chem. Phys. **105**, 639 (1996).

[122] J. A. Padro, J. Marti, and E. Guardia, J. Phys.: Condens. Matter **6**, 2283 (1994).

[123] G. E. Walrafen, Y. C. Chu, and G. J. Piermarini, J. Phys. Chem. **100**, 10363 (1996).

[124] K. Mizoguchi, Y. Hori, and Y. Tominaga, J. Chem. Phys. **97**, 1961 (1992).

[125] J. Hasted, S. Husain, F. Frescura, and J. Birch, Chem. Phys. Lett. **118**, 622 (1985).

[126] G. E. Walrafen, J. Chem. Phys. **44**, 1546 (1966).

[127] M. Souaille and J. C. Smith, Mol. Phys. **87**, 1333 (1996).

[128] M.-C. Bellissent-Funel and J. Teixeira, J. Mol. Struct. **250**, 213 (1991).

[129] J. Teixeira, M. C. Bellissent-Funel, S. H. Chen, and B. Dorner, Phys. Rev. Lett. **54**, 2681 (1985).

[130] S. Krishnamurthy, R. Bansil, and J. Wiafe-Akenten, J. Chem. Phys. **79**, 5863 (1983).

[131] N. Muller, J. Phys. Chem. **76**, 3017 (1972).

[132] R. Rigler, C.-R. Rabl, and T. M. Jovin, Rev. Sci. Instrum. **45**, 580 (1974).

[133] W. Knoll and G. Stark, J. Membr. Biol. **37**, 13 (1977).

[134] T. Y. Tsong and E. Kingsley, J. Biol. Chem. **250**, 786 (1975).

[135] H. Ma, C. Wan, and A. H. Zewail, Proc. Nat. Acad. Sci. **105**, 12754 (2008).

[136] M. R. Bunagan, X. Yang, J. G. Saven, and F. Gai, J. Phys. Chem. B **110**, 3759 (2006).

[137] H. Ma, C. Wan, A. Wu, and A. H. Zewail, Proc. Nat. Acad. Sci. **104**, 712 (2007).

[138] Z. Wang, Y. Pang, and D. D. Dlott, J. Phys. Chem. A **111**, 3196 (2007).

[139] S. Ashihara, N. Huse, A. Espagne, E. T. J. Nibbering, and T. Elsaesser, J. Phys. Chem. A **111**, 743 (2007).

[140] J. Hobley, Y. Kuge, S. Gorelik, M. Kasuya, K. Hatanaka, S. Kajimoto, and H. Fukumura, Phys. Chem. Chem. Phys. **10**, 5256 (2008).

[141] E. H. G. Backus, K.-J. Tielrooij, M. Bonn, and H. J. Bakker, Opt. Lett. **39**, 1717 (2014).

[142] A. Tokmakoff, B. Sauter, and M. D. Fayer, J. Chem. Phys. **100**, 9035 (1994).

[143] P. Wernet, D. Testemale, J.-L. Hazemann, *et al.*, J. Chem. Phys. **123**, 154503 (2005).

[144] P. H.-L. Sit, C. Bellin, B. Barbiellini, *et al.*, Phys. Rev. B **76**, 245413 (2007).

[145] C. J. Sahle, C. Sternemann, C. Schmidt, *et al.*, Proc. Nat. Acad. Sci. **110**, 6301 (2013).

[146] N. Akiya and P. E. Savage, Chem. Rev. **102**, 2725 (2002).

[147] R. Parthasarathi, V. Subramanian, and N. Sathyamurthy, J. Phys. Chem. A **109**, 843 (2005).

[148] D. M. Benoit and D. C. Clary, J. Phys. Chem. A **104**, 5590 (2000).

[149] M. Sodupe, A. Oliva, and J. Bertran, J. Phys. Chem. A **101**, 9142 (1997).

[150] R. J. Lipert and S. D. Colson, J. Phys. Chem. **94**, 2358 (1990).

[151] A. Courty, M. Mons, I. Dimicoli, F. Piuzzi, V. Brenner, and P. Millie, J. Phys. Chem. A **102**, 4890 (1998).

[152] R. Resta, Phys. Rev. Lett. **80**, 1800 (1998).

[153] W. S. Benedict, N. Gailar, and E. K. Plyler, J. Chem. Phys. **24**, 1139 (1956).

[154] N. Larsen, J. Mol. Struct. **51**, 175 (1979).

[155] P. K. Mishra, O. Vendrell, and R. Santra, Angew. Chem. Int. Ed. **52**, 13685 (2013).

[156] G. Herzberg, *Electronic spectra and electronic structure of polyatomic molecules*, (1966).

[157] B. J. Gertner, R. M. Whitnell, K. R. Wilson, and J. T. Hynes, J. Am. Chem. Soc. **113**, 74 (1991).

[158] I. Benjamin, B. J. Gertner, N. J. Tang, and K. R. Wilson, J. Am. Chem. Soc. **112**, 524 (1990).

[159] W. L. Jorgensen, J. Chandrasekhar, J. D. Madura, R. W. Impey, and M. L. Klein, J. Chem. Phys. **79**, 926 (1983).

[160] H. J. C. Berendsen, J. R. Grigera, and T. P. Straatsma, J. Phys. Chem. **91**, 6269 (1987).

[161] J. L. F. Abascal and C. Vega, J. Chem. Phys. **123**, 234505 (2005).

[162] M. A. Gonzalez and J. L. F. Abascal, J. Chem. Phys. **135**, 224516 (2011).

[163] J. L. F. Abascal, E. Sanz, R. G. Fernández, and C. Vega, J. Chem. Phys. **122**, 234511 (2005).

[164] M. W. Mahoney and W. L. Jorgensen, J. Chem. Phys. **112**, 8910 (2000).

[165] H. Nada and J. P. J. M. v. d. Eerden, J. Chem. Phys. **118**, 7401 (2003).

[166] J.-P. Piquemal, L. Perera, G. A. Cisneros, P. Ren, L. G. Pedersen, and T. A. Darden, J. Chem. Phys. **125**, 054511 (2006).

[167] M. Matsumoto, S. Saito, and I. Ohmine, Nature **416**, 409 (2002).

[168] B. M. Auer and J. L. Skinner, J. Chem. Phys. **128**, 224511 (2008).

[169] J. Ma, P. B. Sigler, Z. Xu, and M. Karplus, J. Mol. Bio. **302**, 303 (2000).

[170] D. Vitkup, D. Ringe, G. A. Petsko, and M. Karplus, Nat Struct Mol Biol **7**, 34 (2000).

[171] S. J. Hagen, J. Hofrichter, and W. A. Eaton, Science **269**, 959 (1995).

[172] M. A. Young, S. Gonfloni, G. Superti-Furga, B. Roux, and J. Kuriyan, Cell **105**, 115 (2001).

[173] C. M. Dobson, A. Ŝali, and M. Karplus, Angew. Chem. Int. Ed. **37**, 868 (1998).

[174] M. Karplus and J. A. McCammon, Nat Struct Mol Biol **9**, 646 (2002).

[175] A. K. Rappe, C. J. Casewit, K. S. Colwell, W. A. Goddard, and W. M. Skiff, J. Am. Chem. Soc. **114**, 10024 (1992).

[176] A. Jaramillo-Botero, J. Su, A. Qi, and W. A. Goddard, J. Comput. Chem. **32**, 497 (2011).

[177] D. W. R. Gruen and S. Marcelja, J. Chem. Soc., Faraday Trans. 2 **79**, 225 (1983).

[178] S. Vaitheeswaran, H. Yin, and J. C. Rasaiah, J. Phys. Chem. B **109**, 6629 (2005).

[179] W. Tang, E. Sanville, and G. Henkelman, J. Phys.: Condens. Matter **21**, 084204 (2009).

[180] G. Henkelman, A. Arnaldsson, and H. Jonsson, Comput. Mater. Sci. **3**, 354 (2006).

[181] F. Paesani, S. Iuchi, and G. A. Voth, J. Chem. Phys. **127**, 074506 (2007).

[182] S. O. Yesylevskyy, L. V. Schafer, D. Sengupta, and S. J. Marrink, PLoS Comput Biol **6**, e1000810 (2010).

[183] Y. A. Mantz, B. Chen, and G. J. Martyna, Chem. Phys. Lett. **405**, 294 (2005).

[184] D. Laage and J. T. Hynes, Science **311**, 832 (2006).

[185] M. Levitt, M. Hirshberg, R. Sharon, K. E. Laidig, and V. Daggett, J. Phys. Chem. B **101**, 5051 (1997).

[186] D. R. W. R. L. ROWLEY, Mol. Phys. **94**, 555 (1998).

[187] S. K. Kannam, B. D. Todd, J. S. Hansen, and P. J. Daivis, J. Chem. Phys. **136**, 024705 (2012).

[188] J. D. Smith, C. D. Cappa, K. R. Wilson, R. C. Cohen, P. L. Geissler, and R. J. Saykally, Proc. Natl. Acad. Sci. **102**, 14171 (2005).

[189] E. Schwegler, G. Galli, and F. Gygi, Phys. Rev. Lett. **84**, 2429 (2000).

[190] D. H. Jung, J. H. Yang, and M. S. Jhon, Chem. Phys. **244**, 331 (1999).

[191] E. Dahl, Water Res. **10**, 677 (1976).

[192] R. Zangi and A. E. Mark, J. Chem. Phys. **119**, 1694 (2003).

[193] R. Evans and U. Marini Bettolo Marconi, J. Chem. Phys. **86**, 7138 (1987).

[194] P. Hirunsit and P. B. Balbuena, J. Phys. Chem. C **111**, 1709 (2007).

[195] J. Martí and M. C. Gordillo, Phys. Rev. E **64**, 021504 (2001).

[196] M. Gordillo and J. Martí, Chem. Phys. Letters **329**, 341 (2000).

[197] J. C. Rasaiah, S. Garde, and G. Hummer, Annu. Rev. Phys. Chem. **59**, 713 (2008).

[198] P. Wernet, D. Nordlund, U. Bergmann, *et al.*, Science **304**, 995 (2004).

[199] A. Vegiri, J. Mol. Liq. **110**, 155 (2004).

[200] Y. C. Choi, C. Pak, and K. S. Kim, J. Chem. Phys. **124**, 094308 (2006).

[201] D. Lockhart and P. Kim, Science **257**, 947 (1992).

[202] K. J. Freedman, M. Jürgens, A. Prabhu, C. W. Ahn, P. Jemth, J. B. Edel, and M. J. Kim, Anal. Chem. **83**, 5137 (2011).

[203] M. A. Fox and E. Galoppini, J. Am. Chem. Soc. **119**, 5277 (1997).

[204] L. F. Evans, J. Atmos. Sci. **30**, 1657 (1973).

[205] C.-C. Wang, R.-T. Huang, W.-J. Sheu, and Y.-J. Chang, Int. J. Heat Mass Transfer **47**, 3491 (2004).

[206] S. Franzen, R. F. Goldstein, and S. G. Boxer, J. Phys. Chem. **94**, 5135 (1990).

[207] A. Gopher, Y. Blatt, M. Schönfeld, M. Okamura, G. Feher, and M. Montal, Biophys. J . **48**, 311 (2015).

[208] S. V. Shevkunov and A. Vegiri, J. Mol. Struct.: THEOCHEM **574**, 27 (2001).

[209] S. A. Clough, Y. Beers, G. P. Klein, and L. S. Rothman, J. Chem. Phys. **59**, 2254 (1973).

[210] P. L. Silvestrelli and M. Parrinello, Phys. Rev. Lett. **82**, 3308 (1999).

[211] A. Vegiri, J. Chem. Phys. **116**, 8786 (2002).

[212] D. Rai, A. D. Kulkarni, S. P. Gejji, and R. K. Pathak, J. Chem. Phys. **128**, 034310 (2008).

[213] U. Buck, I. Ettischer, M. Melzer, V. Buch, and J. Sadlej, Phys. Rev. Lett. **80**, 2578 (1998).

[214] J. K. Gregory, D. C. Clary, K. Liu, M. G. Brown, and R. J. Saykally, Science **275**, 814 (1997).

[215] P. K. Mishra, O. Vendrell, and R. Santra, J. Phys. Chem. B **119**, 8080 (2015).

[216] A. Pagnani and M. Pretti, Europhys. Lett. **92**, 46008 (2010).

[217] M. Sprik and M. L. Klein, J. Chem. Phys. **89**, 7556 (1988).

[218] J. L. F. Abascal and C. Vega, J. Phys. Chem. C **111**, 15811 (2007).

[219] S. Niu, M.-L. Tan, and T. Ichiye, J. Chem. Phys. **134**, 134501 (2011).

[220] G. N. Patey and J. P. Valleau, J. Chem. Phys. **64**, 170 (1976).

[221] C. Vega and P. A. Monson, J. Chem. Phys. **102**, 1361 (1995).

[222] S. W. Rick, J. Chem. Phys. **120**, 6085 (2004).

[223] T. Urbic, Chem. Phys. Chem. **610–611**, 159 (2014).

[224] H. B. Levene and J. J. Valentini, J. Chem. Phys. **87**, 2594 (1987).

[225] W. Wagner and A. Pruß, J. Phys. Chem. Ref. Data **31**, 387 (2002).

[226] F. Rettich, N. Vieweg, O. Cojocari, and A. Deninger, J Infrared Milli Terahz Waves , 1 (2015).

[227] D. Grischkowsky, S. Keiding, M. v. Exter, and C. Fattinger, J. Opt. Soc. Am. B **7**, 2006 (1990).

[228] S. Fleischer, Y. Zhou, R. W. Field, and K. A. Nelson, Phys. Rev. Lett. **107**, 163603 (2011).

[229] S. Bartalini, P. Cancio, M. De Rosa, *et al.* (OSA, 2013) p. NM3A.1.

[230] X. Wu, S. Carbajo, K. Ravi, *et al.*, Opt. Lett. **39**, 5403 (2014).

[231] K. Ravi, W. R. Huang, S. Carbajo, X. Wu, and F. Kärtner, Opt. Express **22**, 20239 (2014).

[232] D. M. Carey and G. M. Korenowski, J. Chem. Phys. **108**, 2669 (1998)